Stellingen

behorende bij het proefschrift van Willem Remco Pasterkamp
getiteld:
"The Tyre As Sensor To Estimate Friction"

1. Een frictieschatter die gebaseerd is op het band- of voertuiggedrag kan betrouwbare schattingen opleveren wanneer het frictiepotentieel in aanzienlijke mate benut wordt (*dit proefschrift).*

2. Het verkrijgen van een goede schatting van de frictie tussen band en wegdek onder zo veel mogelijk omstandigheden vereist een combinatie van directe en indirecte methoden (*dit proefschrift).*

3. Wanneer de snelheidsbeperking en de handhaving daarvan geen voor de automobilist als redelijk ervaren doel dienen, zal de automobilist niet geneigd zijn zich aan de snelheidsbeperking te onderwerpen.

4. Het in gebruik nemen van de vluchtstrook tijdens het spitsuur voor normaal verkeer c.q. de afsluiting daarvan buiten het spitsuur suggereert dat men tijdens het spitsuur geen pech onderweg kan krijgen.

5. De verkeersveiligheid is wellicht meer gebaat bij het tegengaan van telefoneren tijdens het autorijden door de bestuurders dan bij het verder perfectioneren van de handhaving van de maximumsnelheid (*The New England Journal of Medicine 1997, Vol. 336, pp. 453-458*).

6. Wanneer de reclameuitzendingen op radio en televisie onderbroken worden door andere programma's, dienen deze eenzelfde gemiddeld volumeniveau te handhaven.

7. Flexibilisering van arbeidstijden wordt gefrustreerd door de niet-flexibele instelling van de meeste kinderopvang-mogelijkheden.

8. Een dichtbevolkt land als Nederland zou zich meer moeten specialiseren in relatief milieuvriendelijke bedrijfstakken zoals financiele en administratieve dienstverlening en softwareontwikkeling in plaats van milieubelastende bedrijfstakken als landbouw en transport. In dit kader is een efficiente elektronische snelweg voor de toekomst wellicht van groter belang dan de Betuwe- of de HSL-lijn of een nieuwe luchthaven.

9. Paars maakt kleurenblind.

10. Wanneer Sir Alexander Fleming volgens de ISO 9000 normen gewerkt zou hebben, zou hij de penicilline niet ontdekt hebben.

The Tyre As Sensor

To

Estimate Friction

The Tyre As Sensor To Estimate Friction

PROEFSCHRIFT

ter verkrijging van de graad van doctor
aan de Technische Universiteit Delft,
op gezag van de Rector Magnificus Prof.dr.ir. J. Blaauwendraad,
in het openbaar te verdedigen ten overstaan van een commissie,
door het College van Dekanen aangewezen,
op maandag 8 december 1997 te 10.30 uur

door

Willem Remco PASTERKAMP
werktuigkundig ingenieur
geboren te Rotterdam

Dit proefschrift is goedgekeurd door de promotoren:
Prof.dr.ir. H.B. Pacejka
Prof.ir. O.H. Bosgra

Samenstelling promotiecommissie:

Rector Magnificus,	voorzitter
Prof.dr.ir. H.B. Pacejka,	TU Delft, promotor
Prof.ir. O.H. Bosgra,	TU Delft, promotor
Prof.Dr.-Ing. L. Palkovics,	TU Budapest
Prof.dr.ir. F.T.M. Nieuwstadt,	TU Delft
Prof.dr.ir. R.F.C. Kriens,	TU Eindhoven
Dr.ir. P.J.Th. Venhovens,	BMW AG München
Prof.dr.ir. J.A. Mulder,	TU Delft, reservelid

Published and distributed by
Delft University Press
Mekelweg 4
2628 CD Delft
The Netherlands
Telephone: +31 15 2783254
Fax: +31 15 2781661
E-mail: DUP@DUP.TUDelft.NL

ISBN/CIP 90-407-1538-6

Printed in the Netherlands

Voor Astrid en Bas,
voor Pim

Table of Contents

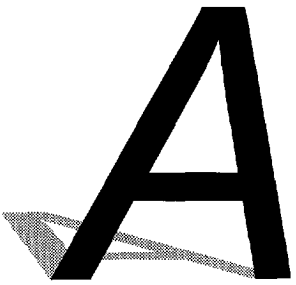

Acknowledgements

The first problem that I encountered in this study was of a financial nature. The intended cooperation with a Dutch company was cancelled because of bankrupcy of the firm in question. Thanks to a grant of the Beek fund, I was able to continue my research. Beek funding is especially intended for research projects to which a degree of risk is attached, in the sense that it is quite unclear if the goals of the project will ever be met. It is therefore with great pleasure that I present this thesis since it shows that within certain limitations, estimation of the tyre-to-road friction using the tyre as a sensor is indeed possible.

I owe special thanks to my promotors, Professor Hans Pacejka and Professor Okko Bosgra, for their advice and criticism, and to my fellow researchers, who have created a pleasant working atmosphere. The people working at the laboratory contributed a great deal to get things up and running for which they deserve my gratitude. Last but not least, I should like to thank my wife and son, who each in their own way supported me throughout the research, especially in the final stages, even though they did not always get the attention they deserved.

Delft, October 17, 1997

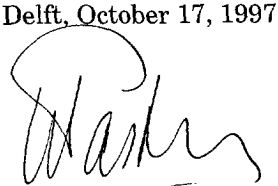

Wim Pasterkamp

1 Introduction

1.1. Motivation and background

The automobile has undergone rapid developments since it was introduced about a century ago. It has evolved into an efficient, reliable and fast vehicle and has become the main means of transport in the industrialised part of the world. Nowadays, the challenges to the vehicle researchers are primarily to enhance the safety and the driving comfort of the vehicle, to enhance the traffic circulation and to reduce environmental pollution by the vehicles. These goals are interrelated to a certain extent. For example, reducing the workload on the driver will generally reduce the number of accidents he causes, and part of the traffic congestion is due to traffic accidents. Traffic congestion, in turn, causes unnecessary environmental pollution.

Over the last few decades, the safety of the vehicle has been enhanced not only by improvements in the construction and the mechanics of the vehicle, but, thanks to the rapid developments in the computer and electronics technology, also by the incorporation of modern control systems. The most popular examples are probably anti-lock brake systems (ABS) and traction control systems (TCS), but four-wheel steering (4WS), active yaw control (AYC) and active suspension have also been introduced into the market. Nowadays attention is focussed on adaptive intelligent cruise control with automatic distance keeping between vehicles, and communication with other vehicles or road administrators about road and traffic conditions.

These control systems can only perform to their full potential if they have access to accurate information about the behaviour of the vehicle. A very important aspect of this behaviour is the interaction between the tyres of the vehicle and the road. The ability of the tyres to transmit forces between tyre and road limits the operating

range of the vehicle. These forces between tyre and road are mainly transmitted by a friction mechanism. If the friction value changes, dramatic changes in vehicle behaviour may result. For example, obstacle avoidance may be impossible at lower friction levels, whereas it is possible at higher friction levels (Figure 1.1). A simple analysis of the stationary circular motion of a point mass shows that the radius of the circle is inversely proportional to the centripetal acceleration. For a vehicle, the maximum achievable acceleration is approximately proportional to the friction level. Consequently, a 10% decrease in friction level results in an 11% increase of the minimum curve radius while a 50% decrease in friction level doubles the minimum curve radius.

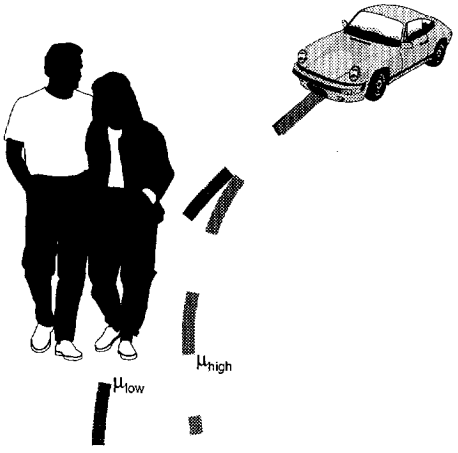

Figure 1.1: *Increase of minimum curve radius due to decrease of friction*

From the viewpoints of safety and from of performance, it is therefore highly desirable to know the capacity of the tyre to transmit forces to the road, both to provide information to the driver (warning signals etc.) and as a sensory input to advanced vehicle control systems.

The different applications make different demands on the friction estimator in terms of accuracy, reliability and speed. For example, on the one hand, most active control systems, such as AYC, are only activated if the vehicle under consideration is recognized as being in a near-critical situation. This implies that an accurate, reliable friction estimate needs to be available in time before the control is activated, but does not need to be available if the vehicle is in a non-critical situation, i.e. driving straight forward without accelerating or decelerating. For AYC systems, 'in time' means in the order of a second, while for ABS systems 'in time' means in the order of 0.01 seconds. On the other hand, although a road administrator needs to know the current state of friction of the road very reliably at

all times, an estimate of this in the order of minutes is acceptable, and it does not need to be very precise. It is therefore important for the designer of a friction estimator to state the purpose of the friction estimate.

1.2. Problem statement

The ability of the tyre to transmit forces mainly depends on the properties of the tyre itself, the orientation of the tyre relative to the road, the load on the tyre that presses the tyre onto the road surface and the friction between tyre and road. Excepting only the friction between tyre and road, these factors are all relatively easy to determine.

Although various methods have been developed to identify tyre/road friction, the final solution to this problem has certainly not yet been found. As will be explained in Chapter 2 in more detail, we may distinguish two different approaches to the friction determination problem: a direct one and an indirect one. The first approach comprehends methods that are directly related to the friction process, for example using forces and accelerations, while the second approach contains methods that monitor some parameters that are related to the frictional process, such as wetness and temperature of the road. Although the methods developed by the second approach may be easily implementable in vehicles and may be relatively inexpensive, the position of this research is to take the first approach, because it has a direct relation to the friction process. It is to be expected though, that both approaches may complement each other.

We would like to look as closely as possible at the source of frictional forces, which brings us to regard the tyre itself as a possible sensor to identify the friction. This implies that as far as possible the friction identification should be separated from the rest of the vehicle behaviour. The clear advantages of this approach are firstly, that the friction identification becomes independent of possibly changing vehicle parameters, and secondly, that it is possible to identify tyre to road friction for individual wheels, as opposed to friction identification for the entire vehicle or per axle. Thus, the main subject of this thesis is:

Investigation of the possibility to use the tyre as a sensor for on-line identification of tyre to road friction characteristics.

It is intended that the friction identification system should be used primarily for driver warning and vehicle control applications implemented on-line in the vehicle.

1.3. Outline of Thesis

Various methods designed to identify the friction coefficient between tyre and road have already been developed. An overview of these methods is presented in Chapter 2. The contribution of this thesis is presented in the subsequent chapters. Chapter 3 discusses the theoretical background of the method based on the tyre modelling theory and Chapter 4 discusses the identification methods employed. Experimental application of the friction identification method and experimental results are discussed in Chapter 5. Chapter 6 gives some examples of possible applications of this identification method in advanced vehicle control systems, illustrated by a case study. Conclusions and recommendations are formulated in the final Chapter 7.

2 Survey on Friction Estimators

2.1. Introduction

This chapter provides a survey of the various existing methods to determine the friction potentials described in the literature. However, before doing this, we will first introduce the concept of friction potentials of a single tyre and of a total vehicle. The various methods to determine the friction potentials are then discussed, and some conclusions are drawn from the survey.

2.2. Friction potentials

2.2.1. Friction potential of the tyre

In [23], the friction potential of a tyre in the longitudinal direction on a specific road is defined as the maximum braking force divided by the vertical tyre load at a nominal vertical load and in the absence of side slip or camber:

$$\mu_K = \left| \frac{F_{x,max}}{F_z} \right|_{F_z = F_{z,nom}} \tag{2.1}$$

Similarly, we can define the friction potential of the tyre in the lateral direction in the absence of longitudinal slip or camber:

$$\mu_\alpha = \left| \frac{F_{y,max}}{F_z} \right|_{F_z = F_{z,nom}} \tag{2.2}$$

Although the friction potentials of the tyre in longitudinal and lateral directions are slightly different, usually $\mu_K > \mu_\alpha$, they are often assumed to be equal. A combined friction potential, describing both longitudinal and lateral friction potentials, however, is always a compromise.

2.2.2. Friction potential of the vehicle

The ability of the vehicle to exploit the friction potentials of the tyres is most important for the interaction of forces between vehicle and road. The friction potential of the total vehicle can be defined by the maximum attainable vehicle accelerations in both longitudinal and lateral directions. This can be illustrated by an acceleration diagram (Figure 2.1).

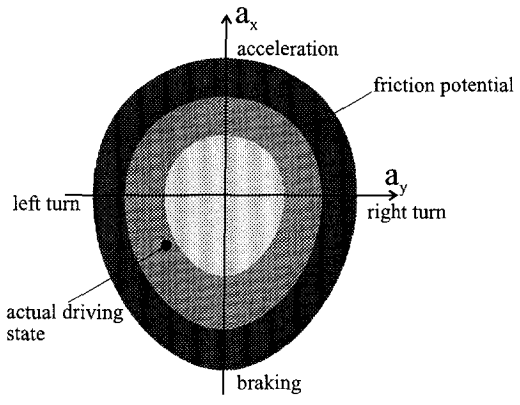

Figure 2.1: *Acceleration diagram*

In this diagram, the horizontal axis represents lateral acceleration and the vertical axis represents longitudinal acceleration. The outer contour in the diagram, the friction potential of the vehicle, represents maximum attainable combinations of accelerations in both directions in steady state conditions, e.g. braking in a curve. The contour is symmetrical with respect to the a_x-axis if the vehicle is symmetrical with respect to its longitudinal axis. In that case, making a left curve is similar to making a right one. The maximum feasible accelerations for driving and braking are not the same. Therefore, the contour is not symmetrical with respect to the a_y-axis. The actual driving state has to be inside the contour and the distance from the actual point in this diagram to the outer contour represents the safety margin. Therefore, the innermost light grey shaded area represents a high safety margin, while a driving state in the dark shaded outermost area represents driving with a very small safety margin.

2.3. Classification of friction estimators

For the classification of the various friction estimation methods, described in the literature, we use the diagram of Figure 2.2.

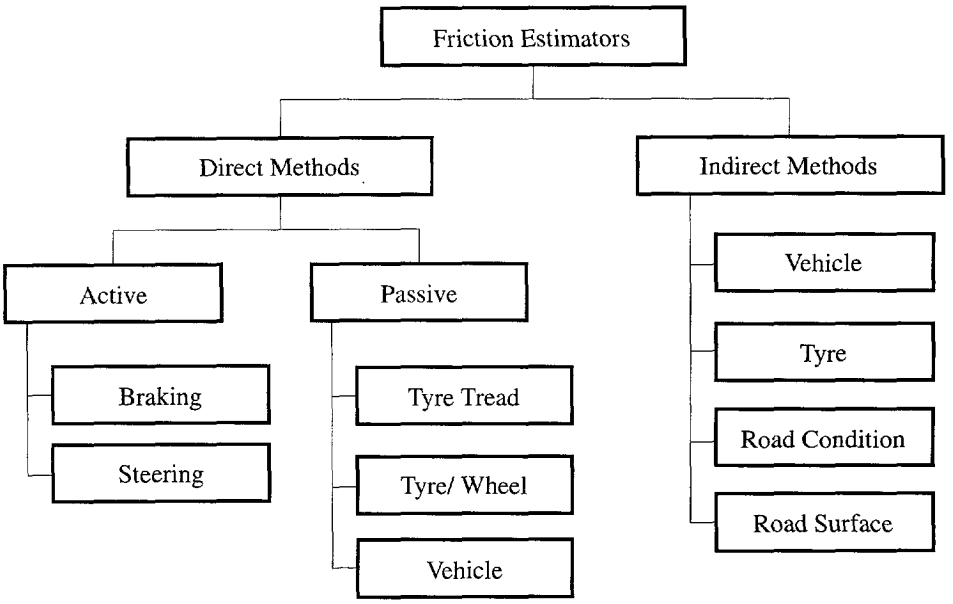

Figure 2.2: *Classification of friction estimation methods*

The first classification is into direct methods (also called effect based [23] methods) and indirect methods (also called parameter based methods). The first category contains methods that are directly related to the frictional process, for example, methods using forces, torques and accelerations. These methods will be considered in section 2.4. The second category contains methods that monitor one or several of the many environmental parameters that affect the frictional process, such as wetness or temperature. These indirect methods will be discussed in section 2.5.

2.4. Direct determination of the tyre friction potential

2.4.1. Active versus Passive Methods

The direct methods can be subdivided into active and passive methods. In this respect, active means deliberate excitation of the tyre or the vehicle such that the responses can be used to determine the friction potential. Passive methods do not use deliberate excitation of the system, but use the responses that are obtained from accidental excitation of the system. Thus, they do not intervene in the vehicle dynamics.

In practice, active methods employ steering or braking of one or more wheels of the vehicle. For example, research has been conducted on perodically changing the toe-in angles of the front wheels. The vehicle response to this excitation provides a measure for the friction coefficient. Also, in severe cornering manoeuvres, the inner

rear wheel may be braked up to wheel lock, or rather up to activation of the ABS system, to provide a friction estimate. Since this wheel is almost unloaded, the resulting brake force is relatively small, having only a minor oversteer influence on the vehicle behaviour.

An advantage of these active methods is that a very accurate prediction of the friction potential of the tyre can be made. However, the disturbance of the vehicle dynamics, which possibly affects safety and driving comfort, the inevitable additional tyre wear and the energy loss involved, should generally be regarded as unacceptable, except possibly in emergency situations.

For these reasons, we will disregard active methods and concentrate on passive methods. These passive methods can be subdivided into three main categories that relate to the choice of system boundaries. The first category focuses on the frictional process between tread elements and road surface at a micro-level. The second category, which also contains the contribution of this thesis, considers the entire wheel together with the tyre as a single element, transmitting forces and torques between road and vehicle. The methods in the third category do not consider individual wheels, but rather the front and rear axles, and use the overall vehicle responses to generate friction estimates. These three categories are described in the next sub-sections.

2.4.5. Determination of the tyre friction potential using tread element behaviour

Roth [16, 57] developed a method to measure tyre to road friction based on the concept that the "global" forces on the tyre (longitudinal and lateral forces) result from the integral of "local" forces (i.e. local stress) over the contact patch,

$$F_i = \int_y \int_x \sigma_i(x,y)\,\mathrm{d}x\,\mathrm{d}y \tag{2.3}$$

where F_i is the global planar tyre force in some direction i and $\sigma_i(x,y)$ is the local horizontal stress in that direction. It is not possible to directly measure the local stresses in the contact patch directly. Instead, the deformation of tread elements was used as an indirect signal for this,

$$F_i = \int_y \int_x c_i TTD_i(x,y)\,\mathrm{d}x\,\mathrm{d}y \tag{2.4}$$

where *TTD* stands for Tyre Tread Deformation and c for the tread stiffness in that direction.

A special tyre sensor called FIT (Friction Indicating Tread) was developed for this purpose. This sensor, based on a Hall-generator, was vulcanised into a tread

element of the tyre (Figure 2.3) and measures the deformation of the tread element as it travels through the contact patch.

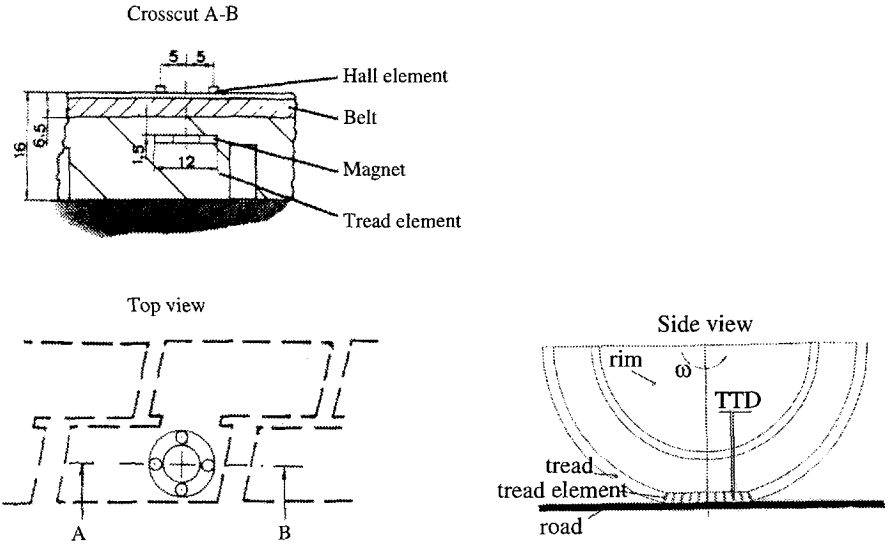

Figure 2.3: *Friction Indicating Tread sensor [16]*

From the TTD-data, three characteristics were calculated, one for friction potential and two for friction demand, in longitudinal and lateral directions respectively. The reported results show that both the friction potential and the friction demand, the part of the friction potential that is being utilized, could be estimated. Since the tread elements will always be deformed as they travel through the contact patch, even in free rolling conditions, at least very low friction conditions could be detected.

A second and a third generation of sensors have been developed [3]. The Hall element and the magnet are no longer separated by the belt in the third generation of sensors. This permits the use of standard steel belt tyres, as opposed to the Kevlar belt tyres that had to be used for the first generation of sensors. Moreover, since the new sensors are located entirely within the tread element, they are practically insensitive to deformations of the belt.

Although this method is very attractive from a scientific point of view and the results are quite good, the required sensors and accompanying equipment probably limit the applicability of this method to research purposes, for example by tyre manufacturers.

2.4.2. Determination of friction potential using tyre or wheel behaviour

General considerations

The majority of friction estimators use the nonlinear tyre force versus (longitudinal and/or lateral) slip relation and its dependency on the friction coefficient to determine both the friction potential and the friction demand. The general force versus slip characteristic of a tyre is shown in Figure 2.4 for two different friction values. The characteristic shown is for longitudinal slip. Although the characteristics for longitudinal and lateral slip are somewhat different, the general shape of the curve is similar. From left to right we first have an almost linear region (I), where the tyre force is approximately linearly dependent on the slip value and practically independent of friction value. This region is followed by a nonlinear region (II) where the increase in tyre force is less than proportional to the increase of slip and reaches a maximum. Then, the tyre force flattens out or decreases in the third region (III). The slip values at which the regions change from one to another depend on the friction coefficients. These regions have been indicated in Figure 2.4 for both high and low μ.

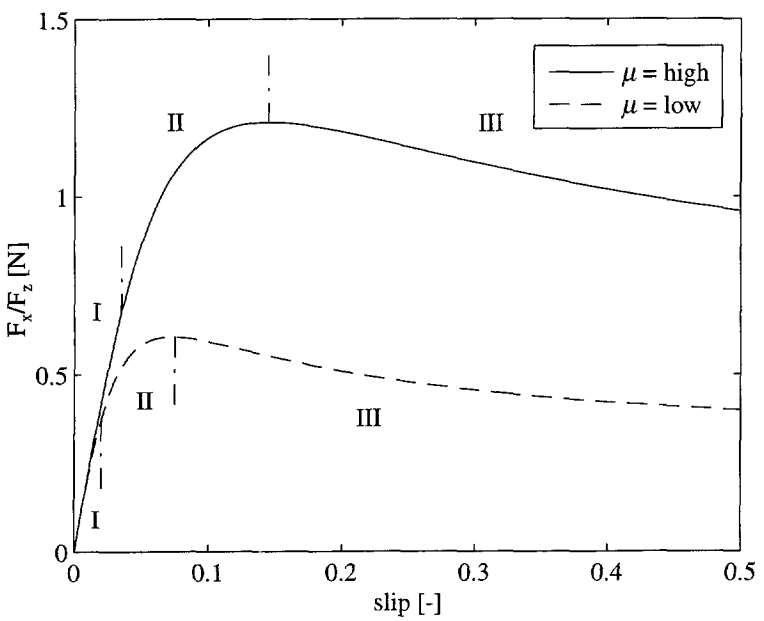

Figure 2.4: *General tyre force versus slip characteristics for two friction values*

The wheel slip and the tyre force need to be determined for the friction estimation. The wheel slip in longitudinal direction is defined by

$$\kappa = \frac{-V_{sx}}{V_x} \tag{2.5}$$

where the longitudinal slip speed V_{sx} is defined by

$$V_{sx} = V_x - \Omega r_e \tag{2.6}$$

and V_x is the vehicle forward speed, Ω is the wheel angular velocity, and r_e is the effective rolling radius of the wheel. Using the wheel speed sensors of the anti-lock brake system, the angular velocity of each wheel can be determined, while the effective rolling radius has an approximately constant value.

In the case of traction, the wheel slip is easily determined from the difference in angular velocity of driven and freely rolling wheels. In the case of braking, the vehicle speed could be determined from integration of the longitudinal acceleration if an accelerometer were installed, which is usually not the case with current ABS systems. Instead, usually the difference in angular velocity between front and rear wheels is used, keeping in mind that the rear wheels are much less braked than the front wheels to prevent rear wheel lock-up. A correction is made for the error in the rear wheel angular speed.

The tyre tractive forces are determined either from the motor management in the case of traction or engine retarding, assuming equal distribution of the tractive force over the driven wheels, or by measuring the driving torques by placing gauges on the drive shafts. Tyre braking forces are determined from the brake pressure, either on the slave cylinders at the wheels, or on the master cylinder at the booster, using the pre-set brake force distribution. This method is inaccurate owing to the possible variation in transmission from brake pressure to actual braking force between tyre and road. Alternatively, the longitudinal acceleration could be used. In the case of driving, this assumes equal distribution of the tractive force over the driven wheels. In the case of braking, the pre-set brake force distribution between front and rear wheels is used and the brake forces on left and right wheels are assumed to be equal on each axle.

Built-in friction estimators in ABS and TCS control

Existing ABS and TCS use built-in friction estimators to determine the maximum circumferential force that the tyre can transmit. Usually, the friction coefficient is not actually estimated, but a related parameter, such as the maximum brake pressure before wheel lock-up, is used. Also, the spin-up of the wheel after release of the brake in the ABS cycle can be used to determine the friction coefficient: if the brake is released, the angular acceleration of the wheel is caused by the frictional force between the tyre and the road only. The friction coefficient is then easily calculated if the moment of inertia and the wheel load are known. However, by their

nature, these systems can only supply friction information when they are activated, that is at critical situations. That is obviously too late to give the driver a warning.

Friction estimation using micro slip

Dieckmann [11, 12] used the longitudinal slip of the wheel due to the traction forces needed to overcome the normal resistance of motion while driving at constant speed to determine the friction potential, that means in area I of Figure 2.4. The slip was determined by measuring the difference in rotational speed of the driven and freely rolling wheels during straight line driving. For his front wheel drive test car, these traction forces were about 130 N per wheel at a constant speed of 70 km/h, which was about 3 % of the wheel load. The wheel slip needed to generate these forces was less than 1 ‰. A new method was developed to measure these small wheel slips. Using this method, the wheel slip could be measured to an accuracy of 0.1 ‰, still using the standard ABS wheel pulse sensors. The tractive forces were derived from the motor management. This implies that only the summed tractive forces over both driven wheels could be determined. Thus it was not possible to recognise so-called μ-split roads, where the friction coefficients of the left and right wheels are different.

The longitudinal slip stiffness of the tyre under small slip was calculated from the quotient of longitudinal force and slip. The principle for the detection of the friction potential of the tyre is that lower longitudinal slip stiffness of the tyre (more slip at the same amount of tractive force) corresponds to a lower friction potential. This was verified by experiments and simulations and appears to hold, but other sources report a number of other factors that also affect the tyre longitudinal slip stiffness. The most important factors appear to be inflation pressure and road surface texture. Bachmann [2] noted that tyre temperature is also important; the longitudinal tyre stiffness is slightly greater in wet conditions due to lower tyre temperature. Therefore, information about the tyre temperature might be needed for friction monitoring based on measurement of the microslip of the wheel.

Overall, since this method relies on extremely small slip values and tyre forces, it seems likely that the method is sensitive to all kinds of disturbances.

Friction estimation using wheel slip behaviour and fuzzy logic

Like Dieckmann, Ito [31] also used the slip needed to develop traction forces to maintain a constant speed. He also derived the traction forces from the motor management and the wheel slip from the ABS-sensors. He observed that a larger amount of longitudinal slip was needed while driving on packed snow than on dry asphalt roads. But in addition to the average magnitude, he also observed a relation between variations in the amplitude of slip fluctuations and the road condition, see Table 2.1.

	Small Torque		Large Torque	
	Slip level	Amplitude of slip fluctuation	Slip level	Amplitude of slip fluctuation
Dry Asphalt	small	small	small	small
Packed Snow	small	small	large	large

Table 2.1: *Road surface characteristics*

Using these road surface characteristics, a fuzzy membership function and a set of rules governing the fuzzy logic control could be constructed, as depicted in Tables 2.2 and 2.3. A rather rough estimate of the tyre-to-road friction could be made by using these fuzzy rules.

L M H	L M H	L M H	Low High
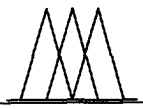	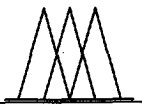	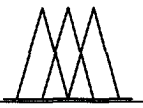	
Traction force	Slip level	Amplitude of slip fluctuation	Road surface condition

Table 2.2: *Fuzzy membership functions*

Traction force	Slip level	Amplitude of slip fluctuation	Road condition
Medium	High	High	Low
Medium	Low	Low	High
High	High	High	Low

Table 2.3: *Fuzzy rules set (abridged)*

Ito also studied the effects of several disturbances on the estimation procedure. Corrections were made for combined slip, while the effects of tyre type, tyre inflation pressure variations and road gradient proved to be small enough to be neglected for this rather rough estimator.

The interesting aspect of this method is the use of statistical information (average value and variation of slip) in the friction estimation. These slip variations may be primarily due to the roughness of the packed snow compared to the smooth asphalt road. In that respect, this method could also be classified as an indirect method.

The same holds true for the method developed by Gustaffson [25]. He also recognised road surface types by monitoring not only the differences, but also the

variances of the measured wheel speeds. This approach, which can be seen as a useful refinement of the work by Dieckmann, was extensively tested and appeared to be able to distinguish at least three different friction levels. The classifier however was sensitive to tyre wear and tyre replacement.

Friction estimation using the rotational wheel dynamics

Kiencke [32] showed the possibility to use brake pressure and wheel slip to estimate the tyre to road friction coefficient using the wheel dynamic behaviour.

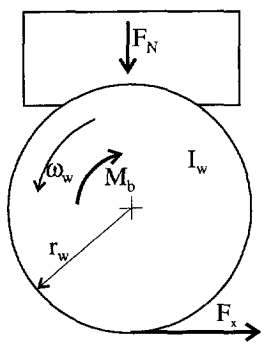

Figure 2.5: *Single Wheel Model*

Figure 2.5 shows a simple single wheel model without vertical dynamics. The frictional force F_x in the contact area between tyre and road depends on the friction coefficient μ as a function of the slip s and the normal load F_N on the wheel:

$$F_x = \mu(s)F_N \tag{2.7}$$

The torque balance of the wheel is formulated by

$$I_w\dot{\omega}_w = F_x r_w - M_b = \mu(s)r_w F_N - M_b \tag{2.8}$$

where I_w is the moment of inertia about the spin axis of the wheel, M_b is the brake torque, r_w is the rolling radius of the wheel and ω is the angular velocity of the wheel. The friction coefficient follows from

$$\mu(s) = \frac{I_w\dot{\omega}_w + M_b}{F_N r_w} \tag{2.9}$$

The brake torque is proportional to the braking pressure:

$$M_b = cp_b \tag{2.10}$$

where p_b is the brake pressure and c is a constant that is usually different for front and rear wheels. The angular velocity of the wheel and the brake pressure were measured while the normal load was determined using a simple single mass vehicle model and the measured longitudinal and lateral accelerations. The tyre to road friction was determined using Recursive Least Squares (RLS).

The developments by Liu [35] are along the same lines. Apart from the RLS method, he also employed an extended nonlinear adaptive observer method, that apparently performed better than RLS.

2.4.2. Determination of friction potential using vehicle behaviour

Introduction

Instead of using the wheel responses, we may use the responses of the total vehicle to determine the friction coefficient. Usually, the implementation of these methods is relatively easy, since they are typically based on the use of vehicle accelerations. It is to be expected that there will be an increase in the application of accelerometers in modern vehicles (e.g. for Vehicle Dynamic Control purposes), that can also be used for friction estimation. However, since these methods use the total vehicle response, only a general average estimate of the tyre to road friction coefficient can be made. For example, a μ-split road cannot be recognised. Moreover, since the sensory inputs used by these methods are located further away from the actual frictional interaction in the tyre-road contact area, it is to be expected that the mechanisms in between the tyre and the sensor (the suspension and the vehicle body) will have a filtering effect. This however, may not be undesirable.

This section describes a steady state method using Neural Networks, and a dynamic, observer-based method. Both methods happen to focus mainly on the lateral vehicle behaviour, as opposed to the previous section, that merely focused on the longitudinal behaviour.

Determination of friction from steady state vehicle behaviour using neural networks

Pal [45] used the steady state vehicle response to estimate the tyre to road friction. He used vehicle speed V, steering angle δ, yaw rate r and slip angle β to feed a neural network (the use of neural networks will be further explained in Chapter 4). This neural network created a static mapping from the measured signals to the friction estimate. Pal used two different types of networks, both with one hidden layer of 6 neurons. Type A had a single output, while type B had multiple outputs (Figure 2.6). In type A, μ was set directly as the output of the network, whereas in type B μ was determined from a number of outputs O_i, $i=1..n$, corresponding to the available number of training sets with different friction values. The teaching signals formed a unit diagonal matrix with dimensions equal to the number of the aforementioned training sets, as shown in table 2.4 for the case $n=3$.

Teaching Signal			Output Signal
μ=1.0	μ=0.4	μ=0.1	
1	0	0	O_1
0	1	0	O_2
0	0	1	O_3

Table 2.4: *Teaching signals for type B architecture*

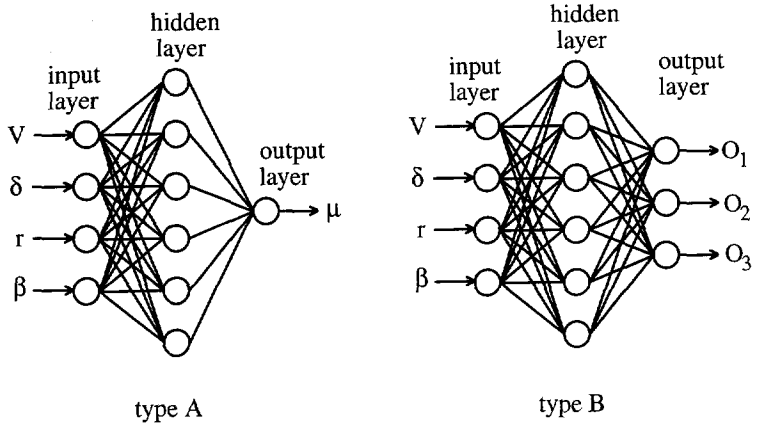

Figure 2.6: *Neural network architectures*

Finally, μ was determined by using Eq. 2.11. This equation is a probabilistic weighted measurement of μ.

$$\mu_{predicted} = \frac{\sum_{i=1}^{3} O_i \mu_i^{teach}}{\sum_{i=1}^{3} O_i} \tag{2.11}$$

Results indicated that the prediction of μ using a type B network was slightly more accurate than the prediction using the type A network. It remains unclear whether this was owing to the probabilistic approach, or to the increased number of parameters of the type B network.

Determination of friction from dynamic vehicle behaviour

Ray [52, 53, 54] used Extended Kalman Filtering (EKF) to estimate vehicle state and tyre forces from an incomplete, noise corrupted measurement set, without a priori knowledge of road conditions or tyre forces. The observer contains an eight degree of freedom vehicle model. The states of the observer are the longitudinal and lateral speeds, the yaw and roll rates, the angular velocities of the four wheels and

the roll angle. The observer is fed by measurements of the angular velocities of the wheels, the brake pressures and the deduced brake torques and the steer angle. The outputs are the yaw rate, the wheel speeds and the longitudinal and lateral accelerations. The observer does not contain a tyre model. Instead, the tyre forces are estimated as parameters. These estimated states and tyre forces are then used in a Bayesian hypothesis selection procedure together with a nominal tyre model to determine the most likely road coefficient of friction. This tyre model may also be determined by off-line processing of estimated vehicle states and tyre forces using EKF.

The results presented by Ray indicate that friction estimation is possible above the level of 0.3 g deceleration in straight line braking and 0.4 g lateral acceleration in cornering on a high friction (μ = 0.9) road. Unfortunately, no experiments were conducted on low friction surfaces. Moreover, the estimator needed about 1.5 seconds to converge to a stable result.

A somewhat simplified but faster version of this method was used by Klaarenbeek [33, 62]. This work only focused on the lateral behaviour of the vehicle. Moreover, the lateral acceleration was used as a sensory input, as opposed to estimation of the lateral acceleration by Ray. The other inputs were the vehicle speed and the steering angle. The observer uses a single track vehicle model with a simple exponential non-linear tyre model. The estimated states are the vehicle slip angle, the yaw rate and the friction coefficient. The output is the lateral acceleration. The output of the observer is compared to the measured lateral acceleration, and the error between measured and calculated acceleration is used to correct the internal vehicle model. The estimated friction is then obtained from the observer states.

The method was only tested in a simulation environment. From simulation experiments, it seems reasonable to assume that the estimator will be effective from about the same level of lateral acceleration as the estimator of Ray. The virtue of this method is its relative simplicity, while only the lateral acceleration is used as an extra sensory input.

2.5. Indirect determination of tyre friction potential

2.5.1. Classification of parameters

The parameters influencing friction can be classified as belonging to either the *vehicle* (e.g. wheel load and speed), the *tyre* (e.g. design, compound, inflation pressure and temperature), the *road condition* (e.g. dry, wet or icy) or the *road surface* (e.g. smooth or rough). The first two categories have been well investigated, and their parameters can be measured relatively easily. Moreover, these

parameters do not change rapidly. The latter two categories have been less well investigated. Their parameters are difficult to measure from the vehicle and may change very rapidly, e.g. potholes or icy patches.

The parameters of the *vehicle* have limited influence on the friction, except for the easily measured vehicle speed. The *tyre*-related parameters also have limited influence, although their influence increases in the presence of a lubricant (a winter tyre has much more grip on ice than a regular tyre). The *road condition* can change the friction dramatically: the road friction can drop from about 1.2 for a dry asphalt road to about 0.5 for a wet asphalt road and even to 0.05 for an icy road. The influence of the road *surface* is rather small as long as it is dry. If, however, the road surface is wet, the differences between road friction onn old cobblestone road and on a good asphalt surface can reach a factor of around 3.

For these reasons, the parameters related to the vehicle and the tyre are usually assumed to be constant and are not continuously monitored. Most systems focus on the road condition and the road surface.

2.5.3. Determination of the road condition

Görich [22, 23] developed a system that makes a qualitative distinction of the local road surface condition in *dry*, *wet* or *icy*. The road condition is determined in three steps. First the road is assumed to be dry. Then whether the road is icy or not is determined. If it is not icy, it is determined whether the road is wet.

Icy road detection

The strategy to detect ice on roads is based on the fact that the slip stiffness of a tyre significantly decreases on icy roads, compared to dry and wet road. This means that at a specific slip value, the friction force is considerably smaller on an iced road than on a dry or wet road. The friction forces and the slip values are determined by using the measured wheel angular velocities, the longitudinal and lateral accelerations and the yaw rate. Using a database containing the results of many test runs, the decision is made if the road is icy or not. This icy road detection is actually related to the direct, wheel-based methods.

Wetness sensors

Two optical wetness sensors were developed by Eichhorn [15] and Holzwarth [29]. The first one is based on the principle of diffuse light reflection using a semi-conductor laser. The second one is based on the different absorption of water for different wavelengths in the near infrared range.

In addition, an acoustical system was developed [23] that measures the acoustic vibrations of the mudguards, using accelerometers. It appears that the frequency content of this sound changes in a typical manner if the tyre swirls water on to the

mudguard when driving on a wet road. For all velocities, the most significant changes in frequency contents are within the 2.5 and 4.5 kHz range. The magnitude of the sound depends on the wheel speed.

Tyre noise [16, 57] depends on virtually all parameters in the friction process between tyre and road. The noise certainly contains information about the friction, but the information is contaminated by the effects of many other parameters. Some of these can be accounted for, (e.g. the type of tyre and the driving speed,) but others, such as the kind of road surface (material and texture), are hard to find without additional information.

2.5.4. Determination of road surface

A sensor was developed that can deliver a profile cut of the road like that which would be produced by a tactile surface analyser, but in this case it is based on optical triangulation using a semi-conductor laser [16]. The sensor performs a high speed distance measurement; in conjunction with the speed of the car, the profile cut is obtained.

A system similar to the acoustical system for wetness detection was developed to measure macro roughness by using accelerometers on the rear suspension arms [23], measuring vertical accelerations. The frequency range of interest is in between 70 and 120 Hz.

2.6. Calculation of the friction potential of the vehicle

Once the maximum feasible tyre forces as a function of the tyre load are known, the maximum achievable accelerations in longitudinal and lateral direction can be calculated using a vehicle model [23]. The main parameters of this vehicle model are the vehicle mass, the position of centre of gravity, the braking force ratio, the roll moment ratio and the aerodynamical and rolling resistance forces. Using these maximally achievable accelerations, contours indicating the friction potential of the vehicle, as shown in Figure 2.1, can be constructed.

In the case of maximum braking deceleration, the effects of a possibly active ABS-system have to be accounted for in the calculations. In general, the maximum longitudinal forces will not be fully exploited when an ABS system is active. The maximum lateral acceleration is affected by the load and the load distribution of the vehicle.

The shape of the contours is primarily defined by the mass distribution of the vehicle in relation to vehicle concept and loading. The road conditions have only minor influence on the shape. For these contours, it is assumed that the vehicle is

driving on a homogeneous road surface and that the vehicle is symmetrical about its longitudinal axis. The thus derived driving limits may serve as a basis for determination of the driving safety margin and driver information systems.

2.7. Conclusions of this chapter

The known friction estimators can be divided into active and passive methods. For reasons of safety, comfort and loss of energy, the active methods are not desirable , except possibly in emergency situations.

The passive methods can be subdivided in indirect and direct methods. The first group includes monitoring all relevant parameters, such as road wetness and temperature, that are somehow correlated to the tyre to road friction. The advantages of such systems are, firstly, that they always provide an estimate no matter the vehicle driving state, and secondly, that depending on the monitored parameters they can be relatively cheap and easy to implement. The disadvantage of such systems is that they do not actually monitor the frictional force interaction between tyre and road surface, but instead one or several of the many parameters that are correlated with the frictional process between the tyre and the road. Chances are that a slippery road surface may not be recognised since it may be due to an unmonitored parameter, such as rotting leaves on the road surface.

From a scientific point of view, it seems preferable to have direct estimators, that estimate the friction using forces or accelerations that are due to the frictional process between tyre and road. However, these systems usually only provide reliable friction estimates in the range of intermediate to high friction utilisation. For most vehicle dynamics control systems the friction information is only needed in this range. If, however, friction information is needed at very low levels of friction utilisation, indirect methods can provide useful additional information.

It is noted that the direct methods using the wheel or tyre behaviour barely use the lateral tyre forces and the self aligning torques that are also generated. The research presented in this thesis exploits these sources of information and is thus a contribution to the category of direct methods.

3 Model Based Friction Estimation

3.1. Introduction

This thesis describes the development of a friction estimator that is implementable in a standard vehicle and can run in real time under normal operating conditions. In this chapter, we will first build the theoretical foundation for the estimator, and then gradually work towards an implementation of the estimator in the subsequent chapters.

Assuming a non-zero friction coefficient between the tyre and the road surface, a tyre, rolling over a road surface and subjected to a vertical load and a side slip angle, generates a side force and possibly also a torque around the tyre's vertical axis, the self aligning torque. As will be explained in this chapter, this torque is due to the asymmetrical buildup of side force over the contact area. The side force and the self aligning torque are linearly independent functions of the tyre-to-road friction coefficient μ as soon as the tyre is partially or entirely sliding over the road surface. This phenomena can be exploited to identify the friction coefficient.

The proposed friction identification method is founded on the simple brush tyre model, which in the next sections will be discussed for pure and combined slip and for camber. The simple brush tyre model yields qualitatively good results compared to the actual tyre behaviour but quantitatively, its performance is rather poor. However, it does have the major advantage of being a well understood physical model. The purpose of discussing the brush tyre model is therefore, to gain insight into the proposed identification method. In quantitative sense much better results can be obtained by using an empirically derived tyre model. The friction identification method will also be discussed using such a model.

3.2. Friction Estimation Using the Brush Tyre Model

The simple steady-state brush tyre model is well known in literature (e.g. [43, 44]), therefore only a recapitulation on the theory will be given here.

3.2.1. Pure Side Slip

The brush tyre model assumes elastic bristles or tread elements connected to the rim at one end and touching the road surface at the other end. This implies the assumption of infinite tyre carcass stiffness. This simplification may be partially compensated by adapting (reducing) the element stiffness so that a more realistic model behaviour is obtained. The effects of tyre width are neglected; the contact patch is modelled as a contact line (Fig. 3.1).

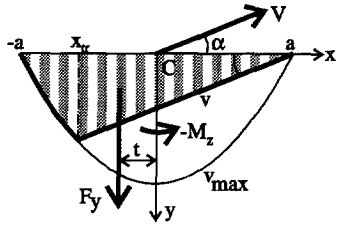

Figure 3.1: *Contact line of steady state side slipping brush type tyre model*

The length of the contact line is assumed to be proportional to the root of the normal load F_z:

$$a^2 = Q^2 F_z \tag{3.1}$$

where a is half the contact length and Q is a constant.

Adhesion

If the direction of the wheel speed vector V encloses a slip angle α with respect to the wheel rim (x-axis), the tread elements deflect as they travel through the contact area. As long as the friction μ between a tread element and the road surface is large enough to deflect the tread element, it is in the adhesion zone: the tread element remains in contact with the same point of the road surface and the contact line is parallel to the wheel speed vector. The tread element generates a side force in proportion to its deflection. The following expressions are obtained:

$$v = (a - x)\tan\alpha \tag{3.2}$$

$$q_{y_{ad}} = c_p \cdot v \qquad \text{for } c_p \cdot v < \mu q_z \tag{3.3}$$

where q_y is the side force distribution, q_z is the normal load distribution and c_p is the lateral tread element stiffness per unit length.

For $\alpha \to 0$ and/or $\mu \to \infty$, these expressions hold for the entire contact region, we have complete adhesion. Due to the asymmetry in the side force distribution with respect to the y-axis, the resultant side force F_y acts at a point shifted over a distance t, the pneumatic trail, from the centre C of the contact line, thus creating the self aligning torque M_z. In the case of complete adhesion, the pneumatic trail has a constant value. Then, the side force, self aligning torque and pneumatic trail become:

$$F_y = \int_{-a}^{a} q_y \, dx \quad = 2c_p a^2 \alpha \tag{3.4}$$

$$-M_z = -\int_{-a}^{a} q_y x \, dx = \frac{2}{3} c_p a^3 \alpha \tag{3.5}$$

$$t = -\frac{M_z}{F_y} \quad = \frac{1}{3} a \tag{3.6}$$

By differentiating Eqs. 3.4 and 3.5 to α, we obtain the cornering stiffnesses for the side force and the self aligning torque:

$$C_{F_\alpha} = 2c_p a^2 \tag{3.7}$$

$$C_{M_\alpha} = \frac{2}{3} c_p a^3 \tag{3.8}$$

Summarising, we conclude that in the case of complete adhesion, side force and self aligning torque do not depend on friction μ, but both are linearly related to the side slip angle α.

Adhesion and sliding

If the friction coefficient μ has a finite value and the load distribution q_z gradually drops to zero at both edges of the contact area, we may have both adhesion and sliding in the contact area. The tread element will be under the regime of adhesion (Equations 3.2 and 3.3) up to the transition point x_{tr}, where the friction force is not able to deflect the tread element sufficiently. From that point up to the trailing edge of the contact area, the tread element slides over the road surface. In the sliding zone, the generation of side force by the tread elements is governed by the friction coefficient μ and the load distribution:

$$q_{y_{sl}} = \mu q_z \qquad \text{for } c_p \cdot v \geq \mu q_z \tag{3.9}$$

For simplicity, a parabolic load distribution over the contact line is assumed:

$$q_z = \frac{3F_z}{4a}\left\{1 - \left(\frac{x}{a}\right)^2\right\} \tag{3.10}$$

The transition point x_{tr} is found by equating expressions 3.3 and 3.9,

$$q_{y_{ad}} = q_{y_{sl}} \tag{3.11}$$

and introducing the dimensionless parameter φ

$$\varphi = \frac{2c_p a^2 |\tan\alpha|}{3F_z} \tag{3.12}$$

or with Eq. 3.1 rewritten to:

$$\varphi = \tfrac{2}{3} c_p Q^2 |\tan\alpha| \tag{3.13}$$

which shows that φ is invariant to normal load or friction coefficient and only varies with the slip angle, we find for the transition point:

$$x_{tr} = a\left(\frac{2\varphi}{\mu} - 1\right) \tag{3.14}$$

Since the transition point needs to be within the contact length, it is clear that $0 \le \varphi \le \mu$. By integrating over the contact patch the contributions of adhesion over $\langle x_{tr}, a]$ and sliding over $[-a, x_{tr}]$, we obtain expressions for side force, self aligning torque and the pneumatic trail as functions of friction and side slip for the partially sliding tyre:

$$F_y = \frac{1}{\mu^2} F_z \varphi\left(3\mu^2 - 3\mu\varphi + \varphi^2\right)\mathrm{sgn}(\alpha) \tag{3.15}$$

$$-M_z = \frac{1}{\mu^3} F_z a \varphi(\mu - \varphi)^3 \,\mathrm{sgn}(\alpha) \tag{3.16}$$

$$t = -\frac{M_z}{F_y} = \frac{a(\mu - \varphi)^3}{\mu\left(3\mu^2 - 3\mu\varphi + \varphi^2\right)} \tag{3.17}$$

Equations 3.15 to 3.17 show that the side force and self aligning torque are two linearly independent functions of the side slip angle α and the friction coefficient μ provided the tyre is partially sliding. This means that if α and μ are the only two unknown variables, they can be obtained by solving the set of nonlinear equations 3.15 and 3.16.

We conclude that the side force and self aligning torque are two linearly independent functions of the side slip angle α and the friction coefficient μ, provided the tyre is partially sliding.

Sliding

Total sliding of the tyre starts if x_{tr} equals a, which results in the condition

$$\varphi = \mu \tag{3.18}$$

In this case, the side force distribution is symmetrical about the y-axis. This implies that t and consequently also M_z equal zero. We have:

$$F_y = \mu F_z \operatorname{sgn}(\alpha) \tag{3.19}$$

$$M_z = 0 \tag{3.20}$$

$$t = -\frac{M_z}{F_y} = 0 \tag{3.21}$$

Thus we find that in the case of total sliding, the side force is proportional to the friction coefficient μ and only related to the side slip angle α with respect to the sign. The self aligning torque and the pneumatic trail equal zero.

3.2.2. Friction estimation in the case of pure side slip

The previous section shows that for the brush tyre model, given the tyre parameters (α and c_p) and the load F_z, the friction μ can be determined through combination of side force and self aligning torque by numerically or graphically solving Eqs. 3.15 and 3.16 in the case of partial sliding, or just from the side force by solving Eq. 3.19 in the case of total sliding. In the case of complete adhesion, μ cannot be determined. The side slip angle α can be determined from either the side force or the self aligning torque using Eq. 3.4 or 3.5 in the case of complete adhesion, or from the combination of side force and self aligning torque using Eqs. 3.15 and 3.16 in the case of partial sliding. In the case of total sliding, the side slip angle can not be determined from the side force or the self aligning torque.

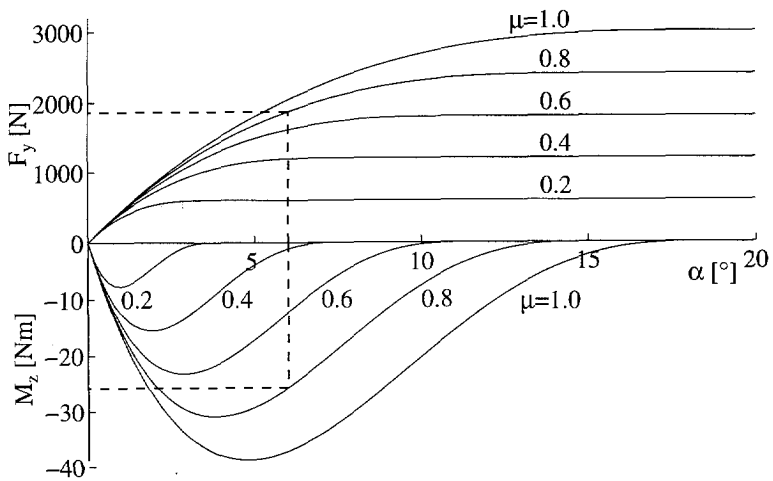

Figure 3.2: *F_y and M_z versus α for various friction levels*

Figure 3.2 illustrates how we can use the tyre, in this case modelled by the brush tyre model, as a sensor to estimate the side slip angle and the friction coefficient. The graph shows the lateral force and the self aligning torque versus the side slip angle for various friction levels μ for the brush type tyre model. A pair of values F_y and M_z, depicted with dashed lines in Fig. 3.2, corresponds to a pair of values α and μ. Thus, for given F_y and M_z, we can find the corresponding values of α and μ.

A more suitable way of presenting this principle is by a so-called Gough-plot, as shown in Figure 3.3 for various side slip angles and friction levels using the brush tyre model at a constant normal load. Lines of constant friction coefficient (solid), constant side slip angle (dotted) and constant pneumatic trail (dash-dotted) are shown in this diagram.

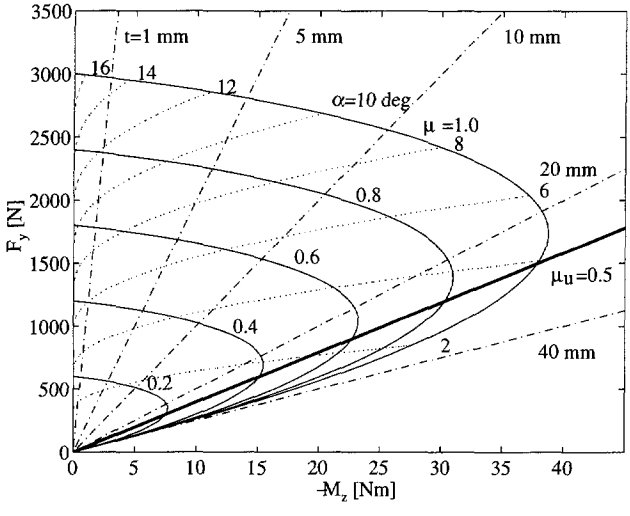

Figure 3.3: *Gough plot for different friction levels and side slip angles*

Over a wide range of variables, the values of α and μ can be derived from F_y and M_z: a pair of values (F_y, M_z) results in a unique pair of values (α, μ), corresponding to a value of t. This holds for the case of partial sliding. Complete adhesion is found where the lines of constant friction coincide. In theory complete adhesion only exists with vanishing slip angle or infinite friction, but from the graph it will be clear that even at finite friction levels where their curves almost coincide it becomes more difficult to distinguish between various friction levels. Along the y-axis, the lines of constant side slip angle coincide. This is the case of total sliding and the different side slip angles cannot be distinguished, but the friction coefficient can be identified.

In order to indicate normal driving conditions in terms of utilised friction potential, Figure 3.3 also shows a thick line of constant utilised friction potential $\mu_u = 0.5$, where μ_u is defined by

$$\mu_u = \frac{F_y}{\mu F_z} \tag{3.22}$$

For the brush tyre model, this becomes

$$\mu_u = \frac{\varphi}{\mu^3}\left(3\mu^2 - 3\mu\varphi + \varphi^2\right)\mathrm{sgn}(\alpha) \tag{3.23}$$

At high friction road surfaces, exceeding this rather arbitrarily chosen value of 50% utilisation of friction potential would require rather severe cornering manoeuvres. Otherwise, only the relatively small part of the graph enclosed by this line and the curve of the highest possible friction coefficient (in this case μ = 1.0) remains available for friction estimation. On the other hand, on low friction road surfaces, one might easily exceed this 50% utilisation of friction potential.

Sensitivity of side force and self aligning torque to α and μ

For the case of combined adhesion and sliding (Equations 3.15 and 3.16) the following expressions for $\frac{\partial F_y}{\partial \mu}$ and $\frac{\partial M_z}{\partial \mu}$ are obtained:

$$\frac{\partial F_y}{\partial \mu} = F_z\,\mathrm{sgn}(\alpha)\frac{\varphi^2}{\mu^3}(3\mu - 2\varphi) \tag{3.24}$$

$$\frac{\partial M_z}{\partial \mu} = -3aF_z\,\mathrm{sgn}(\alpha)\frac{\varphi^2}{\mu^4}(\mu - \varphi)^2 \tag{3.25}$$

Equations 3.24 and 3.25 give rise to some interesting graphs, as depicted in Figure 3.4. Here, the sensitivity S of side force and self aligning torque to changes in friction coefficient is graphed as a function side slip angle and friction coefficient. Both graphs are normalized with respect to vertical load.

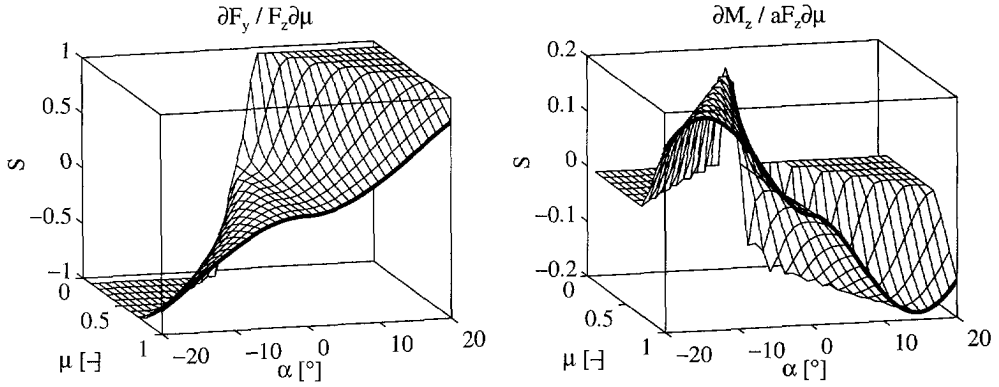

Figure 3.4: *Sensitivity of side force (left) and self aligning moment (right) to changes in friction coefficient*

The left graph, showing sensitivity of side force to friction coefficient, shows a flat area at zero magnitude around zero side slip which narrows for decreasing friction coefficient. This area is due to the insensitivity of the side force to friction coefficient in the adhesion region. As sliding in the contact area increases, the magnitude of the sensitivity rises, up to a limit at total sliding, where it flattens out at the maximum level. At vanishing friction coefficient, there is hardly any adhesion in the contact area, therefore the flat area around zero slip angle vanishes too.

The same reasoning holds true for the right graph in Figure 3.4. Around zero slip angle, there is a more or less flat region, again due to adhesion. Partial sliding in the contact area gives rise to sensitivity of the aligning torque to the friction coefficient. At total sliding however, the aligning torque becomes zero and irrespective of friction coefficient; therefore there is zero sensitivity to friction coefficient again.

Obviously, friction estimation based upon combination of side force and self aligning torque can only be succesful if at least one of these two sensitivities have a non-zero magnitude, that is, there has to be some sliding in the contact area, which underlines the conclusions drawn in section 3.2.

Dimensionless variables

Figure 3.3 is only valid for one specific vertical load. By introducing the dimensionless variables

$$F_y^* = \frac{F_y}{F_z} \tag{3.26a}$$

$$M_z^* = \frac{M_z}{aF_z} \tag{3.26b}$$

$$t^* = \frac{t}{a} = -\frac{M_z^*}{F_y^*} \tag{3.26c}$$

which for the brush tyre model become

$$\begin{aligned} F_y^* &= \frac{\varphi}{\mu^2}\left(3\mu^2 - 3\mu\varphi + \varphi^2\right)\mathrm{sgn}(\alpha) \\ &= \varphi\left(3 - 3\frac{\varphi}{\mu} + \left(\frac{\varphi}{\mu}\right)^2\right)\mathrm{sgn}(\alpha) \end{aligned} \tag{3.27a}$$

$$-M_z^* = \frac{\varphi}{\mu^3}(\mu-\varphi)^3 \operatorname{sgn}(\alpha) = \varphi\left(1-\frac{\varphi}{\mu}\right)^3 \operatorname{sgn}(\alpha) \tag{3.27b}$$

$$t^* = \frac{(\mu-\varphi)^3}{\mu\left(3\mu^2-3\mu\varphi+\varphi^2\right)} = \frac{\left(1-\frac{\varphi}{\mu}\right)^3}{\left(3-3\frac{\varphi}{\mu}+\left(\frac{\varphi}{\mu}\right)^2\right)} \tag{3.27c}$$

the Gough plot can be made invariant to load, as shown in Figure 3.5.

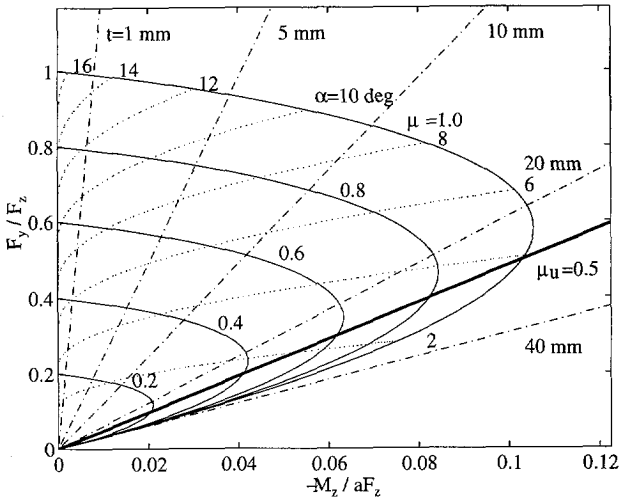

Figure 3.5: *Gough plot for different friction levels and side slip angles, invariant to load*

Invariant lines

Apparently, t^* is a function only of φ/μ. Inspired by early work [18], we may further manipulate the axes to simplify the Gough-diagram to a single curve, invariant to load or friction coefficient. By rewriting Eq. 3.23, we find that, apart from the sign, also μ_u is a function of φ/μ only:

$$\mu_u = \frac{\varphi}{\mu}\left(3-3\frac{\varphi}{\mu}+\left(\frac{\varphi}{\mu}\right)^2\right)\operatorname{sgn}(\alpha) \tag{3.28}$$

Since this third order function is monotonically increasing, the function is invertible, although the solution is tedious. Thus, it is possible to describe t^* as a function of μ_u. We may now draw a graph of μ_u versus t^* as shown in Figure 3.6. The resulting graph is a single curve, invariant to load or friction coefficient, which can be quite accurately approximated by a second order polynomial. As we would expect from Eqs. 3.21 and 3.6, the magnitude of t^* varies between 0 at full sliding and 1/3 at full adhesion.

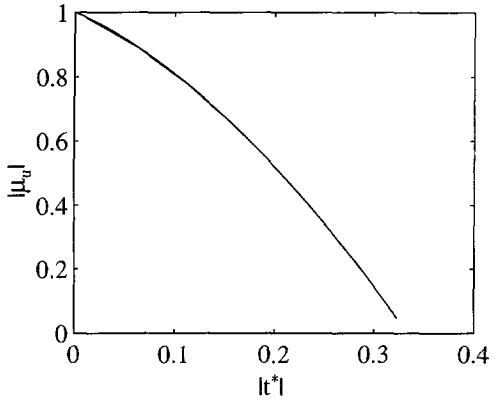

Figure 3.6: *Utilised friction potential versus normalized pneumatic trail (brush tyre model)*

The procedure to estimate friction would have been to calculate the variable t^* from measured F_y and M_z and available contact length, evaluate the polynomial and deduce the friction coefficient μ from the resulting μ_u by using Eq. 3.22. It is noted that t^* represents the pneumatic trail normalized for the contact length, and since the contact length is in this model only a function of vertical load, it can also be interpreted as the pneumatic trail normalized for the vertical load.

3.2.3. Sensitivity analysis for friction estimation in the case of pure side slip

The friction coefficient and side slip angle are estimated using measured signals with limited accuracy, due to imperfections in the measurement system and noise. The sensitivity to measurement errors is calculated for the case of pure side slip using an approach based on Taylor series [14, 19]:

Method

Suppose N is a function of n independent variables $u_1, u_2, \ldots, u_n$,

$$N = f(u_1, u_2, \ldots, u_n) \tag{3.29}$$

These variables u_i $(i=1,2,\ldots,n)$ are measured with a possible error of $\pm\Delta u_i$. These errors result in a total error in the final result:

$$N \pm \Delta N = f(u_1 \pm \Delta u_1, u_2 \pm \Delta u_2, \ldots, u_n \pm \Delta u_n) \tag{3.30}$$

Developing the function f in a Taylor series results in:

$$f(u_1 \pm \Delta u_1, u_2 \pm \Delta u_2, \ldots, u_n \pm \Delta u_n) = f(u_1, u_2, \ldots, u_n) \pm \Delta u_1 \frac{\partial f}{\partial u_1} \pm \Delta u_2 \frac{\partial f}{\partial u_2} \pm \ldots \pm \Delta u_n \frac{\partial f}{\partial u_n} \pm \frac{1}{2}\left[(\Delta u_1)^2 \frac{\partial^2 f}{\partial u_1^2} + \ldots \right] \pm \ldots \tag{3.31}$$

Generally speaking, the higher order terms are negligible if the magnitudes of Δu_i are small. The 'worst-case' total absolute error E_a is then formulated as

$$E_a = \left| \Delta u_1 \frac{\partial f}{\partial u_1} \right| + \left| \Delta u_2 \frac{\partial f}{\partial u_2} \right| + \ldots + \left| \Delta u_n \frac{\partial f}{\partial u_n} \right| \tag{3.32}$$

The magnitudes of the partial derivatives indicate which variables have major influence on the error in the final result.

Application to the estimation of μ and α

Applying this theory to the estimation of side slip angle and friction coefficient, we estimate the friction coefficient μ, the side slip angle α and the vertical load F_z from the independent variables F_y, M_z and F_z and we write in analogy to Eq. 3.29:

$$\mu = \mu(F_y, M_z, F_z, \ldots) \tag{3.33a}$$

$$\alpha = \alpha(F_y, M_z, F_z, \ldots) \tag{3.33b}$$

and rather trivial:

$$F_z = F_z(F_z) \tag{3.33c}$$

We may restrict this analysis to the variables side force, self aligning torque and vertical load. The worst case total errors are then formulated as

$$E_{\mu,a} = \left| \Delta F_y \frac{\partial \mu}{\partial F_y} \right| + \left| \Delta M_z \frac{\partial \mu}{\partial M_z} \right| + \left| \Delta F_z \frac{\partial \mu}{\partial F_z} \right| \tag{3.34a}$$

$$E_{\alpha,a} = \left| \Delta F_y \frac{\partial \alpha}{\partial F_y} \right| + \left| \Delta M_z \frac{\partial \alpha}{\partial M_z} \right| + \left| \Delta F_z \frac{\partial \alpha}{\partial F_z} \right| \tag{3.34b}$$

$$E_{F_z,a} = \left| \Delta F_y \frac{\partial F_z}{\partial F_y} \right| + \left| \Delta M_z \frac{\partial F_z}{\partial M_z} \right| + \left| \Delta F_z \frac{\partial F_z}{\partial F_z} \right| \tag{3.34c}$$

Considering Eq. 3.33c, we obviously conclude that

$$E_{F_z,a} = |\Delta F_z| \tag{3.35}$$

The determination of the other errors requires the determination of the partial derivatives in these expressions. This is facilitated by using the earlier introduced dimensionless variables (Eq. 3.26). For the friction coefficient we have

$$\frac{\partial \mu}{\partial F_y} = \frac{\partial \mu}{\partial F_y^*}\frac{\partial F_y^*}{\partial F_y} \tag{3.36a}$$

$$\frac{\partial \mu}{\partial M_z} = \frac{\partial \mu}{\partial M_z^*}\frac{\partial M_z^*}{\partial M_z} \tag{3.36b}$$

$$\frac{\partial \mu}{\partial F_z} = \frac{\partial \mu}{\partial F_y^*}\frac{\partial F_y^*}{\partial F_z} + \frac{\partial \mu}{\partial M_z^*}\frac{\partial M_z^*}{\partial F_z} \tag{3.36c}$$

and similarly for the side slip angle we have

$$\frac{\partial \alpha}{\partial F_y} = \frac{\partial \alpha}{\partial F_y^*}\frac{\partial F_y^*}{\partial F_y} \tag{3.37a}$$

$$\frac{\partial \alpha}{\partial M_z} = \frac{\partial \alpha}{\partial M_z^*}\frac{\partial M_z^*}{\partial M_z} \tag{3.37b}$$

$$\frac{\partial \alpha}{\partial F_z} = \frac{\partial \alpha}{\partial F_y^*}\frac{\partial F_y^*}{\partial F_z} + \frac{\partial \alpha}{\partial M_z^*}\frac{\partial M_z^*}{\partial F_z} \tag{3.37c}$$

In order to simplify the algebra in this discussion, we consider only the case of $\alpha > 0$.

Sensitivity of μ with respect to F_y, M_z and F_z

A Gough-diagram (Fig. 3.7) shows the dimensionless side force versus the negative dimensionless aligning torque for two friction values, μ and $\mu+\Delta\mu$. It is important to note that additional curves can be created by multiplication of the original curve with respect to the origin.

We define a point P, pointed to by a vector p, and a point P_n at $p+\Delta p$. We have

$$p = \begin{bmatrix} -M_z^* \\ F_y^* \end{bmatrix}, \quad \Delta p = \begin{bmatrix} -\Delta M_z^* \\ \Delta F_y^* \end{bmatrix} \tag{3.38}$$

The vector Δp can be resolved into the vectors Δp_{t^*} along the line of constant t^* and Δp_μ along the curve of constant μ:

$$\Delta p = \Delta p_{t^*} + \Delta p_\mu \tag{3.39}$$

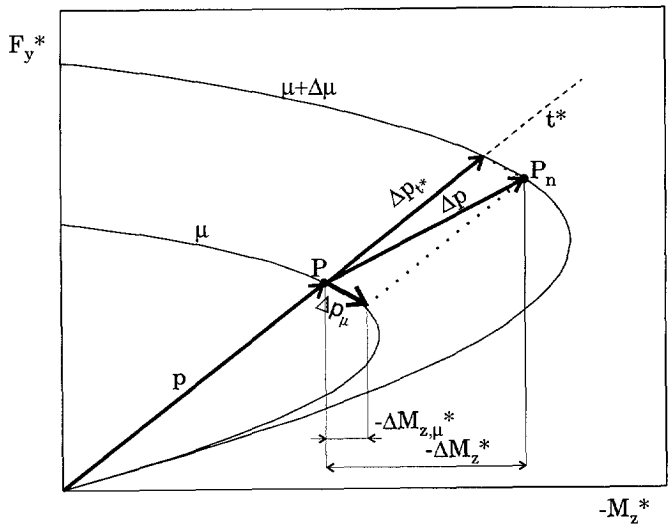

Figure 3.7: *Gough-diagram of dimensionless side force versus aligning torque for two friction levels*

The component vectors become

$$\Delta p_{t^*} = \frac{\Delta\mu}{\mu} p$$

$$\Delta p_\mu = -\Delta M_{z,\mu}^* \left[1 \quad \left. \frac{\partial F_y^*}{\partial\left(-M_z^*\right)} \right|_\mu \right]^T \tag{3.40}$$

For the components of Δp we have

$$-\Delta M_z^* = \frac{\Delta\mu}{\mu}\left(-M_z^*\right) - \Delta M_{z,\mu}^*$$

$$\Delta F_y^* = \frac{\Delta\mu}{\mu} F_y^* - \Delta M_{z,\mu}^* \left. \frac{\partial F_y^*}{\partial\left(-M_z^*\right)} \right|_\mu \tag{3.41}$$

and by elimination of $-\Delta M_{z,\mu}^*$ we obtain

$$\Delta\mu = \frac{\mu\Delta F_y^* + \mu\Delta M_z^* \left. \frac{\partial F_y^*}{\partial\left(-M_z^*\right)} \right|_\mu}{F_y^* + M_z^* \left. \frac{\partial F_y^*}{\partial\left(-M_z^*\right)} \right|_\mu} \tag{3.42}$$

so that for infinitesimally small Δ's we have

$$\frac{\partial\mu}{\partial F_y^*} = \frac{\mu}{F_y^* + M_z^* \left.\dfrac{\partial F_y^*}{\partial\left(-M_z^*\right)}\right|_\mu} \tag{3.43a}$$

$$\frac{\partial\mu}{\partial M_z^*} = \frac{\mu \left.\dfrac{\partial F_y^*}{\partial\left(-M_z^*\right)}\right|_\mu}{F_y^* + M_z^* \left.\dfrac{\partial F_y^*}{\partial\left(-M_z^*\right)}\right|_\mu} \tag{3.43b}$$

The partial derivative $\partial F_y^* / \partial\left(-M_z^*\right)\big|_\mu$ in these expressions describes the slope of the tangent to the curve of constant friction coefficient. Along this curve, the side slip angle α is the only running variable. We may write

$$\left.\frac{\partial F_y^*}{\partial\left(-M_z^*\right)}\right|_\mu = \frac{\left.\dfrac{\partial F_y^*}{\partial\alpha}\right|_\mu}{\left.\dfrac{\partial\left(-M_z^*\right)}{\partial\alpha}\right|_\mu} \tag{3.44}$$

For the brush tyre model we find (for $0 \le \varphi \le \mu$)

$$\left.\frac{\partial F_y^*}{\partial\tan\alpha}\right|_\mu = 2c_p Q^2\left(1-\frac{\varphi}{\mu}\right)^2 \tag{3.45a}$$

$$\left.\frac{\partial\left(-M_z^*\right)}{\partial\tan\alpha}\right|_\mu = \frac{2}{3}c_p Q^2\left(1-\frac{\varphi}{\mu}\right)^2\left(1-\frac{4\varphi}{\mu}\right) \tag{3.45b}$$

and the slope of the tangent to the curve of constant friction coefficient becomes

$$\left.\frac{\partial F_y^*}{\partial\left(-M_z^*\right)}\right|_\mu = \frac{3\mu}{\mu-4\varphi} \tag{3.46}$$

We note that for finite μ, the slope becomes 3 for vanishing φ, that is at zero slip angle, which agrees with Eq. 3.6. Furthermore, for $\varphi=\mu$, that is at total sliding, the slope becomes -1. With Eq. 3.46, Eq. 3.43 now becomes (with $0 \le \varphi \le \mu$)

$$\frac{\partial \mu}{\partial F_y^*} = -\left(\frac{\mu}{\varphi}\right)^2 \frac{\mu(\mu - 4\varphi)}{6\mu^2 - 4\mu\varphi + \varphi^2} \tag{3.47a}$$

$$\frac{\partial \mu}{\partial M_z^*} = -\left(\frac{\mu}{\varphi}\right)^2 \frac{3\mu^2}{6\mu^2 - 4\mu\varphi + \varphi^2} \tag{3.47b}$$

Furthermore, we have

$$\frac{\partial F_y^*}{\partial F_y} = \frac{1}{F_z} \tag{3.48a}$$

$$\frac{\partial M_z^*}{\partial M_z} = \frac{1}{aF_z} \tag{3.48b}$$

$$\frac{\partial F_y^*}{\partial F_z} = -\frac{1}{F_z^2} F_y \tag{3.48c}$$

$$\frac{\partial M_z^*}{\partial F_z} = -\frac{3}{2aF_z^2} M_z \tag{3.48d}$$

and substituting Eqs. 3.15, 3.16, 3.47 and 3.48 in Eq. 3.36 we find

$$\frac{\partial \mu}{\partial F_y} = -\frac{\mu^3(\mu - 4\varphi)}{F_z\varphi^2\left(6\mu^2 - 4\mu\varphi + \varphi^2\right)} \tag{3.49a}$$

$$\frac{\partial \mu}{\partial M_z} = -\frac{3\mu^4}{aF_z\varphi^2\left(6\mu^2 - 4\mu\varphi + \varphi^2\right)} \tag{3.49b}$$

$$\begin{aligned}\frac{\partial \mu}{\partial F_z} &= \left(\frac{\mu}{\varphi}\right)^2 \frac{\mu(\mu - 4\varphi)}{6\mu^2 - 4\mu\varphi + \varphi^2} \frac{1}{F_z^2} F_y + \left(\frac{\mu}{\varphi}\right)^2 \frac{3\mu^2}{6\mu^2 - 4\mu\varphi + \varphi^2} \frac{3}{2aF_z^2} M_z \\ &= -\frac{\mu\left(6\mu^3 - 12\mu^2\varphi + 14\mu\varphi^2 - 5\varphi^3\right)}{\varphi F_z\left(6\mu^2 - 4\mu\varphi + \varphi^2\right)}\end{aligned} \tag{3.49c}$$

We note that both $\partial\mu/\partial F_y$ and $\partial\mu/\partial F_z$ are inversely proportional to F_z, while $\partial\mu/\partial M_z$ is inversely proportional to aF_z, or with Eq. 3.1, inversely proportional to $F_z\sqrt{F_z}$. Furthermore, the following table shows the values that the sensitivities take for the extreme values of φ.

	$\varphi \to 0$	$\varphi = \mu$
$\partial\mu/\partial F_y$	$-\infty$	$1/F_z$
$\partial\mu/\partial M_z$	$-\infty$	$-1/aF_z$
$\partial\mu/\partial F_z$	∞	$-1/F_z$

Table 3.1: *Sensitivities for extreme values of φ*

These results are also illustrated by Figure 3.8. The graphs of this figure were generated at a given value of F_z and thus of a of 4000 N and 0.1131 m, respectively. The meshgrids in these graphs are triangular because of the limitation that φ cannot exceed μ in magnitude.

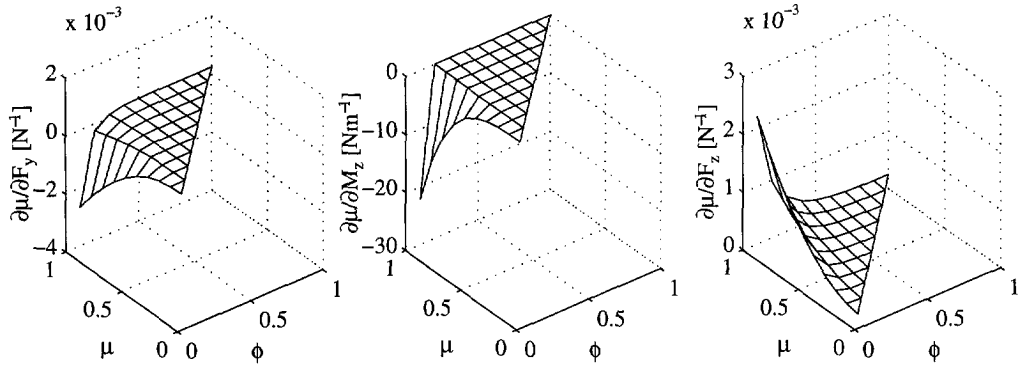

Figure 3.8: *Sensitivity of μ-estimate with respect to the independent variables F_y, M_z and F_z at a given vertical load*

For $\varphi \to 0$, we have vanishing sliding in the contact patch, that is we approach total adhesion. It is the area where the curves of constant friction in the Gough-diagram (Fig. 3.7) approach each other. It is easily understood that very small errors in the values of side force or aligning torque can make large differences in the friction estimate near the origin of the Gough-plot. The larger the actual friction coefficient, the stronger this effect is. Since an error in the vertical load results in an erroneous perception of the side force and the aligning torque, errors in the load also affect the friction estimate primarily in the case of adhesion.

Considering the fact that the side force and aligning torque are an order in magnitude larger than the aligning torque, it becomes clear that primarily the sensitivity to errors in the aligning torque in the case of total adhesion is very large.

This is further illustrated by Figure 3.9, showing the sensitivities of the friction to relative errors in side force, aligning torque and vertical load.

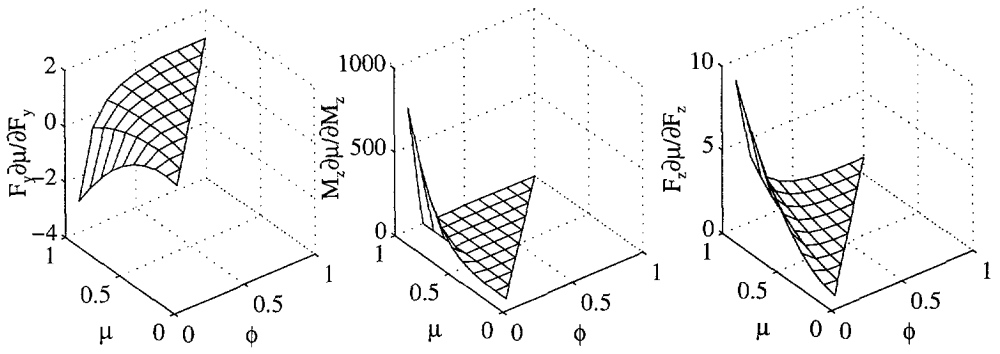

Figure 3.9: *Relative sensitivity of μ-estimate with respect to the independent variables F_y, M_z and F_z at a given vertical load*

Sensitivity of α with respect to F_y, M_z and F_z

For the sensitivity of α with respect to the independent variables, we follow a derivation similar as for the sensitivity of μ in the previous section. Figure 3.10 shows the dimensionless side force versus the negative dimensionless aligning torque for two side slip angles or, since φ only depends on α, two φ-levels φ and $\varphi + \Delta\varphi$. Again, additional curves can be created by multiplication of the original curve with respect to the origin.

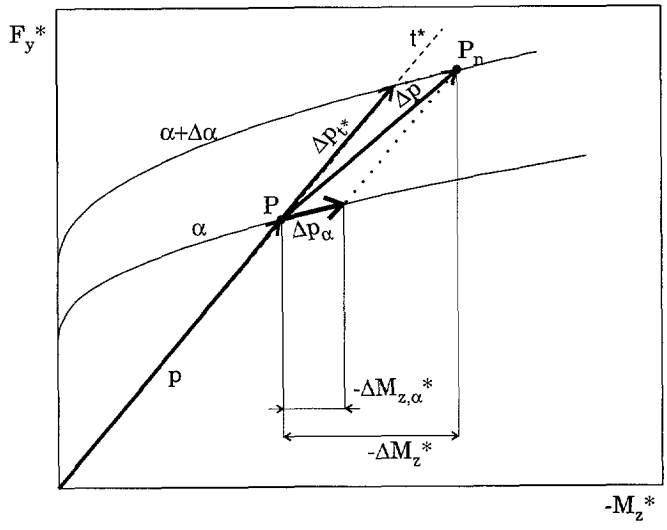

Figure 3.10: *Gough-diagram of dimensionless side force versus aligning torque for two side slip angles*

Once more, we have a point P and a point P_n, for which Eq. 3.38 holds. We derive

$$\Delta p_{t^*} = \frac{\Delta\varphi}{\varphi} p$$

$$\Delta p_\varphi = -\Delta M^*_{z,\varphi} \left[1 \quad \left. \frac{\partial F^*_y}{\partial\left(-M^*_z\right)} \right|_\varphi \right]^T \tag{3.50}$$

For the components of Δp we have

$$-\Delta M^*_z = \frac{\Delta\varphi}{\varphi}\left(-M^*_z\right) - \Delta M^*_{z,\varphi}$$

$$\Delta F^*_y = \frac{\Delta\varphi}{\varphi} F^*_y - \Delta M^*_{z,\varphi} \left. \frac{\partial F^*_y}{\partial\left(-M^*_z\right)} \right|_\varphi \tag{3.51}$$

and by elimination of $-\Delta M^*_{z,\varphi}$ we obtain

$$\Delta\varphi = \frac{\varphi\Delta F^*_y + \varphi\Delta M^*_z \left. \frac{\partial F^*_y}{\partial\left(-M^*_z\right)} \right|_\varphi}{F^*_y + M^*_z \left. \frac{\partial F^*_y}{\partial\left(-M^*_z\right)} \right|_\varphi} \tag{3.52}$$

so that for infinitesimally small Δ's we have

$$\frac{\partial\varphi}{\partial F^*_y} = \frac{\varphi}{F^*_y + M^*_z \left. \frac{\partial F^*_y}{\partial\left(-M^*_z\right)} \right|_\varphi} \tag{3.53a}$$

$$\frac{\partial\varphi}{\partial M^*_z} = \frac{\varphi \left. \frac{\partial F^*_y}{\partial\left(-M^*_z\right)} \right|_\varphi}{F^*_y + M^*_z \left. \frac{\partial F^*_y}{\partial\left(-M^*_z\right)} \right|_\varphi} \tag{3.53b}$$

The partial derivative $\partial F_y^* / \partial\left(-M_z^*\right)\Big|_\varphi$ in these expressions describes the slope of the tangent to the curve of constant side slip angle. Along this curve, the friction coefficient μ is the only running variable. Thus, we derive:

$$\left.\frac{\partial F_y^*}{\partial\left(-M_z^*\right)}\right|_\varphi = \frac{\left.\frac{\partial F_y^*}{\partial \mu}\right|_\varphi}{\left.\frac{\partial\left(-M_z^*\right)}{\partial \mu}\right|_\varphi} \tag{3.54}$$

Using the brush tyre model we find

$$\left.\frac{\partial F_y^*}{\partial \mu}\right|_\varphi = \left(\frac{\varphi}{\mu}\right)^2\left(3-2\frac{\varphi}{\mu}\right) \tag{3.55a}$$

$$\left.\frac{\partial\left(-M_z^*\right)}{\partial \mu}\right|_\varphi = 3\left(\frac{\varphi}{\mu}\right)^2\left(1-\frac{\varphi}{\mu}\right)^2 \tag{3.55b}$$

and the slope of the tangent to the curve of constant side slip angle becomes

$$\left.\frac{\partial F_y^*}{\partial\left(-M_z^*\right)}\right|_\varphi = \frac{\mu(3\mu-2\varphi)}{3(\mu-\varphi)^2} \tag{3.56}$$

We note that for $\mu \to \varphi$ (at $\mu > \varphi$), that is when the F_y-value becomes the peak value and total sliding is reached, the slope tends to ∞. For the theoretical case of $\mu \to \infty$, the slope becomes one. For $\mu = 1$, and assuming that $\mu > \varphi$, the slope attains a value depending on φ, equal to $\dfrac{3-2\varphi}{3(1-\varphi)^2}$. With Eq. 3.56, Eq. 3.53 now becomes

$$\frac{\partial \varphi}{\partial F_y^*} = \frac{3\mu^2}{6\mu^2-4\mu\varphi+\varphi^2} \tag{3.57a}$$

$$\frac{\partial \varphi}{\partial M_z^*} = \frac{\mu^3(3\mu-2\varphi)}{\left(6\mu^2-4\mu\varphi+\varphi^2\right)(\mu-\varphi)^2} \tag{3.57b}$$

For positive α we have

$$\varphi = \min\left(\frac{2}{3}c_p Q^2 \tan\alpha, \mu\right), \quad \alpha \geq 0,$$
$$\alpha = \operatorname{atan}\left(\frac{3\varphi}{2c_p Q^2}\right), \varphi \leq \mu \tag{3.58}$$

so that

$$\frac{\partial\alpha}{\partial\varphi} = \frac{6c_p Q^2}{4c_p^2 Q^4 + 9\varphi^2} \approx \frac{3}{2c_p Q^2} \tag{3.59}$$

where the approximation is quite reasonable for the (positive) working range of the tyre. Combining Eqs. 3.1, 3.48, 3.57 and 3.59, we finally find

$$\begin{aligned}\frac{\partial\alpha}{\partial F_y} &= \frac{\partial\alpha}{\partial\varphi}\frac{\partial\varphi}{\partial F_y^*}\frac{\partial F_y^*}{\partial F_y} \\ &= \frac{18\mu^2 c_p Q^2}{F_z\left(4c_p^2 Q^4 + 9\varphi^2\right)\left(6\mu^2 - 4\mu\varphi + \varphi^2\right)} \\ &\approx \frac{9\mu^2}{2c_p\alpha^2\left(6\mu^2 - 4\mu\varphi + \varphi^2\right)}\end{aligned} \tag{3.60a}$$

$$\begin{aligned}\frac{\partial\alpha}{\partial M_z} &= \frac{\partial\alpha}{\partial\varphi}\frac{\partial\varphi}{\partial M_z^*}\frac{\partial M_z^*}{\partial M_z} \\ &= \frac{6\mu^3 c_p Q^2(3\mu - 2\varphi)}{aF_z\left(4c_p^2 Q^4 + 9\varphi^2\right)\left(6\mu^2 - 4\mu\varphi + \varphi^2\right)(\mu - \varphi)^2} \\ &\approx \frac{3\mu^2(3\mu - 2\varphi)}{2c_p a^3\left(6\mu^2 - 4\mu\varphi + \varphi^2\right)(\mu - \varphi)^2}\end{aligned} \tag{3.60b}$$

$$\begin{aligned}\frac{\partial\alpha}{\partial F_z} &= \frac{\partial\alpha}{\partial\varphi}\left\{\frac{\partial\varphi}{\partial F_y^*}\frac{\partial F_y^*}{\partial F_z} + \frac{\partial\varphi}{\partial M_z^*}\frac{\partial M_z^*}{\partial F_z}\right\} \\ &= -\frac{9c_p Q^2\mu\varphi(3\mu - \varphi)}{F_z\left(4c_p^2 Q^4 + 9\varphi^2\right)\left(6\mu^2 - 4\mu\varphi + \varphi^2\right)} \\ &\approx -\frac{9\mu\varphi(3\mu - \varphi)}{4c_p\alpha^2\left(6\mu^2 - 4\mu\varphi + \varphi^2\right)}\end{aligned} \tag{3.60c}$$

The values that these partial derivatives take for $\tan(\alpha)$, or approximately for α, for the extreme values of μ and φ are laid down in Table 3.2.

	$\mu \to 0$	$\mu = \varphi$
$\partial\alpha/\partial F_y$	0	$3/C_{F\alpha}$
$\partial\alpha/\partial M_z$	0	∞
$\partial\alpha/\partial F_z$	0	$-\alpha/F_z$

Table 3.2: *Sensitivities for extreme values of μ*

These results are illustrated for a constant vertical load by the graphs in Figure 3.11.

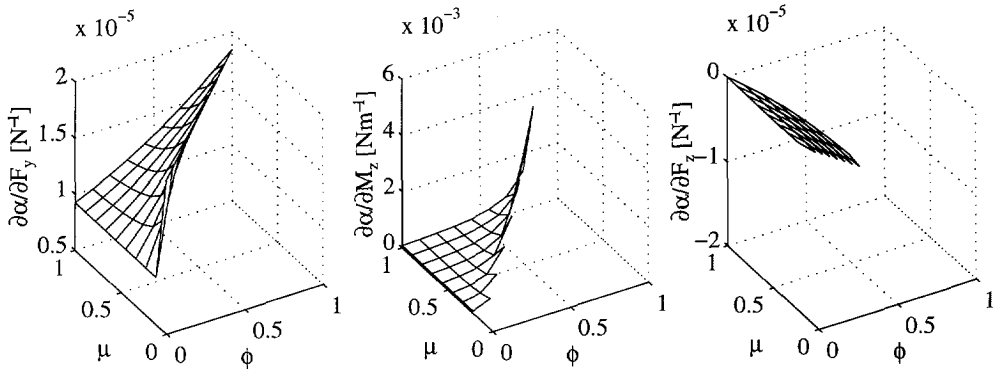

Figure 3.11: *Sensitivity of α-estimate with respect to the independent variables Fy, Mz and Fz at a constant vertical load*

In contrast to the sensitivities of the μ-estimate, the α-estimate is most sensitive to errors in the independent variables at total sliding. In the Gough-diagram (Fig. 3.10), this is the area along the y-axis where all the curves of constant side-slip coincide. The relative importance of the errors becomes more apparent in the next graph, Figure 3.12, using relative errors. Now it becomes clear that primarily the errors in side force affect the α-estimate.

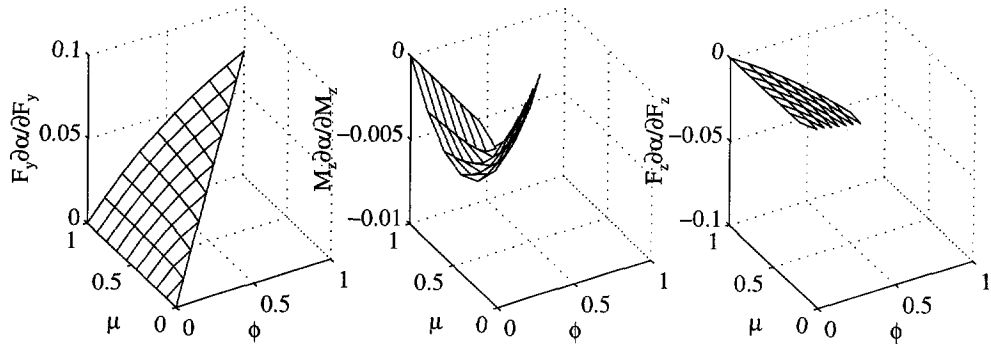

Figure 3.12: *Relative sensitivity of α-estimate with respect to the independent variables Fy, Mz and Fz at a constant vertical load*

3.2.4. Pure Longitudinal slip

The calculation of longitudinal force due to longitudinal slip is analogous to the calculation of side force due to side slip. The pure longitudinal force does not generate a self aligning moment. The pure longitudinal slip will be regarded as a special case of combined lateral and longitudinal slip.

3.2.5. Combined Lateral and Longitudinal Slip

In the case of combined lateral and longitudinal forces generated by the tyre, the lateral and longitudinal carcass stiffnesses of the tyre can no longer be neglected. Due to carcass deformations in these directions, the lines of action of the lateral and longitudinal forces are shifted. This gives rise to contributions to the self aligning torque in addition to the torque generated by side force as in the case of pure side slip. Expressions for combined slip for the simple brush tyre model will be derived under the assumption of isotropic friction coefficient μ and tread element stiffness c_p. Furthermore, we introduce the longitudinal and lateral carcass stiffnesses C_{cx} and C_{cy} respectively and we assume an infinite torsional stiffness of the carcass about the vertical axis. A top view of the contact line of the brush tyre model under combined drive and side slip is shown in Figure 3.13.

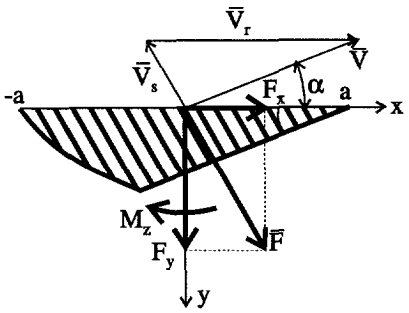

Figure 3.13: *Contact line of steady state combined slipping brush type tyre model*

In this figure, the wheel is thought to travel over the road surface with the total speed vector $\bar{V}$. The wheel is rotating around its y-axis causing the tread elements to travel through the contact area at a speed of $V_r = \Omega \cdot r_e$ in the direction of the wheel, where Ω is the rotational speed of the wheel and r_e is the so-called effective rolling radius. In this context r_e is considered to be a model parameter independent of the tyre slip, conform [42], but unlike for example [13]. Consequently, we have a slip speed vector $\bar{V}_s = \bar{V} - \bar{V}_r$. As long as the tread elements adhere to the road surface, they will deflect at the same rate as the total slip speed vector. In this analysis, all vectors can be decomposed into their components in x and y directions. Since $\bar{V}_r$ is always in x-direction, $V_{rx}=V_r$ and $V_{ry}=0$. We may now introduce a dimensionless slip vector

$$\bar{\sigma} = \begin{pmatrix} \sigma_x \\ \sigma_y \end{pmatrix} = \frac{1}{V_r} \begin{pmatrix} V_{sx} \\ V_{sy} \end{pmatrix} \tag{3.61}$$

The usual definition for the longitudinal slip reads

$$\kappa = \frac{-V_{sx}}{V_x} \tag{3.62}$$

By this definition of κ, κ is positive for positive longitudinal force (driving) and negative for negative longitudinal force (braking). For the side slip angle we have

$$\tan(\alpha) = \frac{-V_{sy}}{V_x} \tag{3.63}$$

so that the slip vector $\bar{\sigma}$ relates to κ and α by

$$\begin{aligned} \sigma_x &= \frac{-\kappa}{1+\kappa} \\ \sigma_y &= \frac{-\tan(\alpha)}{1+\kappa} \\ \sigma &= \sqrt{{\sigma_x}^2 + {\sigma_y}^2} \end{aligned} \tag{3.64}$$

The parameter φ is redefined as

$$\varphi = \frac{2c_p a^2 \sigma}{3F_z} \tag{3.65a}$$

or with Eq. 3.1,

$$\varphi = \frac{2}{3} c_p Q^2 \sigma \tag{3.65b}$$

In analogy to the case of pure side slip, the magnitude of the total force is given by

$$\begin{aligned} F &= \frac{1}{\mu^2} F_z \left(3\mu^2\varphi - 3\mu\varphi^2 + \varphi^3\right) \quad for \ \ \sigma \le \sigma_{sl} \\ F &= \mu F_z \qquad\qquad\qquad\qquad for \ \ \sigma > \sigma_{sl} \end{aligned} \tag{3.66}$$

Where $\sigma_{sl}$is the slip value at which total sliding starts,

$$\sigma_{sl} = \frac{3\mu F_z}{2c_p a^2} \tag{3.67}$$

Assuming isotrope stiffnesses, the direction of the force vector $\overline{F}$ is opposite to $\overline{\sigma}$

$$\overline{F} = \begin{pmatrix} F_x \\ F_y \end{pmatrix} = -F \cdot \frac{\overline{\sigma}}{\sigma} \tag{3.68}$$

and the components F_y and F_x are obtained by combining equations 3.66 and 3.68.

Without carcass compliance, the longitudinal force would not give any contribution to the self aligning torque. The self aligining torque would only be generated by the side force F_y acting at arm t, just as in the case of pure side slip

$$M_z' = -t \cdot F_y \tag{3.69}$$

$$t = \frac{a(\mu - \varphi)^3}{\mu\left(3\mu^2 - 3\mu\varphi + \varphi^2\right)} \tag{3.70}$$

However, deformation of the carcass due to the tyre forces shifts the working lines of F_y and F_x with respect to the contact centre, thus creating additional torques with respect to the vertical axis through the contact centre. This is illustrated by Figure 3.14, where the carcass stiffnesses are modelled by springs. Since no torsional compliance was assumed, only the aligning torque is affected by the carcass deflection.

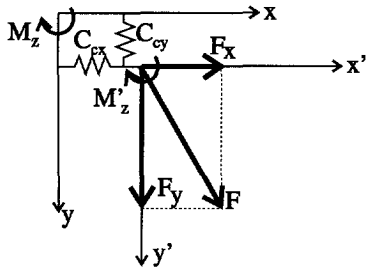

Figure 3.14: *Simplified effect of finite carcass stiffnesses to the brush tyre model*

In addition to the carcass deformation, even at zero side force the working line of the longitudinal force is usually offset from the center by a small distance s, possibly of the order of magnitude of 1 to 1.5 centimeters for passenger car tyres. A representation of both these phenomena which produces qualitatively good results is given by

$$M_z = M_z' + F_x F_y \left(\frac{\varepsilon_x}{C_{cx}} - \frac{\varepsilon_y}{C_{cy}} \right) + F_x s \tag{3.71}$$

where the factors $\varepsilon < 1$ have been introduced to account for forward and sideways rolling effects of the carcass [41]. At this point, it is worthwile to eliminate the dependence of the forces and torques on the vertical load. In analogy to 3.26, we define the dimensionless total planar force

$$F^* = \frac{F}{F_z} \tag{3.72}$$

and for the brush model under combined slip we have

$$\begin{aligned} F_x^* &= \frac{\sigma_x}{\sigma} F^* \\ F_y^* &= \frac{\sigma_y}{\sigma} F^* \end{aligned} \tag{3.73}$$

For the self aligning torque we derive

$$M_z^* = \frac{M_z}{aF_z} = -\frac{t}{a} F_y^* + \frac{1}{aF_z} \left\{ F_x F_y \left(\frac{\varepsilon_x}{C_{cx}} - \frac{\varepsilon_y}{C_{cy}} \right) + F_x s \right\} \tag{3.74}$$

Figure 3.15 shows F_y^* (solid) and F_x^* (dashed) versus α and M_z^* versus α for various friction levels at pure side slip (thick lines) and at a small value 0.4 % brake slip (thin lines). This figure illustrates that such a small amount of longitudinal slip while cornering has very little effect on the side force (not noticeable in the figure) but has a substantial effect on the self aligning torque due to the carcass compliance and to the offset s. It appears that M_z^* may even change sign. In the estimation

procedure for α and μ as described earlier, the longitudinal forces need to be taken into account in order to prevent erroneous results.

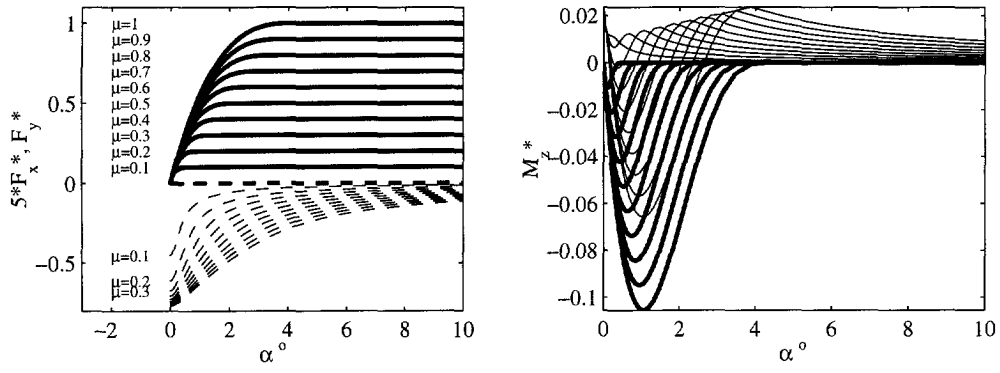

Figure 3.15: *Influence of small braking slip on side force and self aligning torque*

The next figure shows how Gough-plots change due to the combined slip. The plots have an extra dimension due to the longitudinal force, as shown in Figure 3.16. In this figure, a 0.4 % brake slip has been used as before.

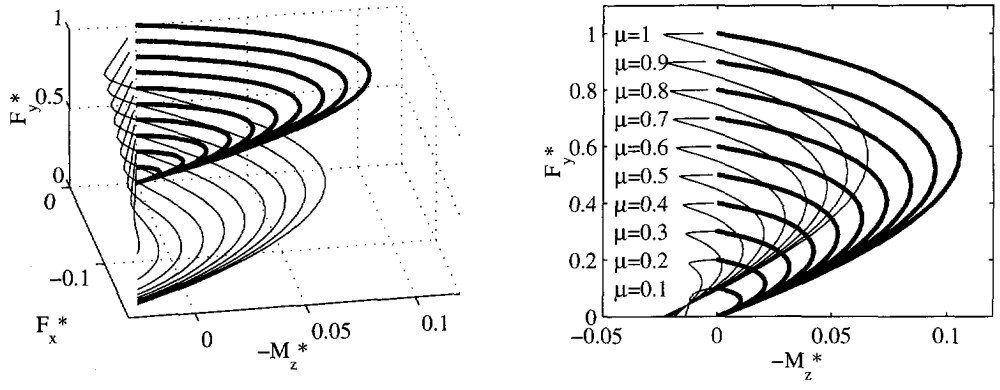

Figure 3.16: *Gough plot for combined slip at various friction levels in 3D-view (left) and in projection on the $M_z^* - F_y^*$ plane (right)*

As before, the curves of constant friction coefficient for pure side slip have been drawn with thick curves, while the curves of constant friction for the small brake

slip have been drawn with thin curves. The projection on the $M_z^* - F_y^*$ plane reveals how the Gough-plot for pure side slip has become distorted due to the combined slip.

The estimation of α, κ and μ can now be described as functions of three input variables F_x^*, F_y^* and M_z^*. We obtain

$$\begin{aligned} \alpha &= \alpha\left(F_x^*, F_y^*, M_z^*\right) \\ \kappa &= \kappa\left(F_x^*, F_y^*, M_z^*\right) \\ \mu &= \mu\left(F_x^*, F_y^*, M_z^*\right) \end{aligned} \tag{3.75}$$

As in the case of pure side slip, we have a unique solution (α, κ, μ) when there is some sliding in the contact area.

3.2.6. Camber

The effects of camber on the side force behaviour of the tyre may be easily understood by considering the left drawing of Fig. 3.17, showing a wheel subject to a camber angle γ, running along a straight line. For simplicity, the side slip angle is assumed to be zero. The right drawing of Fig. 3.17 is a top view of the contact line. In this projection, the bottom parts of the brush elements will follow the straight line due to adhering forces between the tread elements and the road surface, while the top parts of the brush element will follow part of an ellipsoid curve, namely the projection of the wheelcircle on the road (actually, the deflection of the brush elements will be less than what follows from this projection because of the laterally deflected carcass belt). Assuming generation of side force as a function of brush element deflection, as before, it is clear that the camber angle gives rise to a side force on the tyre, even at zero side slip angle. However, this analysis does not explain the generation of aligning torque by camber.

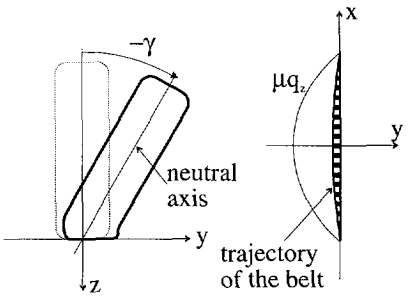

Figure 3.17: *Cambered wheel in front view(left) and contact line in top view (right)*

To understand the aligning torque behaviour with camber, the tyre width has to be taken into account. Suppose we have a cambered wheel running over a straight course (Fig. 3.17). Considering a contact patch of finite length and width, it is easily understood that owing to the varying rolling radius over the contact width, differences in circumferential velocity will arise in the contact patch. Since the forward speed of the tyre is forced to be the same over the width of the tyre, opposite longitudinal slips will arise at both sides of the neutral axis. In conjunction with the friction between the tread elements and the road surface and the tread stiffness in longitudinal direction, this gives rise to a twisting couple around the vertical axis of the tyre. This couple is present even at zero side slip angle.

A rough analysis using a simple discrete brush tyre model with tyre width [20] shows the effects of camber qualitatively (Fig. 3.18). A more thorough discussion of the phenomena related to static and dynamic camber behaviour can be found in [28]. Obviously, the offsets from zero of the side force and the aligning torque are to be taken care of in the friction estimation procedure. It should also be noted however, that the effects of camber on automobile tyres are relatively small compared to the effects of side slip angle. Moreover, camber angles imposed on automobile tyres do not usually exceed a magnitude of 5 degrees.

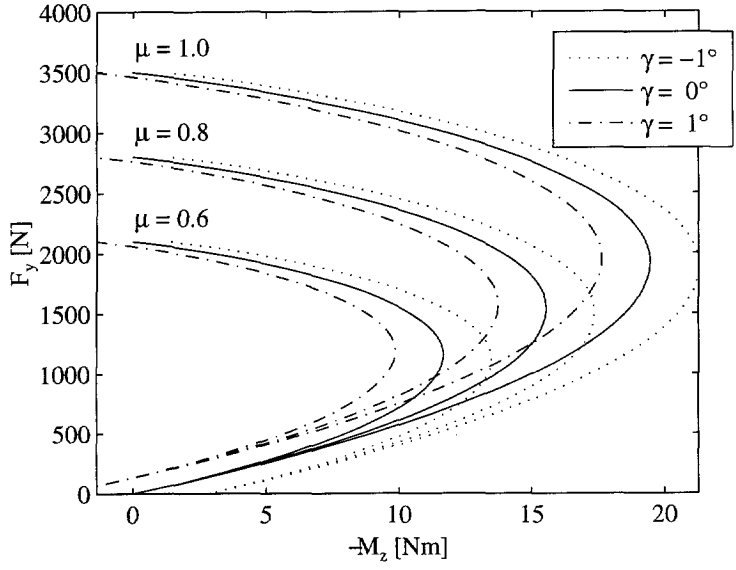

Figure 3.18: *Effects of camber on side force and aligining torque in a Gough-plot*

3.3. Friction Estimation using the Delft Tyre Model

3.3.1. The Delft Tyre Model

The Delft Tyre Model (DTM), also known as Magic Formula Tyre Model, is an empirical tyre model, which means that it is built to describe measured tyre data as closely as possible, rather than being built on tyre modelling theory. The first version of this model was presented in 1987 [4], and since then, the DTM has been updated frequently. The 1997-version is described in [44]. The base form of the formula for pure slip reads

$$y = D\sin\Big[C\operatorname{atan}\big\{Bx - E\big(Bx - \operatorname{atan}(Bx)\big)\big\}\Big] \tag{3.76}$$

with

$$\begin{aligned} Y(X) &= y(x) + S_v \\ x &= X + S_h \end{aligned} \tag{3.77}$$

where Y is the output variable F_x or F_y, and correspondingly X is the input variable κ or α and

B: stiffness factor
C: shape factor
D: peak value
E: curvature factor
S_h: horizontal shift
S_v: vertical shift

The behaviour of Eq. 3.76 is easily explained by first noticing that the base form of this formula is a sine function, scaled by a factor D, equal to μF_z where μ is a function of F_z, which determines the peak value. The argument of the sine is controlled by the arctangent function, which is bounded by $[-\pi/2, \pi/2]$, multiplied by a factor C. Thus, this factor C determines to what extent the sine function is used. For small values of x, $\operatorname{atan}(Bx) \approx Bx$ so the term multiplied by E is not significant and the product BCD forms the longitudinal or lateral slip stiffness. The factor B scales the input variable x and the factor E determines the shape around the peak of the curve.

The calculation of the aligning torque for pure side slip is executed by calculating the product of pneumatic trail and side force and adding a term for residual torque:

$$M_z = -t \cdot F_y + M_{zr} \tag{3.78}$$

The pneumatic trail is calculated by the counterpart of Equation 3.76:

$$t(\alpha_t) = D_t \cos\Big[C_t \operatorname{atan}\big\{B_t\alpha_t - E_t\big(B_t\alpha_t - \operatorname{atan}(B_t\alpha_t)\big)\big\}\Big] \tag{3.79}$$

$$\alpha_t = \alpha + S_{Ht} \tag{3.80}$$

Although these formulae only describe the pure slip case, the DTM is capable of describing the tyre characteristics when subjected to both pure and combined slip, as described in [44], with or without the presence of camber, and is therefore suitable to describe the actual behaviour of the tyre in this research. However, the DTM itself is outside the scope of this thesis and is used only as a tool.

The different cases of pure and combined slip will be described in analogy to section 3.2. Note that, because the brush tyre model used hypothetical parameters, while the DTM model uses actual tyre parameters optimized for a specific tyre, the graphs in this section can only be compared to those of section 3.2 qualitatively.

3.3.2. Pure Side Slip

In analogy to Figure 3.2, Figure 3.19 shows side force vs. slip angle for various friction levels for the case of pure side slip and zero camber at positive slip angles only and without residual forces and torques.

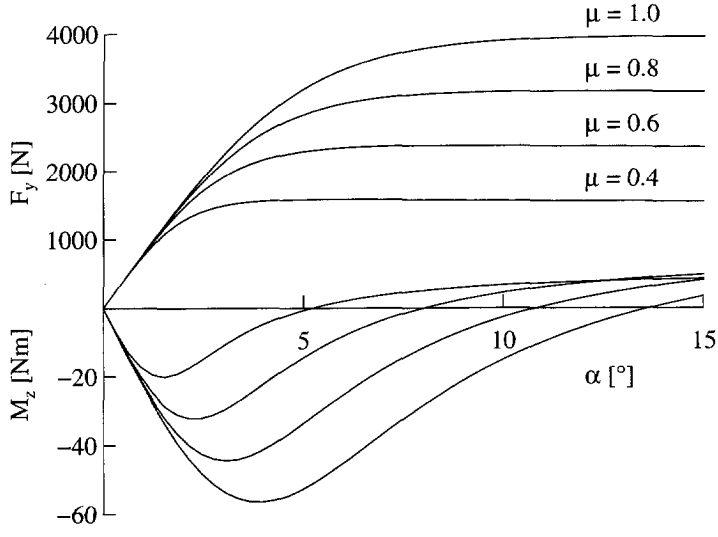

Figure 3.19: *Side force and aligning torque versus side slip at various friction levels for pure side slip*

Comparing this figure to Figure 3.2, it becomes clear that the tyre behaviour is not essentially different from the brush tyre model for these conditions. Once again, a pair of values F_y and M_z corresponds to a pair of α and μ. This is again presented in Figure 3.20 in a Gough-plot, similar to Figure 3.3.

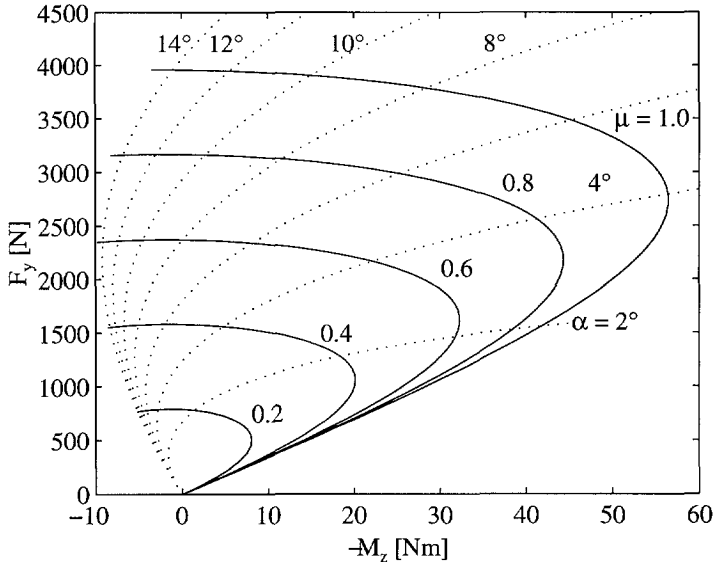

Figure 3.20: *Gough plot for various friction levels*

In analogy to section 3.2.2, we may try to find a curve invariant to load or friction coefficient. However, it is much more complicated than in the case of the brush tyre model, for various reasons. For example, the friction coefficient is load dependent and the tyre behaviour is asymmetrical with respect to slip angle. Considering positive slip angles only, and setting residual forces and torques to zero, a bundle of curves such as in Figure 3.21 can be constructed.

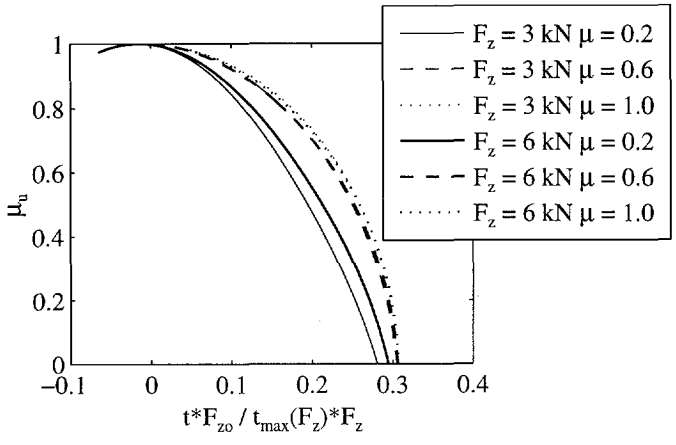

Figure 3.21: *Normalised side force against normalized pneumatic trail (DTM) for different values of F_z and μ.*

In this figure, the side force has been normalized for load and friction, where the friction is a approximately second order function of load. Thus, we have the utilized friction at the y-axis. This load dependency has also been accounted for on the x-axis. However, even with the applied restrictions and corrections, the curves for different values of load and friction are still fairly widely spread, especially as a function of μ, and therefore this result is considered to be of little value to use as a basis for the estimation of μ.

3.3.3. Residual Forces and Torques

So far residual forces and torques have not been considered. Since they are relatively small, it may be safely assumed that they are generated by adhesion friction only and thus independent of the friction coefficient, as shown in Figure 3.22.

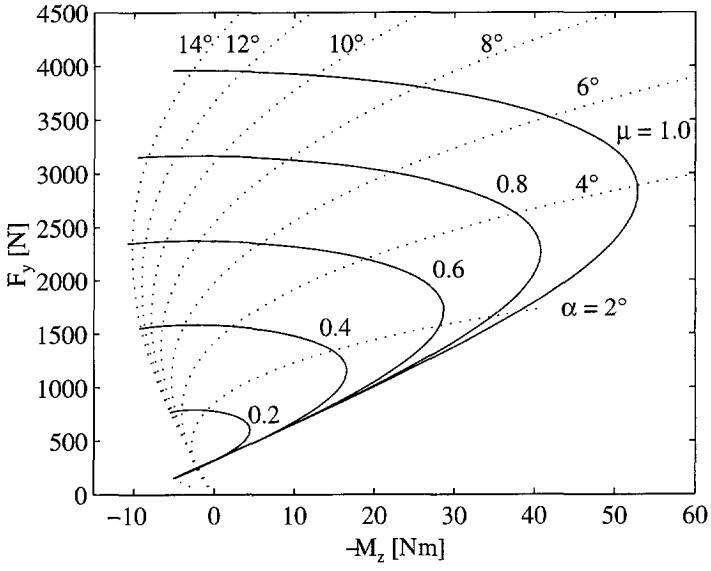

Figure 3.22: *Gough plot for various friction levels, including residual forces and torques (DTM)*

For the friction estimation method, they represent small shifts that have to be taken care of, especially for small slip angles. Only for very small friction coefficients will a considerable proportion of the total friction potential be uitlized by the residual forces and torques. In this case, the residual forces and toruqes induce sliding in the contact patch and consequently become dependent of the friction coefficient. In the extreme case of zero friction, the residual forces and torques vanish completely. (N.B.: the scaling factors in the expressions for the residual

forces and torques of the DTM'97 had to be changed for these purposes, because they erroneously assumed a linear dependency of the residual forces and torques on the friction coefficient. For our purposes, the residual forces are assumed to be independent of the friction coefficient as long as they do not exceed the total available friction potential μF_z).

3.3.4. Pure Longitudinal slip

As described previously, friction estimation using the method developed in section 3.2 is not possible in the case of pure longitudinal slip and will be given no further consideration in this thesis.

3.3.5. Combined Lateral and Longitudinal Slip

As in Figure 3.15 for the brush tyre model, side force and longitudinal force can be plotted versus side slip angle at various friction levels and small longitudinal slip values. A Gough plot can also be made for the DTM model at combined slip (Figure 3.23).

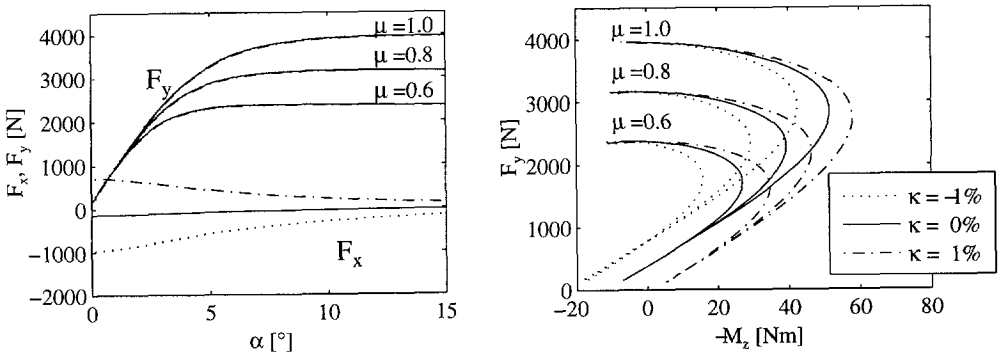

Figure 3.23: *Lateral and longitudinal forces versus side slip angle (left) and a Gough plot for three friction levels and small longitudinal slip values (right)*

3.3.6. Camber

Influence of camber is considered in Figure 3.24. This figure shows that small camber angles result in shifts of the curves. These shifts are relatively more important at low levels of side force and aligning torque. Again, this behaviour is in accordance with the brush tyre model behaviour at camber (Figure 3.18).

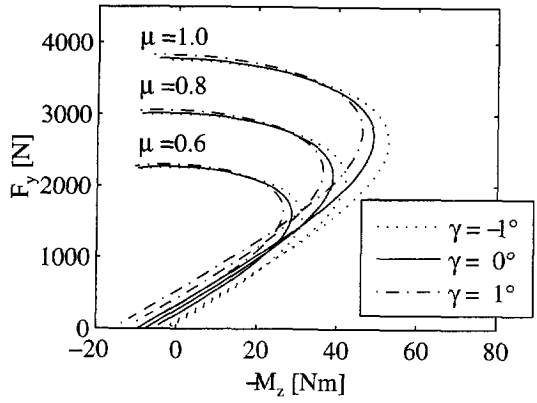

Figure 3.24: *Gough plot for three friction levels and small camber angles*

3.4. Tyre Transient Behaviour

In this research, low frequency dynamic phenomena only may be of interest. The most important low frequency dynamic behaviour of the tyre is caused by the relaxation length. Usually, the transient behaviour of the tyre due to the relaxation length l_{rel} is modeled as a first-order low-pass filter on the side slip angle α in the case of side slip or on κ in the case of longitudinal slip. Before the forces are calculated in a steady state tyre model (Fig. 3.25), the slip passes this filter.

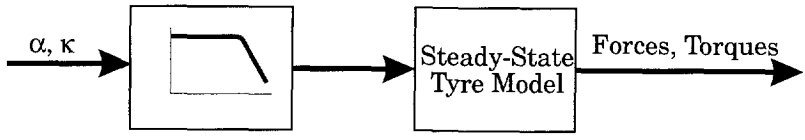

Figure 3.25: *Modeling of relaxation length behaviour*

The transfer function of the filter reads:

$$H(s) = \frac{1}{\tau s + 1} \tag{3.81}$$

The time constant τ is defined as

$$\tau = \frac{l_{rel}}{V} \tag{3.82}$$

The relaxation length mainly depends on the vertical load. A typical value of l_{rel} for a mid size passenger car tyre for side slip is 0.60 [m] at a vertical load of 4000 [N].

At a speed of 20 [m/s] this results in a time constant τ of 0.030 [s] and a bandwidth of the first order lag filter of 5.3 [Hz].

Clearly, this transient behaviour is of minor importance at moderate and high speed on smooth road surfaces; at low speed or at uneven roads however, it may become important.

3.5. Conclusions of this chapter

The brush tyre model was derived for pure side slip and combined side and longitudinal slip. It was found that in the case of pure side slip both the side slip angle and the friction coefficient can be calculated from the side force and the aligning torque for a given load and tyre model parameters provided there is partial sliding of the brush elements in the contact patch. If there is no sliding in the contact area at all, the side slip angle can be estimated, but the friction coefficient cannot be estimated. On the other hand, if there is total sliding, only the friction coefficient can be estimated.

The sensitivity analysis revealed that the friction estimate is primarily sensitive to measurement errors in the case of complete adhesion. In that case the sensitivity of the friction estimate to inaccuracies in the determination of the self aligning torque is prominent. The side slip angle estimate is primarily sensitive to measurement errors in the case of pure sliding. The sensitivity of the side slip angle estimate to errors in the determination of the side force is the largest.

The sensitivity of the estimation method to common disturbances, such as combined slip, camber and residual forces and torques, and measurement inaccuracies, was investigated qualitatively. Small longitudinal forces primarily disturb the self aligning torque, which in turn has a major influence on the friction estimate. Camber and residual forces and torques mainly cause shifts of the curves in the Gough-diagram that have to be accounted for.

The Delft Tyre Model that represents the actual tyre behaviour more closely, essentially shows the same behaviour as the brush tyre model with respect to the possibilities to estimate the side slip angle and the friction coefficient.

For these reasons, it is concluded that within the constraints imposed by the physical nature of the tyre, the tyre can be used as a sensor to estimate side slip and friction coefficient. However, the effectiveness of the estimator depends on the driving conditions. Moreover, care has to be taken with respect to the sensitivities of the estimates to measurement inaccuracies and disturbances.

4 Identification Methods

4.1. Introduction

The previous chapter outlined a procedure to estimate side slip angle α and the friction coefficient μ from measured tyre forces and torques, based on steady-state tyre behaviour. It was shown that the tyre dynamics are of little importance in this research. Accordingly, this chapter focuses on methods to identify the steady-state properties of the tyre behaviour. The identification of the transient tyre behaviour has not been considered in this research, but has been subject of other research, e.g. [28].

Using the available tyre models, e.g. the simple brush tyre model or the Delft Tyre Model (DTM) used in Chapter 3, tyre forces and torques can be calculated as functions of load, side slip, longitudinal slip, camber and friction coefficient. However, the inverse functions cannot be derived analytically. Numerical methods can fill this gap to some extent.

Two different approaches, a table look-up method and a neural network approach will be discussed. Both methods use some form of knowledge of the tyre at hand. In the case of table lookup it is laid down in the table entries, in the case of neural networks it is represented by the neural network weights.

4.2. Table look-up method

For the table lookup method, the steady-state tyre behaviour is assumed to be known and laid down in a table that needs to span the entire working range of the tyre. Assuming we would like to find α and μ from measured variables F_z, F_y, M_z and γ, a four-dimensional table filled with a huge amount of data would be needed. This has to be considered unrealistic. Fortunately, the size of the table can be

reduced by defining a set of nominal conditions for load and camber for which the now two-dimensional table has to be created. These nominal conditions refer to a moderate vertical load and zero camber angle. Actually, the table obtained contains the information of one Gough-plot such as Figure 3.3.

The first step in the estimation procedure now consists of transformation of the measured data to the nominal conditions for which the table is valid. This can be done using the so-called similarity method [42]. This method is also partially implemented in the DTM to facilitate simulation of different friction levels. It is based on the assumptions that the maximum side force is proportional to the product μF_z, while the cornering stiffness at zero side slip angle depends only on F_z and not on μ. The influence of camber (limited to small angles) is represented by shifting the curves of F_y and M_z versus α horizontally. It has been shown in Chapter 3 that these shifts are the main effects of small camber angles. The formulae read:

$$F_y = \frac{\mu F_z}{\mu_0 F_{z,0}} F_{y,0}\left(\alpha_{F_{eq}}\right) \tag{4.1}$$

$$M_z = \frac{\mu F_z}{\mu_0 F_{z,0}} \frac{C_{M\alpha}(F_z)}{C_{M\alpha_0}} \frac{C_{F\alpha_0}}{C_{F\alpha}(Fz)} M_{z,0}\left(\alpha_{M_{eq}}\right) \tag{4.2}$$

$$\begin{aligned} \alpha_{F_{eq}} &= \frac{\mu_0 F_{z,0}}{\mu F_z} \frac{C_{F\alpha}(F_z)}{C_{F\alpha_0}} \left(\alpha + \frac{C_{F\gamma}(F_z)}{C_{F\alpha}(F_z)}\gamma\right) \\ \alpha_{M_{eq}} &= \frac{\mu_0 F_{z,0}}{\mu F_z} \frac{C_{F\alpha}(F_z)}{C_{F\alpha_0}} \left(\alpha - \frac{C_{M\gamma}(F_z)}{C_{M\alpha}(F_z)}\gamma\right) \end{aligned} \tag{4.3}$$

where the *0*-subscript stands for the nominal condition, $C_{F\alpha}(F_z)$ and $C_{M\alpha}(F_z)$ are the cornering and aligning torque stiffnesses depending on load respectively, and $C_{F\gamma}(F_z)$ and $C_{M\gamma}(F_z)$ are the cornering and aligning torque camber stiffnesses, also depending on load, respectively. The similarity method holds true for the simple brush tyre model, but is only approximately true for actual tyre behaviour.

The second step consists of looking up the friction coefficient μ and side slip angle α for the transformed data.

An interesting issue is the creation of the table. For the set of nominal conditions, a table of the nonlinear mapping is made:

$$\left(F_y, M_z\right) = f_{F_y,M_z}(\alpha,\mu) \tag{4.4}$$

where $f_{F_y,M_z}(\alpha,\mu)$ describes the mapping at nominal conditions of vertical load and camber. This nonlinear mapping may be known for example in the form of the DTM. The position in the table represents the output variables (F_y and M_z) of the

mapping while the entries of the table contain the input variables (α and μ), which means two values in each entry in this two-dimensional case. If the values of α and μ are taken from a regularly spaced grid, say in a linear range of -15 to 15 degrees for α and 0 to 1.2 for μ, the output variables will not have values on all points of a regularly spaced grid for the output variables, as shown in Fig. 4.1. (In this figure, the grid points have deliberately been widely spaced to have distinct points in the graphs.)

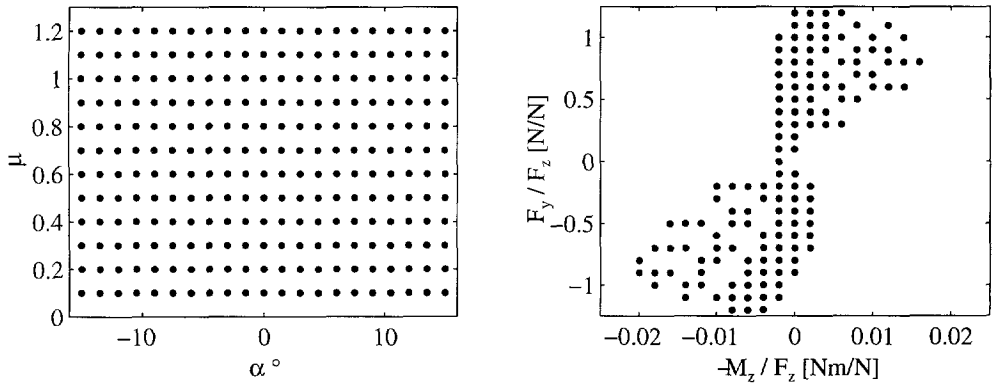

Figure 4.1: *Scatter plot of input values (left) and output values (right) using regularly spaced input values*

It is possible to use the sparsely filled table directly, and use some kind of interpolation at the time of actual lookup if an undefined point in the table is to be calculated. For example, the inverse of the Euclidean distance to the surrounding points can be used as weights for an average.

Alternatively, we could try to fill the table completely [60]. Since the inverse function $f^{-1}_{F_y,M_z}(\alpha,\mu)$ is not known, it is not possible to simply calculate the necessary input values to obtain a regulary grid of output values. A first, simple method to fill the empty positions in the table is by randomly generating input values and calculate their corresponding output values. Thus, a considerable number of gaps in the table will be filled, as shown in Figure 4.2. The remaining gaps can be filled by interpolation or by iteratively determining the corresponding input values. Some areas in the table will appear to be quite impossible to fill using the available input domain. If the chosen input domain is representative for the actual situation, it can be safely assumed that it is very unlikely that these output values will ever be reached. They can either be disregarded or filled by interpolation or extrapolation.

Once the table has been created, the actual lookup in the table may be realised by simply taking the nearest grid point to the desired output values and reading out the corresponding input values, or by interpolating the grid to the desired output values and correspondingly interpolate the table entries.

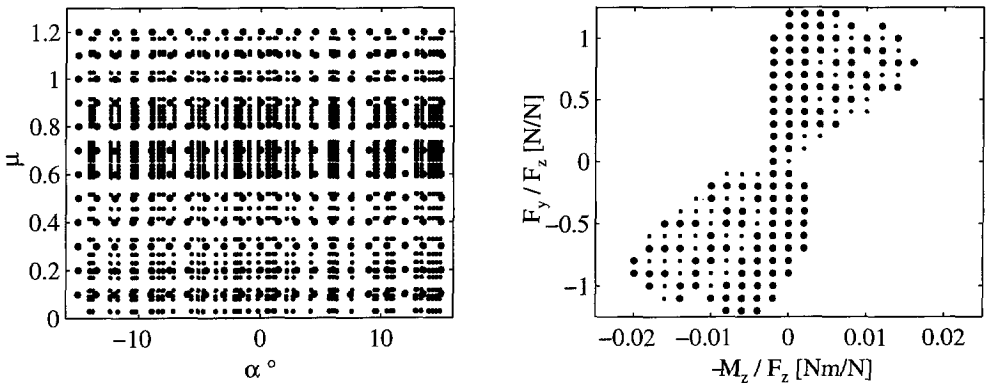

Figure 4.2: *Scatter plot of input values (left) and output values (right) using regularly spaced input values (large dots) and random input values (small dots)*

The table lookup method has been used in actual friction identification experiments [47], but it is rather cumbersome. Moreover, the assumptions made in using the similarity method do not hold over the entire working range of tyres, as remarked earlier.

4.3. Neural Networks

4.3.1. Introduction

Owing to their learning and non-linear input-output mapping capability, Artificial Neural Networks (ANN's or just NN's) have become increasingly popular in automotive research (see e.g. [39] on four-wheel steering, [46] on tyre modelling, [45, 66] on prediction of road friction coefficient, [37] on active suspension or [68] for a survey of neural network and fuzzy logic applications to vehicle systems). The original motivation for the development of neural networks stems from studies of the human nervous system. However, the development of artificial neural networks has diverged in many directions since then. Neural networks nowadays form a field of extensive investigations in which a vast variety of different kinds of neural networks have been developed, resulting in numerous publications. Without trying to cover this entire field of research in neural networks, we briefly discuss the theory of the most popular type of neural networks, the feedforward networks, and

then move on to the application of ANN's in this research. The interested reader is referred to [27], [51] and [56] for more elaborate discussions on neural networks while [10] describes the MATLAB Neural Network Toolbox, which has been used and adapted in this research extensively.

4.3.2. Neural Networks and Statistics Terminology

Part of the distrust of many engineers and scientists towards neural networks is probably due to the confusing terminology. Stemming from a different origin, researchers in neural networks have quite often reinvented concepts and created new terminology for already existing concepts in statistics. A short list of some more or less equivalent terms used in statistics and neural network applications is given by Table 4.2 [39, 58, 59].

statistics	neural networks
model	network
estimation, model fitting, optimisation	training, learning, adaptation
regression	supervised learning, mapping, function approximation
interpolation	generalisation
observations	training set
parameters	weights
overfit	overtraining
independent variables, predictors, regressors, explanatory variables	inputs
dependent variables, predicted values, response	outputs, target variable
residuals	errors
iteration	epoch
ridge regression	weight decay

Table 4.1: *Equivalent terms in statistics and neural networks*

4.3.3. Feedforward Neural Networks for Function Approximation

Neural networks have been applied in various areas of research, such as nonlinear on-line control, pattern recognition and research of the human brains. In this research, they are used for function approximation, or in statisticians' terminology, nonlinear regression. That is, a function is learned from examples presented by a teacher.

For function approximation, the Multi-Layer Perceptrons (MLP's) and Radial Basis Function (RBF) networks are most commonly used. They both provide a mapping from an input space to an output space, and they have been proven to be universal approximators of continuous non-linear functions [27, 56]. This means they can approximate such functions to arbitrary precision, provided the network has sufficient free parameters.

Multi-Layer Perceptrons

Multi-layer feedforward networks (or Multi Layer Perceptrons, MLP's for short) consist of nodes grouped in layers, connected to each other in one direction. The connections contain weight factors that form the free parameters of the network. There is an input and an output layer and usually (but not necessarily) one or more hidden layers (Fig. 4.3).

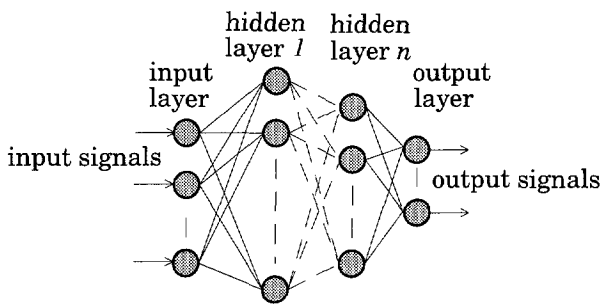

Figure 4.3: *General structure of a Multi-Layer Perceptron*

The input layer just passes the input signals through to the nodes of the next layer(s). At each node of the network, except for nodes in the input layer, the signals from the previous layer (possibly the input layer) are weighted with their respective weights and summed. If needed, a bias is added to the summed signal. Then the summed signals are fed through the so called activation function and passed to the next layer, and finally to the output layer. This leads to the following general input-output relation of an MLP with one hidden layer and with one type of activation function for each layer, describing the output vector y as a function of the input vector x:

$$y = f_o(b_o + W_o \cdot f_h(W_h \cdot x + b_h)) \tag{4.5}$$

where f_o and f_h are the activation functions and b_o and b_h the bias vectors of the output and the hidden layer respectively. W_o is a matrix of weights connecting the hidden layer to the output layer while W_h is a matrix of weights connecting the input layer to the hidden layer. Equation 4.5 can be easily extended for more hidden

layers, as well as for 'skip-layer' connections, e.g. from input layer directly to output layer.

Activation functions

The activation functions may be linear or non-linear. As already remarked, the nodes in the input layer just distribute the inputs to nodes in the subsequent layers. If the network has to learn a non-linear input-output mapping, at least some of the nodes in the subsequent layers need to contain non-linear activation functions. The linear activation function simply reads

$$f(x) = x \tag{4.6}$$

while popular choices for non-linear activation functions are sigmoid functions such as the logistic function

$$l(x) = \frac{e^x}{1+e^x} = \frac{1}{1+e^{-x}} \tag{4.7}$$

having an output range of [0,1], and the hyperbolic tangent function

$$h(x) = \frac{e^x - 1}{e^x + 1} = \frac{1 - e^{-x}}{1 + e^{-x}} \tag{4.8}$$

having an output range of [-1, 1]. The hyperbolic tangent function can be regarded as a scaled version of the logistic function, since

$$h(x) = 2l(x) - 1 \tag{4.9}$$

Figure 4.4 shows both sigmoid type activation functions.

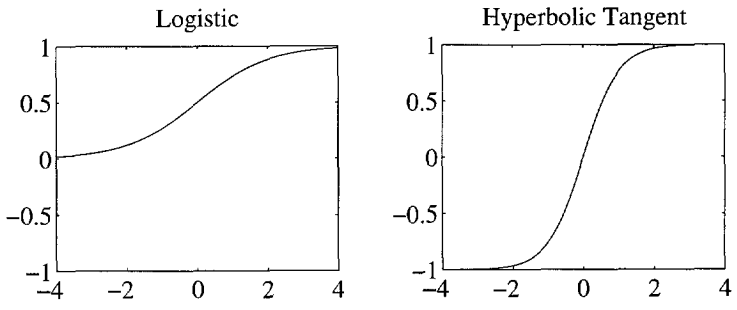

Figure 4.4: *Sigmoid type activation functions*

For continuous function approximations, linear activation functions are usually used in the output layer. This enables the network to have outputs outside the output range of the activation functions in the hidden layers. In principle, the choice of activation function is free, but the activation functions shown seem to be suitable

for most function approximation purposes. Conveniently for computations, but not necessarily, the activation functions are usually chosen to be the same for all nodes in a specific layer.

Network Design

The design of multi-layer feedforward networks involves a number of choices, such as the number of hidden layers, the number of nodes per layer and the kind of activation functions in the nodes. It has been mentioned earlier that it has been proven that MLP's with one hidden layer containing sigmoid type activation functions are universal approximators, provided that enough hidden nodes are applied [27, 56]. However, it may be that in some cases far less nodes, and consequently far less parameters, are needed if they are grouped in more than one hidden layer.

This happens to be the case for the mapping of side force and self-aligning torque to friction coefficient for the DTM tyre model. For positive values of α and μ-values ranging from 0 to 1.2, side force and aligning torque were calculated at a constant load of 4000 N using the DTM. The inverse mapping from side force and aligning torque to friction coefficient has to be learned by an MLP. The left graph of Figure 4.5 shows the true values. On this surface, 100 points were randomly chosen for training set, while test set was chosen as a regular grid. The right graph shows the result of the MLP with 5 nodes in the first and 2 nodes in the second hidden layer, both layers containing sigmoid activation functions. The graph has been cut off at the vertical axis at the level of μ=1.5. This network with 30 free parameters results in a standard deviation of the error on the training set of 0.0038 and on the test set of 0.0138 (the meaning of training and test set will be explained later). This result could not be achieved with a single hidden layer and the same number of free parameters. The difficulty of this particular mapping is the very steep rise of μ near the origin.

Further complications arise if different activation functions are allowed within one layer and if the connectivity between nodes is made variable, for example by allowing direct connections between two non-consecutive layers. The number of possible network architectures thus becomes immense. The best choice of network design depends on the problem at hand. Unfortunately, there are no well-proven rules on how to make these choices. The choices are usually made based on experience and subjective rules of thumb and of course much trial and error is involved. A number of methods have been developed to try to tackle the problem, such as cutting links, removing hidden nodes and changing regularisation parameters [56]. Another approach is to use a Genetic Algorithm to choose the optimum network architecture by optimisation. This approach will be discussed in Section 4.3.6.

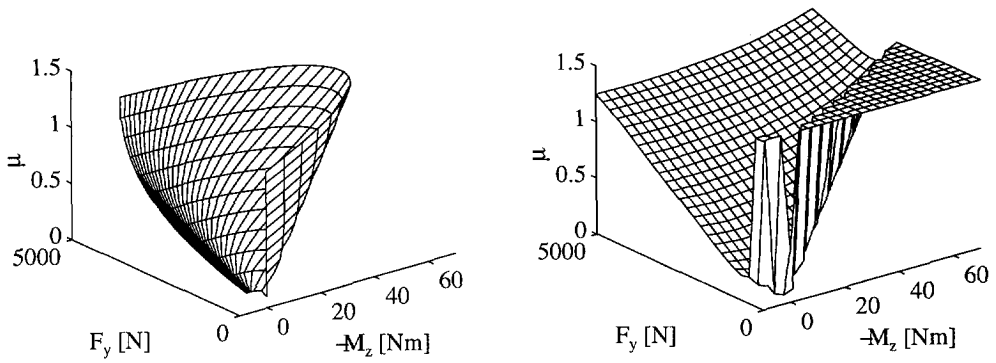

Figure 4.5: *Two-hidden-layer neural network approximation of the DTM. True values in the left graph, neural network approximation in the right graph.*

Network Training

Once the structure of a network has been chosen, the weights and biases of the network have to be optimised such that the error between the network output and the training data is minimised. Usually, the squared error summed over all training samples and over all outputs is used as the criterion for minimisation.

We distinguish online, or sequential training and offline, or batch training. In online training, the weights of the network are adjusted to each data sample, one at a time. In batch processing, all training data are repeatedly available at the same time. Apart from the cases where the training has to be online by the nature of the problem in question, it is also suggested that online training converges faster in cases where the training data consist of a large number of similar examples. In that case, we may expect the weights to converge before the entire set is used for training. However, we could achieve the same effect by taking a small sample of the training data and use that for batch training.

In neural network research, training is traditionally done by some variation on the back-propagation algorithm. This method is suitable for both online training and batch training, but it is notoriously slowly converging. For batch processing, often the Levenberg Marquardt algorithm is much more efficient than the back-propagation algorithm, and has been used in this research primarily. More details on both training algorithms can be found in virtually all textbooks on neural networks, for example in [8].

Both algorithms use the gradients of the activation functions. It is therefore desirable to have activation functions that are continuously differentiable. Differentiation of the logistic function (Eq. 4.7) with respect to x yields

$$\frac{dl(x)}{dx} = \frac{e^x}{\left(1+e^x\right)^2} = l(x)(1-l(x)) \tag{4.10}$$

while differentiation of the hyperbolic tangent function (Eq. 4.8) yields

$$\frac{dh(x)}{dx} = \frac{2e^x}{\left(1+e^x\right)^2} = h(x)(1-h(x)) \tag{4.11}$$

which explains some part of the popularity of sigmoid-type activation functions. If the activation functions are not continuously differentiable, the Nelder-Mead algorithm may be useful.

Since the weights are determined iteratively, starting values for the weights are needed. If sigmoid type activation functions are employed, these initial weights are usually small, randomly chosen numbers. They need to be small to prevent the optimisation from starting out in the saturation region of the activation functions.

The gradient based optimisation methods all find local optima. Although this is usually not a severe problem, there is also considerable interest in finding the global optimum. One method to try to accomplish this is by doing the optimisation several times starting at different randomly chosen points. Alternatives are so-called global optimisation methods, such as simulated annealing and genetic algorithms. These methods are usually much more computationally demanding, but, since these methods are not based on gradients, the activation functions do not need to be continuously differentiable. Section 4.3.6 will discuss genetic algorithms in some more detail.

Radial-Basis Function Networks

Radial-Basis Function (RBF) networks form a special class of feedforward neural networks. As in the case of MLP's, they can learn arbitrary mappings. The architecture of RBF networks usually involves three different layers. The first layer consists of source nodes, just like the MLP's. The second layer is a hidden layer that usually contains many nodes. It is possible, but uncommon, to use more than one hidden layer. The output layer usually consists of linear nodes, although other activation functions are possible.

The hidden units in a RBF network contain radial basis functions. Typically, their output decreases (or increases) monotonically with the distance from their centre. A popular RBF is the Gaussian function:

$$g(x) = \exp\left(\frac{(x-c)^2}{r^2}\right) \tag{4.12}$$

where c is the centre and r is the radius. Gaussian-like functions are local in the sense that they only give significant response in the neighbourhood of their centres. In contrast, there are also multiquadric-type RBF's (equation 4.13), that have global responses.

$$m(x) = \frac{\sqrt{r^2 + (x-c)^2}}{r} \tag{4.13}$$

Figure 4.4 shows both types of RBF's for the radii r=1, 0.5 and 2.0 at the centre $c = 0$. The multiquadric functions are only rarely used and will not be considered here. So, we will assume to have Gaussian RBF's only.

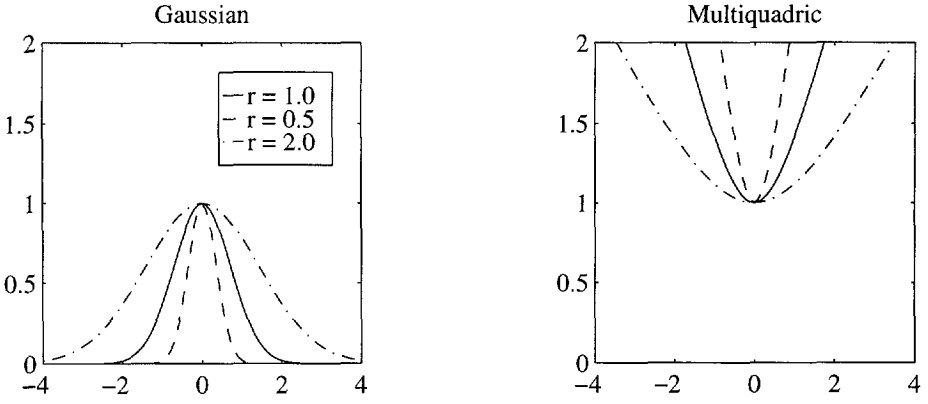

Figure 4.6: *Radial Basis Functions*

The Gaussian RBF's such as defined by Eq. 4.12 need specification of the centre c and the radius r. Various methods of choosing the centre include centres for each training example, which easily leads to overfitting, placing centres over a regular grid, using clustering methods to choose representative centres for the training set, and using the first principal components as the centres. The radii are usually chosen such that the 'tails' of the 'bumps' of the RBF's are slightly overlapping.

In [27], a comparison has been made between RBF networks and MLP's. Firstly, it is remarked that both RBF networks and MLP's are nonlinear layered feedforward networks. They are both also universal approximators. One could always build an MLP that accurately mimics an RBF network's behaviour, or vice versa. However, they may not be equally efficient in terms of number of parameters and required computational effort. There are some important differences that generally hold (based on [27]):

1. An RBF network usually has a single hidden layer, whereas an MLP may have one or more hidden layers. (It should be noted, however, that theoretically, one hidden layer in an MLP should be sufficient.)
2. The output layer of an RBF network is usually linear, whereas the output layer of an MLP may or may not be linear.
3. The argument of the activation function of each hidden unit in an RBF network computes the distance (Euclidean norm) between the input vector and the centre of that unit. The activation function of each hidden unit in an MLP computes the inner product of the input vector and the weight vector of that unit.
4. MLP's construct global approximations to non-linear input-output mapping. This implies that generalisation in regions of the input space where little data is available (interpolation and extrapolation) is possible, although extrapolation may have generate unpredictable results. On the other hand, RBF networks construct local approximations to nonlinear input-output mappings. Extrapolation will eventually result in the bias value of the output layer. This results in fast learning networks, but in order to span a large input space, usually a vast number of radial-basis functions (hidden units) are needed.

Of course, there are exceptions to the rules, they only have indicative meaning.

4.3.4. Modelling Transient Behaviour by Neural Networks

For the sake of completeness, a few words will be added on modelling dynamics by neural networks, although this has not been applied to this research. From the variety of networks that has been developed to model dynamics, two examples are briefly discussed below.

Networks with lumped dynamics

A disadvantage of the ordinary feedforward networks is that they cannot use information from previous time steps. A relatively simple solution to this drawback for nonlinear prediction on a stationary time series (that is, its statistics do not change in time) is to use so called tapped delay inputs. Instead of using the inputs at sample time k, the inputs at the sample times $k\text{-}1$, $k\text{-}2$,...$k\text{-}n$ are used to feed an otherwise static neural network, where n, the so called prediction order, is the number of delays used. The dynamics of the system to be modelled are 'lumped' in an external delay system. Because there is no feedback, it is still a feedforward network that may be trained as an ordinary feedforward network.

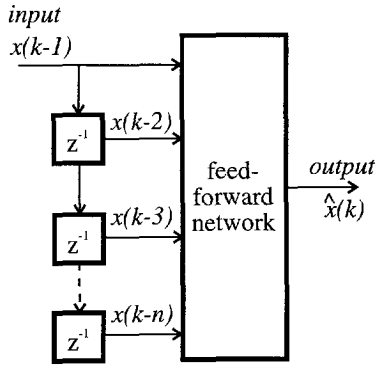

Figure 4.7: *Feedforward Neural Network as a non-linear predictor of a time series Networks with distributed dynamics*

Recurrent networks have feedback loops over individual nodes, over layers or over the entire network (Fig. 4.8). In this figure, a network with one hidden layer has been drawn, while a few (but not all) of the possible feedback loops have been drawn as well. This means that calculated outputs of a node, layer or network can also become inputs to the node, layer or network respectively. Thus, temporal behaviour can be modelled using such networks.

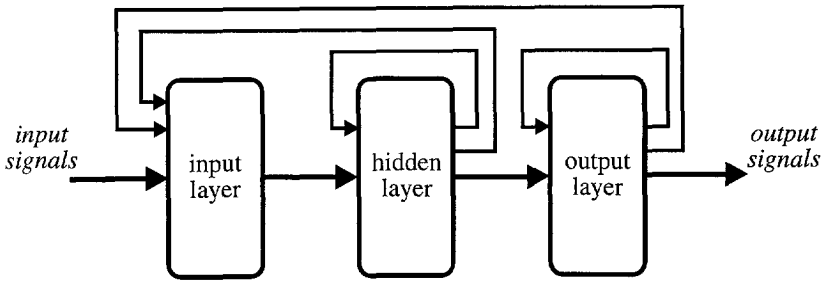

Figure 4.8: *Example of a Recurrent Neural Network*

The introduction of feedback loops in the network implies that care has to be taken to avoid stability problems that, given the nonlinearity of the system, may be hard to predict. The interested reader is referred to [27] for further explanation.

4.3.5. How to treat data with neural networks

Function approximation, being a form of data analysis, requires certain measures with respect to data handling to prevent the assessment of misleading results.

Training, validation and test sets of data

A set of examples, consisting of paired values of inputs and outputs, forms the so-called *training set*. After the function has been learned, or in other words, the network weights have been optimised, the proper behaviour of the network is verified using a second set of examples, the *test set*. Using this test set, that has not been used in training, the generalisation properties of the trained network can be investigated and an unbiased estimate of the generalisation error can be made. If the second set has been used in the training, for example for a stop criterion for the optimisation of the network parameters or to choose the best network from a set of networks, we cannot also use this set as a test set to estimate the generalisation error since this would produce a flattering, biased result. Therefore, a third, completely independent data set, now called *test set*, needs to be used for unbiased estimation of the performance of the network in those cases that the second data set, now called *validation set*, has already been used in training the network. Clearly, all three data sets need to be representative for the problem at hand. Since the concepts of training, validation and test sets are being used rather inconsistently in neural network literature, they are defined here as:

Training set:	A set of examples used for learning, that is to set the weights of the network
Validation set:	A set of examples used to tune the parameters of the network, for example to choose the number of hidden nodes
Test set:	A set of examples used only to assess the performance of a fully trained network.

It can be argued that using the method of holding out data for the actual training is wasting information that could have been used for the optimisation network weights. Indeed, this method assumes that plenty of data is available. If this is not the case, some other methods such as cross-validation and bootstrapping may be preferable. However, since the availability of data is not a problem in this research, these methods are not discussed here and the interested reader is referred to [56] for more details on these issues. It is noted that the issues of validation and testing are not specific to neural networks but should be considered with any data analysis method.

Standardisation of data

Although in theory scaling or standardisation is not necessary if linear output nodes are used, it is good practice to scale the input and output signals such that they all lie within a reasonable range around zero. This is merely to improve the numerical conditions for the optimisation process. A commonly used method is to subtract the mean and divide by the standard deviation of the data. Obviously, if bounded activation functions such as the sigmoid function are used in the output nodes, the

output signals need to be scaled such that they fit in the output range of the activation functions of the output nodes. It is noted that standardising outputs affects the objective function of the optimisation and will thus affect the training result.

Nonlinear transformation of data

Nonlinear transformation of output data primarily affects the objective function in the optimisation of the weights of the network. Since most optimisation methods are based on minimising the absolute difference between target outputs and network outputs, nonlinear transformation may emphasise certain regions of data, while other regions become underexposed. For example, squaring the target values puts more emphasis on large values than on small values.

Since at low friction utilisation the problem of estimating μ becomes ill-posed, in the sense that there is no unique output for μ for various inputs of side force, aligning torque and load, while at high friction utilisation the problem of estimating α becomes ill-posed, problems in the neural network mapping may be expected. For convergence of optimisation, it is desirable to put little emphasis on ill-conditioned data, although it is desirable to have at least a rough estimate of α and μ even if the problem becomes ill-conditioned. This is a designer's trade off. Sometimes it is also useful to split the domain of the mapping into several sub-domains for which it is easier to construct mapping networks.

4.3.6. Optimisation of Neural Networks by Genetic Algorithms

A Genetic Algorithm [9, 24] can be described as an optimisation program that starts with a population of encoded members. It uses a selection process to select the members with highest fitness for procreation using reproduction and recombination to combine properties of the successful members and mutates them stochastically.

Genetic Algorithms (GA's) have been applied to neural network problems essentially in two ways:

1. Training of the network. Instead of using the conventional training algorithms, that are usually based on some form of gradient descent, a GA may be used to select the appropriate weights for a network of a given architecture.
2. Optimisation of the network architecture. The network architecture is selected by a GA, which is then trained by conventional training algorithms, such as backpropagation or Levenberg-Marquardt algorithms.

Obviously, combinations of these two options are also being employed.

Training of Neural Networks by Genetic Algorithms

Training of neural networks by GA's can be useful in special cases, for example if the activation functions are not differentiable, or if there is a need to find the global optimum, rather than a local optimum that is typically found by gradient based

optimisation methods. GA's have been proven to be suitable for such tasks. However, in most cases, including this research, the GA's are far less efficient than conventional algorithms to train neural networks. We will therefore disregard training of neural networks by GA's and assume that the training of the network is performed by conventional training algorithms such as back-propagation or Levenberg Marquardt optimisation.

Optimisation of the Architecture of Neural Networks by Genetic Algorithms

The problem of choosing the optimal network architecture for a specific problem has not yet been solved, as remarked earlier. We may address it as an optimisation problem involving discrete variables, rather than solve this problem by using experience and rules of thumb. One excessively time consuming way to solve this problem is by simply calculating all possibilities. This is only practicable for small problems. For larger problems, one may try a random search, or more sophisticated heuristic methods, such as Genetic Algorithms. The GA optimisation process is visualised by a flow diagram in Figure 4.9. The optimisation scheme consists of two nested optimisation loops: the inner loop to optimise (train) the network weights for a given network architecture, and the outer loop to optimise the network architecture.

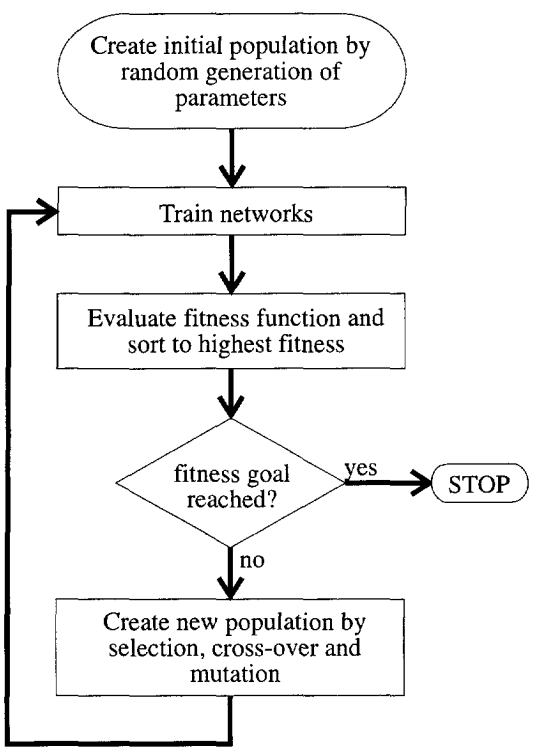

Figure 4.9: *Flow diagram of GA optimisation*

Encoding of Neural Networks for use with Genetic Algorithms

The GA approach requires that the architecture has to be coded in such a way, that from one or more different networks new and hopefully better networks can be derived. The encoding has to contain all possible network configurations within the constraints imposed by the user, while excluding all non-valid configurations. Table 4.2 gives an example of a binary encoding of a network configuration by a bitstring with a total length of 15 bits. This bitstring represents the architecture of a feedforward neural network with a maximum of two hidden layers, while the nodes in the layers contain a choice of one out of four activation functions per layer. In GA terminology, the bitstring is called a chromosome, while the bits are called genes. Since this optimisation problem involves discrete variables, binary encoding is sufficient. However, if real-valued variables are to be optimised, binary encoding typically involves a trade off between precision and complexity. In those cases, often real value representation is preferred. That, however, is beyond the scope of this section.

3 input signals available, 2 used	1 0 1			
1st hidden layer (< 8 nodes), 6 nodes		1 1 0		
2nd hidden layer (< 8 nodes), 4 nodes			1 0 0	
4 activation function types per layer				11 10 01
Total bitstring (15 bits)	1 0 1	1 1 0	1 0 0	11 10 01

Table 4.2: *Example of encoding of a neural network architecture for optimisation by using Genetic Algorithms*

Fitness Function

After the networks have been trained, the members of the population, in this case representations of network architectures, have to be compared with respect to their performance. This comparison requires a criterion, or so-called fitness function. The fitness function is usually a compromise between several conflicting demands. In this case the network mapping should be as accurate as possible, but on the other hand a small, fast learning network is also desirable. In this research the fitness function is (based on [7]) described by:

$$F = acc\left(1 + INI\left(1 - \frac{in}{in_{\max}}\right) + HNI_1\left(1 - \frac{hn_1}{hn_{1,\max}}\right) + HNI_2\left(1 - \frac{hn_2}{hn_{2,\max}}\right)\right) \qquad (4.14)$$

where F stands for fitness, acc for accuracy, INI for the Input Node Influence factor and $HNI_{1,2}$ for the Hidden Node Influence factors for the first and second hidden layer respectively, in for the number of input nodes and hn stands for the number of hidden nodes. The subscript 'max' indicates the maximum allowed value of the variable. Since the accuracy is usually the most important aspect, the node influence factors are usually chosen to be small (<<1).

Procreation by Genetic Algorithms

By employing the principle of survival of the fittest (Darwinism) only the best members of a so-called population are kept and used for procreation. This selection process may be based on a simple ranking of the members with respect to their fitness, or on a biased roulette wheel mechanism, where the chance that a member is selected is positively biased by the fitness of that member. Often, a few of the fittest members of a population are reproduced to the next generation without changes. The other members are used for mating.

The most popular mechanism for mating is cross-over. This means that part of the bitstring of a member is swapped with the corresponding part of the mating partner. Figure 4.10 shows an example of cross-over of the last four bits at the tails of the bitstrings of two members. The cross-over may take place at any point in the string, and also at more than one point (multiple cross-over). Furthermore, swapping of parts of the bitstring is possible between more than two members at a time. Many variations of the cross-over operator have been proposed.

old generation		
member A	1 0 1 1 1 0 1 0 0 1 1	1 0 0 1
member B	1 0 0 1 0 1 1 0 0 0 1	0 1 1 1
new generation		
member A*	1 0 1 1 1 0 1 0 0 1 1	0 1 1 1
member B*	1 0 0 1 0 1 1 0 0 0 1	1 0 0 1

Figure 4.10: *Cross-over of two members of a population*

The introduction of 'fresh blood' may be obtained by adding new, randomly generated members to a new generation, or by mutation of members. The latter means that every bit of the bitstring has a small chance to be changed from 1 to 0 or vice versa. The goal of these measures is to prevent that the optimisation algorithm becomes trapped into some local optimum.

When the new population has been created, the new networks are trained and their fitnesses are evaluated. This cycle continues until the fitness goal has been reached.

Some remarks on the use of Genetic Algorithms with Neural Networks

It should be considered that even this method is not a truly objective way to determine the optimal network architecture; the solution is biased by the choice of encoding and the criterion at which the optimisation is stopped. If the number of generations is limited, as is usually the case, the start population and the rules for procreation may also affect the result. It should also be considered that the optimisation process is very computationally expensive. To evaluate the objective function, each network in the population of each generation has to be trained, and

preferably even more than once, to minimise the effects of random choices for the initial values of the network weights in the training process. Especially for large networks, this easily becomes a large computational burden.

4.4. Conclusions of this chapter

Two methods to find the required mapping from tyre forces and torques to side slip angle and friction coefficient have been discussed in this chapter:

The use of a *lookup table* is very fast and straightforward. However, to have a sufficiently small table, a transformation of data to a set of predefined conditions needs to be performed by using the similarity method. The assumptions made in this process mildly violate the actual tyre behaviour. Moreover, filling the table may be quite a cumbersome task and this method is not very robust to disturbances.

The *neural network* approach may be regarded as a generalisation of the table lookup method. It is far more flexible and besides more robust to disturbances than the table lookup method. The use of neural networks involves two basic steps:

1. A choice of *network architecture*, involving choices such as the type of network, the number of layers, the number of nodes per layer and the type of activation functions. No well proven rules exist for the design of the neural network architecture. Usually, the design is based on experience and rules of thumb. A more objective design method is provided by applying Genetic Algorithms. By using an evolutionary mechanism, the best network architecture evolves from a number of generations of network architecture populations. However, the application of GA's for the optimisation of neural network architectures usually involves an excessive amount of calculation time.
2. The optimisation of the *network parameters*. The training of the network is performed on data available from models or measurements. This data set is called the training set. For this training a number of standard algorithms are available. The training of the network is easy, but time consuming. Once the network has been trained, its proper behaviour needs to be verified using an independent data set, the so-called test set. Both the training and the test set need to be representative for the problem in question. Once the network has been trained, the network calculations are fast and straightforward.

Because of their flexibility and robustness, the neural networks have been chosen as the preferred method in this research.

5

Experimental Applications

5.1. Introduction

The previous two chapters have provided the method and the tools to identify the side slip angle and the tyre to road friction coefficient of a running vehicle. This chapter describes the validation and application of the identification procedure, both in simulation and on actual vehicles. First, the validity of the identification method is verified using a tyre test trailer. Then, implementation in a standard passenger car is discussed to verify the possibility of application in a standard vehicle. Experiments with both vehicles have been conducted, both at simulation level and outdoors. Finally, some disturbances are discussed that could not be tested by experiments, but that may have to be accounted for in future applications.

5.2. Simulation models

In addition to the actual implementations in vehicles, simulation models have also been used. Their virtues are that they are always available, that manoeuvres can be simulated that are hard to realize in practice and on surfaces that are not actually available, that an unlimited number of signals is available and that their results can be used to compare with the results obtained with the actual vehicles and vice versa.

In this research, two vehicle simulation models have been used. One is a relatively simple nonlinear model built in Matlab/Simulink, the other one is built using a multi-body simulation software package called BAMMS [63]. While the latter is more accurate than the first, it is also much slower in computation. For many purposes, the simpler model is sufficient. The parameters have been taken from the manufacturer's specifications, supplemented with parameters that have been

obtained by mass and inertia measurements taken from the actual vehicle in the laboratory.

5.2.1. The Matlab/Simulink simulation model

The Matlab/Simulink model is based on the well known two-track model of a vehicle, depicted schematically by Figure 5.1. The vehicle model consists of the sprung vehicle body mass m_b and the lumped unsprung mass m_a of the front and rear axles. The total mass m is the sum the unsprung and sprung masses:

$$m = m_a + m_b \tag{5.1}$$

The sprung mass has a rotational degree of freedom with respect to the unsprung mass defined by the roll axis. For simplicity, the roll axis has been considered as being fixed in location with respect to the unsprung mass, which is a good approximation when the roll angle remains small. The origin of the system of axes of the vehicle has been located at the roll axis, right beneath the centre of gravity of the sprung mass and fixed to the unsprung mass. The orientation of the axis system follows the SAE conventions, that is x points forward, y to the right and z points down. Furthermore, the roll of the unsprung mass and the pitch of the vehicle body have not been considered, since these are of less importance to this research. With these limitations, we have three mechanical degrees of freedom (DOF) left:

1. the lateral velocity (V_y) of the vehicle at the origin of axes
2. the yaw rate (r) of the vehicle
3. the roll angle (φ) of the vehicle body about the roll axis

Figure 5.1 shows the vehicle model with a wheel base of length $a+b$, and for simplicity centres of gravity of both unsprung and sprung masses at a distance a from the front axle. The trackwidth equals d and at each wheel, the planar tyre forces are indicated by X and Y in longitudinal and lateral direction respectively and the self aligning torque by M_z. In this general case, each wheel may have a different steering angle δ.

The model describes the linearized vehicle behaviour in a steady state turn by the following set of equations for the lateral, yaw and roll motion:

$$\begin{aligned} &m(\dot{V}_y + V_x r) + m_b h_c \ddot{\varphi} = \sum_i Y_i \\ &I\dot{r} = a(Y_1 + Y_2) - b(Y_3 + Y_4) + \frac{d}{2}(X_1 + X_3) - \frac{d}{2}(X_2 + X_4) + \sum_i M_{z,i} \\ &I_{xx}\ddot{\varphi} + K\dot{\varphi} + (C - m_b g h_c)\varphi = m_b h_c(\dot{V}_y + V_x r) \end{aligned} \tag{5.2}$$

where V_x is the longitudinal velocity of the origin of vehicle axes, h_c is the height of the centre of gravity of the vehicle body above the roll axis, I_{xx} is the moment of

inertia of the vehicle body about the roll axis (in x-direction), C the roll stiffness and K the roll damping coefficient. For simplicity, the dynamic effects of product of inertia I_{xz} of the vehicle body and of a possibly inclined roll axis have been neglected in this analysis. The roll stiffness and damping are a result of the front and rear wheel suspensions.

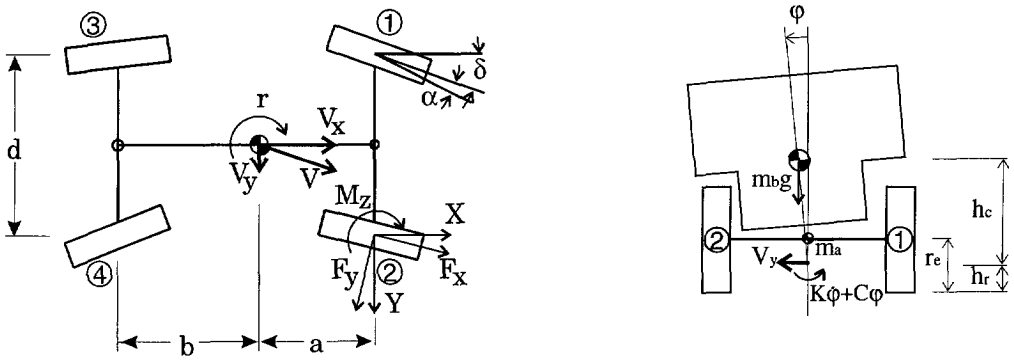

Figure 5.1: *Three DOF two-track vehicle model in top view (left) and front view (right)*

Let us assume the steering angles, slip angles and yaw rate to be small and the total vehicle speed V to be constant. Also, we assume that there are no braking or driving forces:

$$F_{x_i} = 0 \qquad (i = 1..4) \tag{5.3}$$

with subscript *i=1..4* referring to the left front, right front, left rear and right rear wheel of the vehicle, respectively. These assumptions allow the following linearizations and simplifications:

$$\begin{aligned} V_x &\approx V \\ X_i &= F_{x_i}\cos\delta_i - F_{y_i}\sin\delta_i \approx F_{x_i} - F_{y_i}\delta_i \approx 0 \qquad (i = 1..4) \\ Y_i &= F_{x_i}\sin\delta_i + F_{y_i}\cos\delta_i \approx F_{y_i} \qquad (i = 1..4) \end{aligned} \tag{5.4}$$

For front wheel steering, as is the case with our test vehicle, $\delta_3 = \delta_4 = 0$ and approximately $\delta_1 = \delta_2 = \delta$. The tyre forces F_{y_i} and moments M_{z_i} are calculated using the nonlinear Delft Tyre Model (DTM) as a function of vertical load, side slip angle and camber angle, as described in [44].

$$\begin{aligned} F_{y_i} &= F_{y_i}(\alpha_i, \gamma_i, F_{z_i}) \\ M_{z_i} &= M_{z_i}(\alpha_i, \gamma_i, F_{z_i}) \end{aligned} \tag{5.5}$$

For the side slip angles α_i we have

$$\alpha_{1,2} \approx \frac{V_y + ar}{V} - \delta$$
$$\alpha_{3,4} \approx \frac{V_y - br}{V} - \delta \tag{5.6}$$

The side slip angle is filtered by a first-order filter to simulate the transient tyre behaviour due to the tyre relaxation length l_{rel}:

$$\frac{l_{rel}}{V}\dot{\alpha}_i' + \alpha_i' = \alpha_i \quad (i = 1..4) \tag{5.7}$$

Equation 5.7 is the equivalent in the time domain of Eq. 3.80 in the frequency domain. We calculate the camber angle γ_i of the tyre with respect to the flat, level road surface by

$$\gamma_i = \gamma_{b_i} + \varphi \tag{5.8}$$

where γ_b is the camber angle with respect to the vehicle body and φ is the roll angle of the vehicle body. For the front wheels, the angle $\gamma_{b,i}$ depends on the kinematics of the suspension and is a function of φ and δ. For the rear wheels, obviously the steering angle δ does not play a role.

$$\gamma_{b_i} = \gamma_{b_i}(\varphi, \delta) \quad (i = 1,2)$$
$$\gamma_{b_i} = \gamma_{b_i}(\varphi) \quad (i = 3,4) \tag{5.9}$$

Finally, the load is calculated by summing the static load and the load transfer from inner to outer wheels in a turn. For the static load at the front and the rear wheels we have

$$F_{zs_f} = \frac{b}{a+b} mg$$
$$F_{zs_r} = \frac{a}{a+b} mg \tag{5.10}$$

Usually, the roll axis is slightly inclined such that $h_{r,f}$ is smaller than $h_{r,r}$. Also, we use the different unsprung masses $m_{a,f}$ and $m_{a,r}$ at the front and rear axle respectively rather than the lumped unsprung mass m_a and we use the different roll stiffnesses and damping coefficients at the front and rear axle, denoted with the subscripts f and r respectively. The load transfers at the front wheels and rear wheels are obtained by summing the moments about the roll axis. Figure 5.2 shows the relevant forces and torques at the front axis, the rear axis is similar.

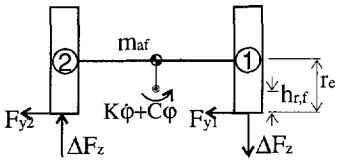

Figure 5.2: *Load transfer at the front axle*

The load transfers at the front and rear axles are calculated by

$$\Delta F_{z,f} = \frac{1}{d}\left\{K_f\dot{\varphi} + C_f\varphi + \left(\dot{V}_y + Vr + a\dot{r}\right)m_{a,f}\left(h_{r,f} - r_{e,f}\right) - F_{y,f}\,h_{r,f}\right\}$$
$$\Delta F_{z,r} = \frac{1}{d}\left\{K_r\dot{\varphi} + C_r\varphi + \left(\dot{V}_y + Vr - b\dot{r}\right)m_{a,r}\left(h_{r,r} - r_{e,r}\right) - F_{y,r}h_{r,r}\right\} \qquad (5.11)$$

where $F_{y,f}$ and $F_{y,r}$ are the summed tyre side forces at the front and rear axle respectively.

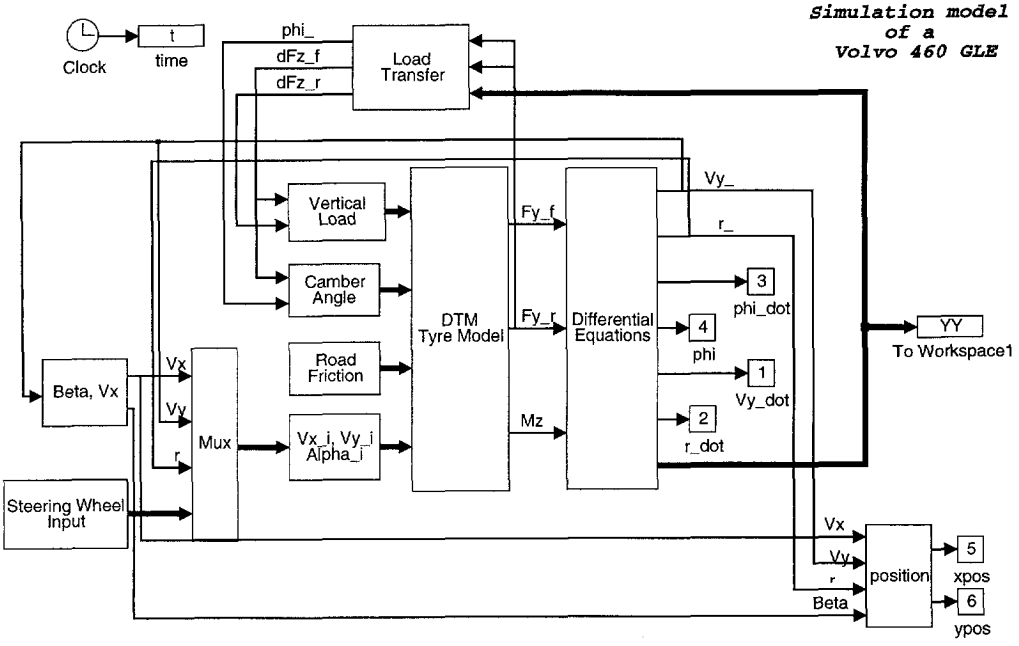

Figure 5.3: *Matlab/Simulink Vehicle Model*

The model has been built using Matlab/Simulink, which provides a modular way of model building. Figure 5.3 shows the block diagram representation of the model. The blocks have descriptive names indicating their functions. Most of the blocks,

e.g. the block called 'Differential Equations', are in turn built up from blocks, put together in one block.

Since linearization has been used in the vehicle modelling, the model is only valid for small deviations around a steady-state turn.

5.2.2. The BAMMS simulation model

Another model, which is not limited to small angles, has been built using a multi-body software package called BAMMS, which stands for Bond graph based Algorithm for Modelling Multi-body Systems [63]. The greater part of this model had already been built by Venhovens [64] but it was modified and extended for this research.

Multi-body software packages prove to be powerful tools in vehicle modelling. The generation of complex non-linear models simply involves defining stiff bodies and interconnecting them by springs and dampers (possibly with non-linear characteristics) or by defining constraints between the bodies. Using BAMMS, a 17 DOF (6 for the vehicle body, 2 for the independent front axles, 2 for the rigid rear axle, 3 for the power train and 4 for the wheel rotations) nonlinear model of the vehicle, including nonlinear tyre behaviour with combined side and longitudinal slip described by the DTM, nonlinear suspension characteristics and steer compliance was built.

As will be shown later, the model behaviour shows good correspondence with the actual vehicle behaviour. Furthermore, the model can be used to simulate measurements with sensors positioned at the same locations as in the actual vehicle. A disadvantage of the model however, is that it takes great computational power to do simulations within reasonable time. For less critical tasks, the simple Matlab/Simulink model is often sufficiently accurate and requires far less simulation time, even though this model has not been optimised for speed and uses a code interpreter, as opposed to the compiled BAMMS-model.

5.3. Experiments with the tyre test trailer

Experiments to verify the identification algorithm have been performed using the tyre test trailer of the Vehicle Research Laboratory at the Delft University of Technology. Figure 5.4 shows the trailer with the test wheel mounted on a measuring hub, located between front and rear wheels. For this research the trailer was only used in pure side slip experiments. A mechanical device in the trailer varies the slip angle and the vertical load of the test wheel as a predetermined function of time. Camber can be set to a fixed angle and water can be sprayed in front of the tyre to wet the road surface. The measured signals F_y, M_z and F_z are

logged and fed to the identification algorithm. A small trailing wheel connected to a potentiometer is used to measure the side slip angle for reference. No device to measure the tyre to road friction coefficient directly is available. The reference value for the friction coefficient is therefore determined by measuring the maximum tyre forces and determining the friction coefficient by fitting these measurements using the DTM. This implies that only an average value of the tyre to road friction coefficient is known for a specific type of road surface in the conditions (e.g. dry or wet, outside temperature) of the time of measurement, while the actual friction coefficient may vary a little, due to spots of dirt or inhomogenities of the road surface for example.

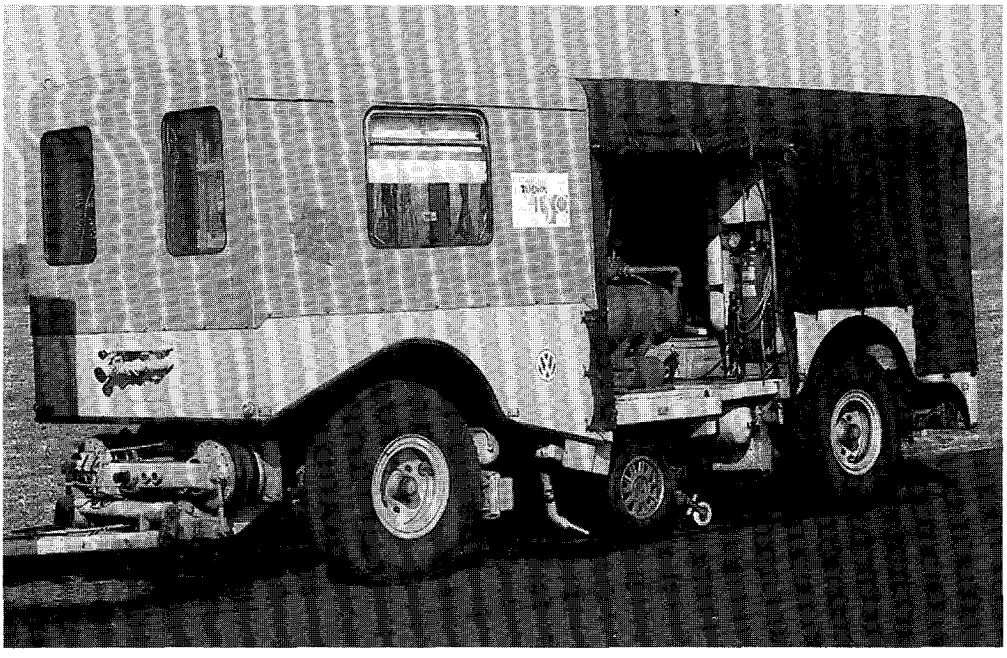

Figure 5.4: *The Tyre Test Trailer of the Vehicle Research Laboratory of the Delft University of Technology*

Various experiments were conducted with the tyre test trailer. Firstly, quasi-static side slip angle sweeps on different surfaces were conducted, to verify the identification procedure. Secondly, manoeuvres were carried out that were calculated by the Matlab/Simulink simulation model of a passenger car. These manoeuvres were 'played back' on the tyre test trailer with a test tyre running on the road. Finally, random manoeuvres were performed.

5.3.1. Quasi-static side slip angle sweeps

A data set was generated by quasi-static variation of the slip angle α at 2, 4, 6 kN

vertical load on both high and low-friction tracks. The data set was split into a training set with data at 2 and 6 kN vertical load and a test set at 4 kN vertical load. A neural network was trained, that is the network parameters were optimized, by presenting the measured signals F_y, M_z and F_z as inputs and α and μ as outputs of the network. The results of the training are displayed in the left part of Figure 5.5. In this figure, the solid lines represent the actual values, while the dashed lines represent the network outputs. The actual friction value μ was calculated from the estimated μ_u using Eq. 3.20. The proper behaviour of the network was then tested by presenting the measured signals F_y, M_z and F_z of the test set as inputs to the trained network and comparing the outputs of the network to the measured signals α and μ of the test set. These results are displayed in the right part of Figure 5.5.

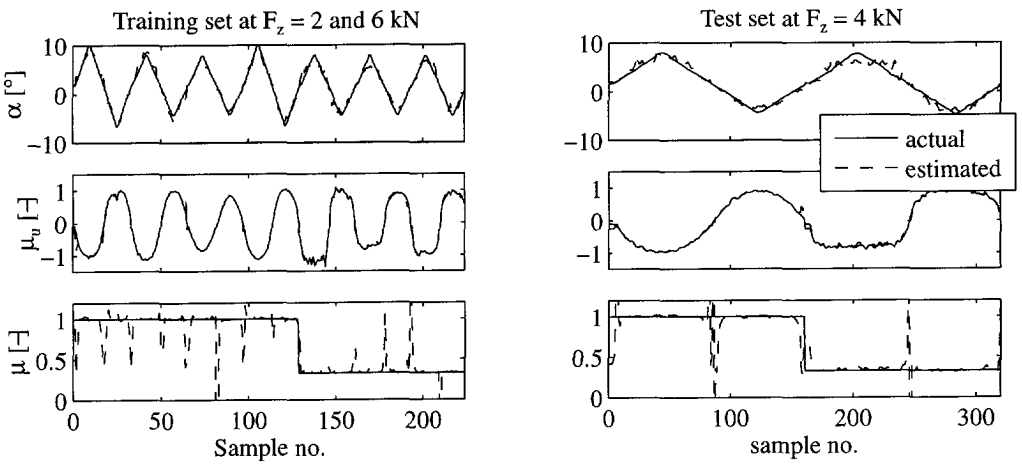

Figure 5.5: *Estimation results from quasi-static tyre test trailer data*

First of all, these results show that neural networks are able to perform the required mapping from measurements to slip angle and friction estimates. Furthermore, the slip angle estimate appears to degrade at high slip angles and/or low friction values (corresponding to total sliding), while the actual friction estimate appears to degrade at small slip angles and/or high friction values (corresponding to almost complete adhesion). These results comply with the brush tyre model theory as explained in Chapter 3. Finally, the utilised friction μ_u is estimated more accurately than the actual friction μ. This can be understood from Eq. 3.20 and recalling that the friction estimate is poor when $|\mu_u|$ is low. In that case, the side force will also approach zero. Thus, even though the friction estimate is poor, the estimate of μ_u is not heavily disturbed.

5.3.2. Play-back of simulation of a lane change manoeuvre

The next figure shows the results of single lane change manoeuvres on high and low friction road surfaces using the same neural network parameters as in the preceeding section. The testwheel of the tyre test trailer was steered and loaded according to the results of simulations with the Matlab/Simulink vehicle model for the right front wheel. The forward speed of the simulated vehicle and, accordingly, also of the tyre test trailer was 10 m/s. The lateral deviation of the vehicle was about 4 meters for both experiments. Obviously, the lane change on the higher friction road surface can be conducted much quicker than at the lower friction road surface. It was intended that in both cases the full friction potential should be used. Since at the time of the experiments the camber angle of the tyre test trailer could not be changed dynamically, it was set to zero.

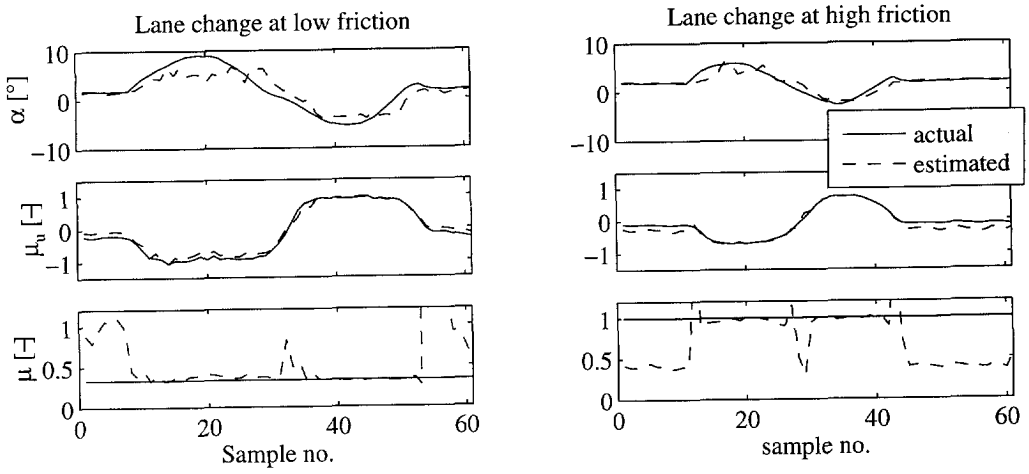

Figure 5.6: *Estimation results from tyre test trailer on lane change manoeuvres at high friction (left) and low friction (right) road surfaces*

These results show that the algorithm is capable of detecting the road friction shortly after the start of the lane change manoeuvre. It may be surprising that the friction estimate seems more smooth at the high friction track than on the low friction track. The reason for this may be found in the lower signal levels of the measurements at the low friction track, thus worsening the signal to noise ratio. If the test wheel is running straight, the friction estimate becomes more or less random while the side slip angle is estimated accurately, as we would expect. The same holds true at the zero crossing of the side slip angle during the lane change. Again, the utilised friction is estimated quite accurately.

Even though these experiments involve a higher rate of change of side slip angle, inducing some tyre transient behaviour, the neural network, trained on quasi-static data, still performes adequately.

5.3.3. Random manoeuvres

Finally, random steering inputs were given to the Matlab/Simulink model and their results were used to steer the test wheel of the tyre test trailer. Due to the dynamics of the simulation model and, moreover, the limited bandwidth of the actuators of the trailer, the resulting steering input (both slip angle and load) was a random signal of low bandwidth. Nevertheless, it gives an indication of how the identification algorithm behaves at random side slip angle variations around zero.

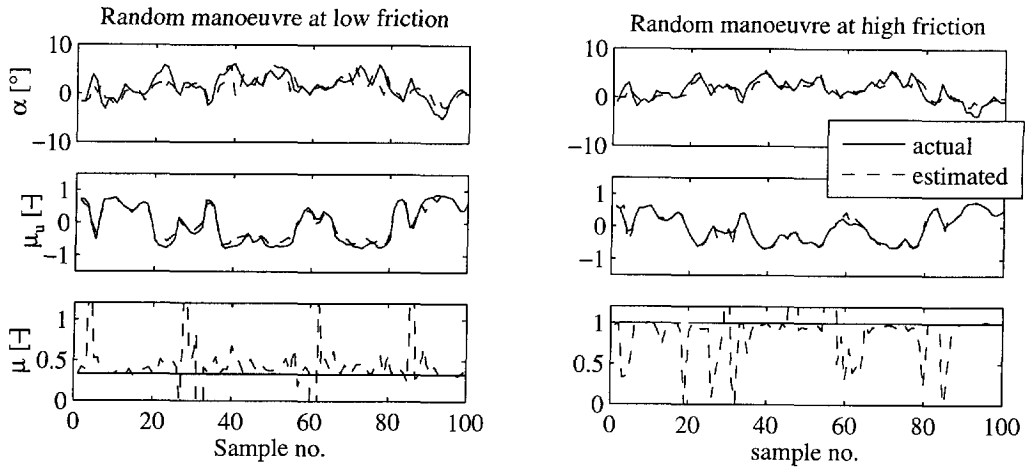

Figure 5.7: *Estimation results from tyre test trailer on random manoeuvres*

The results displayed in this figure confirm the previous findings. Again the identification of the friction coefficient is best at higher levels of friction utilization. The transient behaviour becomes more apparent in these random manoeuvres and disturbs the identification. However, using some adequate filtering one might still distill the average friction coefficient.

5.4. Experiments with the passenger car

5.4.1. Set up of a measurement system in the car

So far we have assumed that the signals F_x, F_y, F_z and M_z of the tyre are all available. However, these signals cannot be measured directly in a standard vehicle unless an expensive rotating wheel dynamometer is used. Since using such a wheel

dynamometer would not give insight into the applicability of the identification method in a standard vehicle, an alternative method has been employed using a set of relatively inexpensive sensors in the front wheel suspension. At this point, only the right front wheel suspension was instrumented. It would be advisable though, to instrument both front wheels. The vehicle under consideration in this research is a Volvo 460 (Fig. 5.8).

Figure 5.8: *The test vehicle (before modifications were made)*

It is a mid size front-wheel drive car with an independent McPherson type front wheel suspension, depicted by Figure 5.9, and a light-weight five link rigid rear axle.

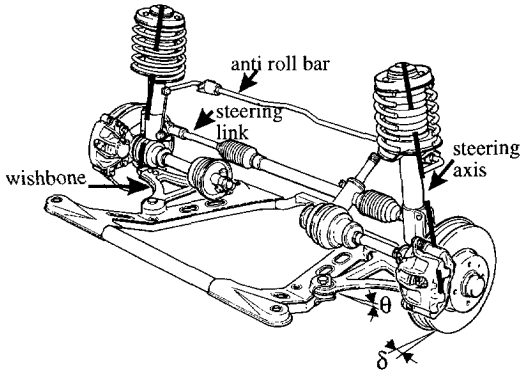

Figure 5.9: *Front wheel suspension*

In this research, we only need to study the front wheels suspension in more detail. The identification procedure described in the previous chapters requires the determination of the tyre forces F_x, F_y and F_z, the self aligning torque M_z and the wheel camber angle γ. Before deciding how these quantities will be measured, we will study the geometry and static force analysis.

The wheel with the tyre is mounted on the wheel carrier, where it can rotate about the spindle. The wheel carrier is rigidly attached to the spring-damper strut, which is attached to the vehicle body by a rubber bushing. For this analysis, we regard this bushing as a universal joint. The strut itself provides for a translational and a revolute degree of freedom. Furthermore, the wheel carrier is attached to the lower suspension arm (wishbone) by the lower ball joint (king-pin). The wishbone is attached to the subframe again by rubber bushings, allowing a rotational degree of freedom, such that the wishbone can sway up and down to allow vertical wheel motion. The wheel assembly can rotate about a line through the upper strut mount and the lower ball joint, the steering axis, indicated by a thick, dashed line in Fig. 5.9. Usually this line does not align with the strut. This rotational, steering degree of freedom is constrained by the steering link, connected to the wheel carrier by another ball joint at the steering knuckle. This link in turn is connected to the steering wheel via the steering rack and pinion.

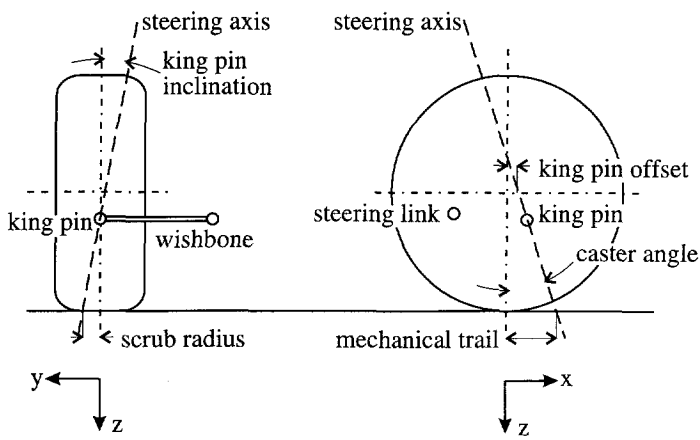

Figure 5.10: *Suspension geometry*

The steering axis is not vertical, but tilted in two directions, described by the king-pin inclination in the y-z plane and the caster angle in the x-z plane (Fig. 5.10). The steering axis intersects with the ground plane at a distance from the wheel center called the mechanical trail in x-direction and the scrub radius in y-direction. The orientation of the steering axis, and consequently the effective mechanical trail and

scrub radius, changes with rotation of the wheel assembly about the steering axis and with the sway angle of the wishbone. The same holds true for the camber angle γ_6 of the wheel with respect to the vehicle body.

The tyre forces in lateral direction are primarily counteracted by reaction forces in the ball joint and in the upper strut mount (Fig. 5.11). From the balance of moments it easily follows that the reaction forces in the ball joint are much larger than the reaction forces in the upper strut mount. The forces in the steering link caused by lateral forces are usually small, but owing to the pneumatic and mechanical trail not negligable. The pneumatic trail and the tyre lateral force form the self aligning torque.

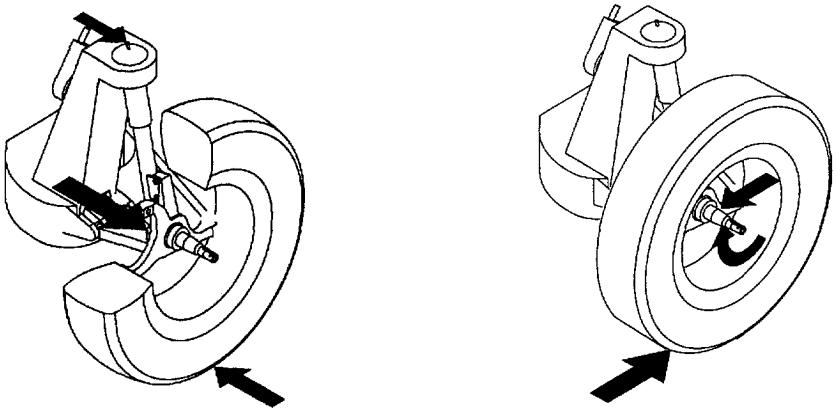

Figure 5.11: *Reaction forces due to lateral forces (left) and longitudinal forces (right) [26]*

In the longitudinal direction, the tyre forces cause a torque about the spindle, that may be counteracted by a driving torque via the driving axle or by a braking torque if the disc brake is activated. The latter case is more complicated due to the extra connection between rotating wheel and wheel carrier through the brake clamp and disc. This case will not be considered here. The longitudinal tyre forces are again counteracted primarily by reaction forces in the lower ball joint and in the strut mount, and also for a small part by forces in the steering link due to the scrub radius.

By convention, the scrub radius is defined in the road plane. However, the effective arm length needed to calculate the torque about the steering axis due to the longitudinal force should be calculated in a plane perpendicular to the steering axis. The same holds true for the mechanical trail.

The vertical tyre force is compensated primarily by the forces in the strut, and since the strut is not aligned vertically with respect to the wheel, for a small part by forces in the wishbone. Furthermore, the vertical tyre force also generates a relatively small torque about the steering axis, compensated by a force in the steering link. Their relative contributions vary with both the steering angle and the wishbone angle with respect to the vehicle body. Since the strut consists of a spring and damper, in static cases the length of the spring indicates the magnitude of the force reacted by the strut. A complication arises due to the anti-roll bar, which is meant to decrease the amount of roll that the vehicle shows in a curve. It consists of a torsion spring connected to the struts by small links. Thus, the anti-roll bar tries to equalize the suspension travel at the left and right front wheels. Because of the way the anti-roll bar is linked to the suspension strut, a torque in the anti-roll bar also generates a torque about the steering axis.

Since the king-pin is located almost at the centre of the wheel in this particular suspension design, the king-pin transmits the major part of the side force. It also transmits a considerable part of the longitudinal force. It is therefore convenient to measure the forces at the king-pin, by means of strain gauges. The strain gauges were mounted in two pairs, at opposite sides of the king-pin, forming two half Wheatstone bridges. Conveniently, the part of the joint with the strain gauges (the ball and shaft) is fixed to the wheel carrier, thus having a fixed orientation with respect to the wheel and the tyre. Figures 5.12 and 5.13 show the gauged king-pin before and after mounting in the wheel suspension respectively. The first picture also shows the mount with two bolt holes, through which the ball joint is bolted to the wishbone. (Note that for the picture in Fig. 5.13 to be taken, the cover plate protecting the brake disc was bent.) The rubber cover that normally seals the ball joint was removed to accomodate the wires connecting the strain gauges with the strain amplifier. Obviously, this rather fragile construction is only suitable for experiments; one would have to look for a more solid construction for everyday use. Alternatively, one could study other possibilities of measuring these forces, e.g. using a redesigned wishbone with strain gauges, or using small radial load cells in the joints connecting the wishbone to the subframe.

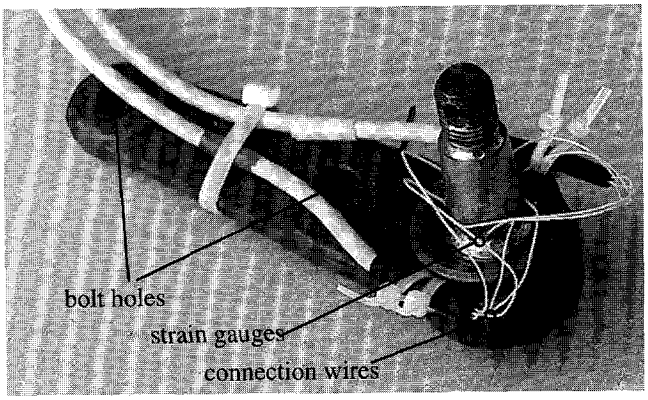

Figure 5.12: *Gauged lower ball joint before mounting*

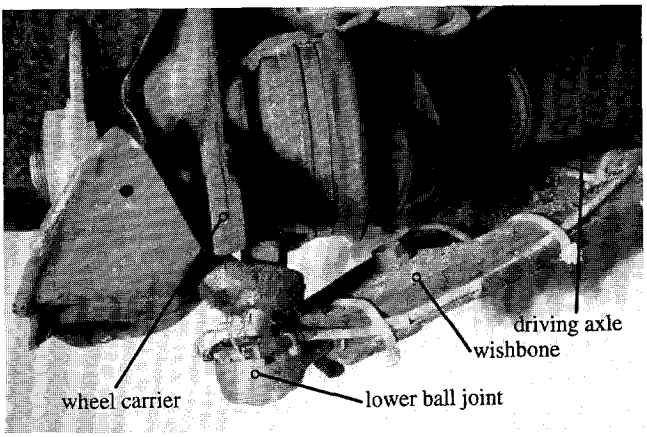

Figure 5.13: *Gauged lower ball joint mouted to wishbone and wheel carrier*

Since the vertical tyre forces are mostly counteracted by strut forces, the suspension travel is strongly correlated to the vertical tyre force. The suspension travel is actually determined by sensing the sway angle of the wishbone using a magneto-resistive potentiometer. To account for the effects of the anti-roll bar, the suspension travel (and travel speed if the dynamics are considered) at both front wheels are measured. The vertical tyre force may be determined in other ways too, e.g. by using accelerometers attached to the sprung and unsprung masses.

The moment about the steering axis M_a, reacted by the force in the steering link, is built up from contributions due to the tyre forces in three directions and the torque in the roll bar as well as the self aligning torque that needs to be determined. Also, all contributions to M_a depend on the steering angle δ and wishbone angle θ of the

suspension mechanism. To study the effects of these contributions, a simple kinematic model of the front wheel suspension was built in Matlab. This model assumes stiff links and joints, that all tyre force act at a point under the wheel center in the middle of the tyre/road contact patch, and that there is no pneumatic trail.

Let us assume that the static load of the tyre with the suspension in design position is 3 kN. The wishbone is forced to sway up and down over -20/+10 degrees, thereby relaxing and compressing the strut spring. We assume that the vertical tyre force completely reacts to the changing strut force, so that the vertical tyre force increases with positive wishbone angles. We also assume to have longitudinal and lateral tyre forces, equal in magnitude and with a resultant equal in magnitude to the vertical tyre force ($\mu_u=1$). Similarly, we force the wheel to steer over -45/+45 degrees. The direction of the planar tyre forces rotates with the wheel. The anti-roll bar is assumed to react as if the left suspension were locked, that is the left suspension does not move with the right suspension. Figure 5.14 shows the resulting torque about the steering axis due to the three tyre forces and the torque in the anti-roll bar as functions of the steering angle δ and the wishbone angle θ. These contributions appear to be in the same order of magnitude as the self aligning torque that we need to determine. It thus follows that the self aligning torque can be determined by measuring the force in the steering link, but only if all other contributions are accounted for. (Note that the maxima in Figure 5.14d are not commonly encountered: they represent situations of counter steering).

Obviously, a suspension design with minimal scrub radius and mechanical trail would be advantageous with respect to determination of the self aligning torque. Also, a rear wheel drive vehicle would eliminate the problem of driving forces affecting M_a. Finally, the contribution of the anti-roll bar to M_a could be eliminated by linking the anti-roll bar to the wishbone instead of to the strut.

The force in the steering link is measured by a standard load cell. One could attach strain gauges to the link to measure axial force, but in order to have a reasonable response, this would require necking down the link, which was considered unsafe. On the other hand, using the load cell required that the steering link was cut through. Alternatively, it might be possible to use the power steering pressure to determine the force in the link, but care would have to be taken that the forces in left and right steering links could be discriminated.

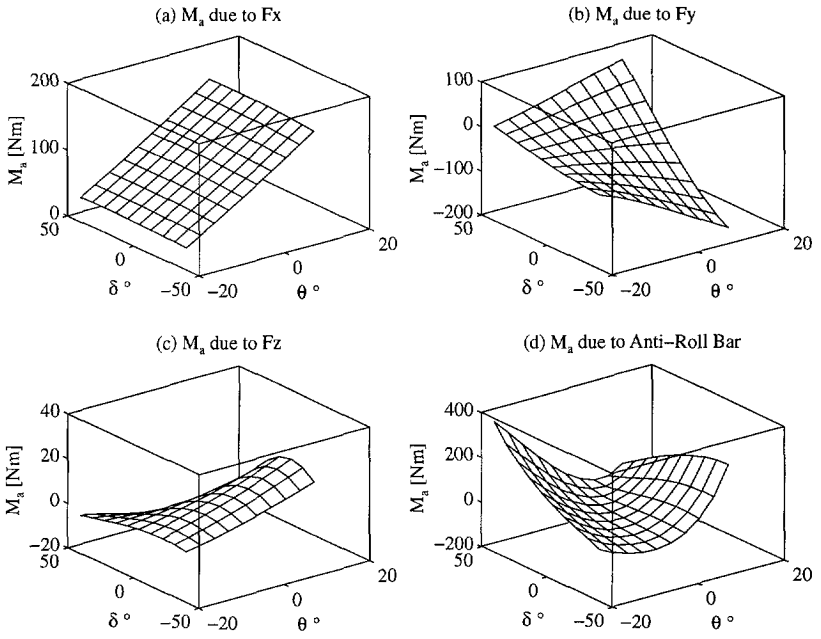

Figure 5.14: *Contributions to torque around the steering axis*

As previously explained it is necessary to determine the steering angle δ and the wishbone sway angle θ and also, to determine the wheel camber with respect to the vehicle body. The latter has already been done for the determination of the wheel load, while the steering angle is measured at the steering wheel. At the time of instrumentation, this seemed to be the most convenient solution. However, it has the disadvantage that steering compliance is present between the sensor and the actual wheel angle. Better solutions may be found by measuring the displacement of the steering rack or by measuring the rotation at the lower ball joint.

Summarizing, the following sensors were installed:

- A load cell in the steering link
- A magneto-resistive potentiometer to measure the angle θ of the wishbone relative to the car body
- Two pairs of strain gauges on the lower ball joint, forming two half Wheatstone-bridges.
- A potentiometer at the steering wheel

The measured signals are processed by a 486-PC on board the test vehicle.

For reference, a few other sensors were installed. These enabled us to compare the actually driven manoeuvres with simulated manoeuvres and check the

identification results. For these reasons, accelerometers for longitudinal and lateral directions and a gyro for yaw velocity were installed at the center of gravity of the vehicle. Also, a Leitz Corrovit optical instrument was installed close to the instrumented right wheel. This instrument is capable of measuring the longitudinal and lateral speeds with respect to the road surface. Thus, the side slip angle at the location of the instrument can be calculated and, from the vehicle geometry, also the side slip angle at the tyre. This signal can be compared with the estimated side slip angle and with the simulation results.

5.4.2. Modelling of the suspension kinematics by a neural network

Even though we have a number of models available that describe the suspension kinematics to various degrees of accuracy, for a number of reasons these models are not suitable for online implementation in a vehicle. Firstly, a model that accurately describes the suspension kinematics, including the flexibilities in the various joints and members, becomes far too computationally demanding. Secondly, the various parameters describing these flexibilities as well as the actual scrub radius are not readily available and hard to obtain. The scrub radius may vary considerably, especially with wide tires. Instead, we chose to describe the suspension kinematics by a nonlinear function, for which a neural network was employed. (It is noted that this is a rather subjective choice which does not rule out other possibilities.) In contrast with a conventional suspension model, the neural network learns the suspension kinematics from measured or simulated examples, without the need for exact parameters and geometries of the various parts. Moreover, it only needs to describe the suspension behaviour in the relevant working area, unlike a generally applicable model. Therefore, the resulting model after training of the network can be much simpler than the conventional model.

The BAMMS simulation model (see Section 5.2.2) is able to simulate both the sensor signals (the steering wheel angle, the wishbone sway angle, the forces on the king-pin in longitudinal and lateral directions, and the force in the steering link) and the actual tyre forces and torques (F_x, F_y, F_z, and M_z) for a given manoeuvre. A series of slalom manoeuvres on two road surfaces with different friction coefficient was conducted with the BAMMS model. These manoeuvres were also performed with the test vehicle, as will be shown in the next section. The acquired simulation data were used to train and test a 3-layer (one hidden layer) network that maps the sensor signals to the actual tyre forces and torques (Figure 5.15).

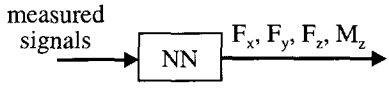

Figure 5.15: *Neural network describing the suspension behaviour*

The training set and the test set were constructed by dividing the data set into two parts. Figure 5.16 shows that identification by this network of F_x, F_y, F_z and M_z from the simulated sensor signals of the test set was successful. The figure thus shows that a neural network is indeed capable to describe the suspension kinematics sufficiently accurate.

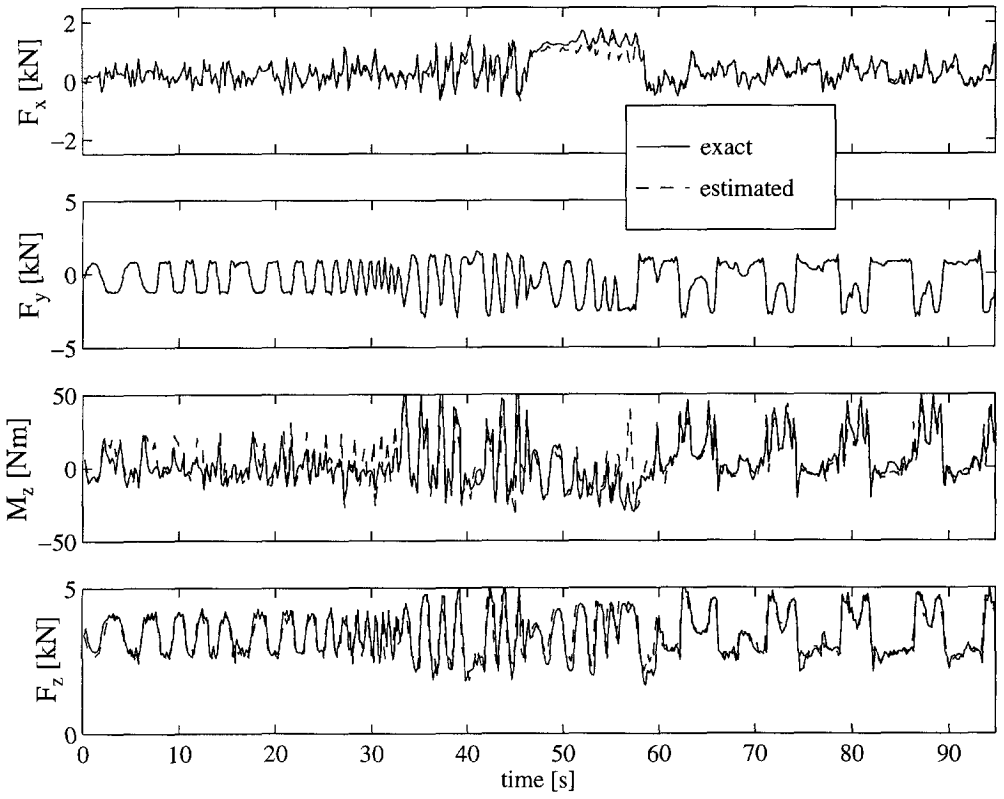

Figure 5.16: *Estimation of F_x, F_y, M_z and F_z from simulated sensor outputs.*

5.4.3. Estimation of side slip angle and tyre to road friction coefficient

The next step would have been to use the estimated tyre forces and self aligning torque to estimate the side slip angle and the tyre to road friction coefficient. However, that would have resulted in two neural networks in series (Fig. 5.17). Obviously, one could merge these networks, as indiciated by the dashed block in Fig. 5.17, and thus eliminate the intermediate step.

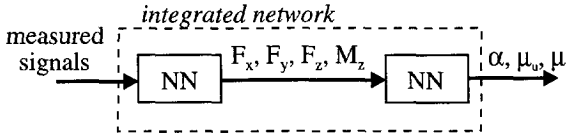

Figure 5.17: *Neural networks in series*

The estimates of α, μ_u and μ from the signals directly are displayed in Figure 5.18 for the training set. The network contains one hidden layer with 30 hidden nodes. This network architecture has been chosen to correspond with the network used with the test vehicle, as discussed in the next section. The network is obviously distinguishing the different friction levels, although the results are quite noisy. As we would expect, poor estimates of friction occur primarily at small values of μ_u, and poor estimates of side slip angle α occur at total sliding. Since the magnitude of μ_u is, on average, much lower at high friction levels than at low friction levels in this experiment, it is more difficult to correctly estimate the high friction level than the low friction level.

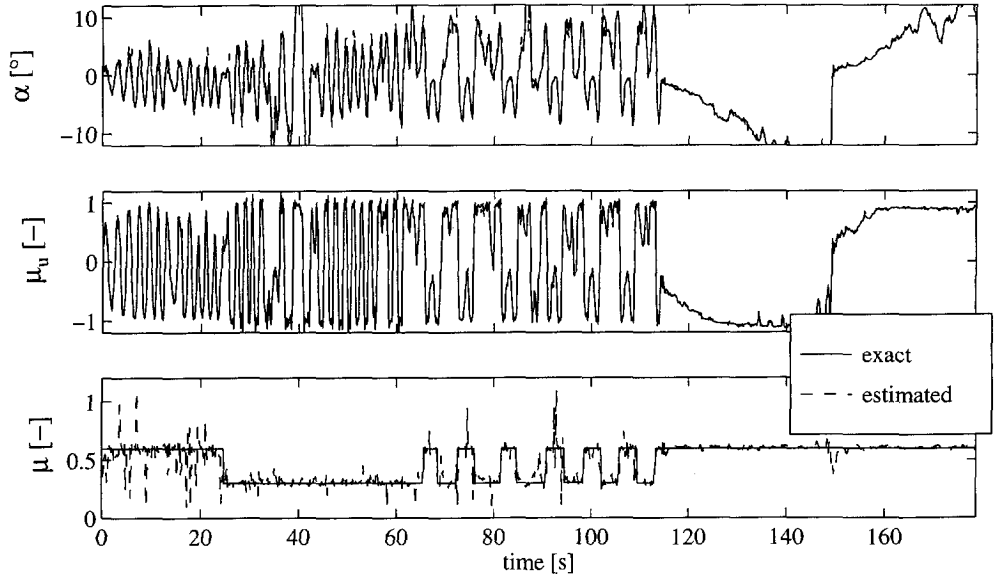

Figure 5.18: *Estimation of α, μ_u and μ from training set (simulation results)*

5.4.4. Enhancement of the estimates by filtering

The friction estimate can be enhanced by applying a weighted moving average filter, built by keeping a number of previous μ-estimates, weighted with their respective

values of $|\mu_u|$, in a buffer of fixed length. This buffer is only updated if $|\mu_u|$ exceeds some threshold value, in this case chosen to be 0.3. The rationale for this is that it is probably better to keep a reliable old estimate than replace it by an unreliable new estimate. However, this implies that the phase lag of this filter is variable. Tuning of this filter is a trade off between accuracy and phase lag. Figures 5.19 to 5.22 show the results for the test set. This test set includes slalom and lane change manoeuvres on high and low friction road surfaces. The filtered results are shown by thick dashed lines.

If $|\mu_u|$ is smaller than the threshold value of 0.3, the tyre behaviour is approximately linear (almost complete adhesion friction) and independent of μ, hence a reliable estimate of the actual friction cannot be made. This threshold value is rather arbitrarily chosen, since there is a continuous transition from adhesion to sliding with increasing $|\mu_u|$. Furthermore, such a threshold depends on the tyre properties and on the experimental setup, as is also demonstrated by the experiments with the tyre test trailer, and on the required accuracy and may therefore vary with other experiments. It is also conceivable to use other types of filters, but major improvements are not to be expected as they are limited by the physical properties of the tyre. It is noted that other research [54], although based on a different method, reports similar results regarding a minimum degree of friction utilisation to enable friction estimation.

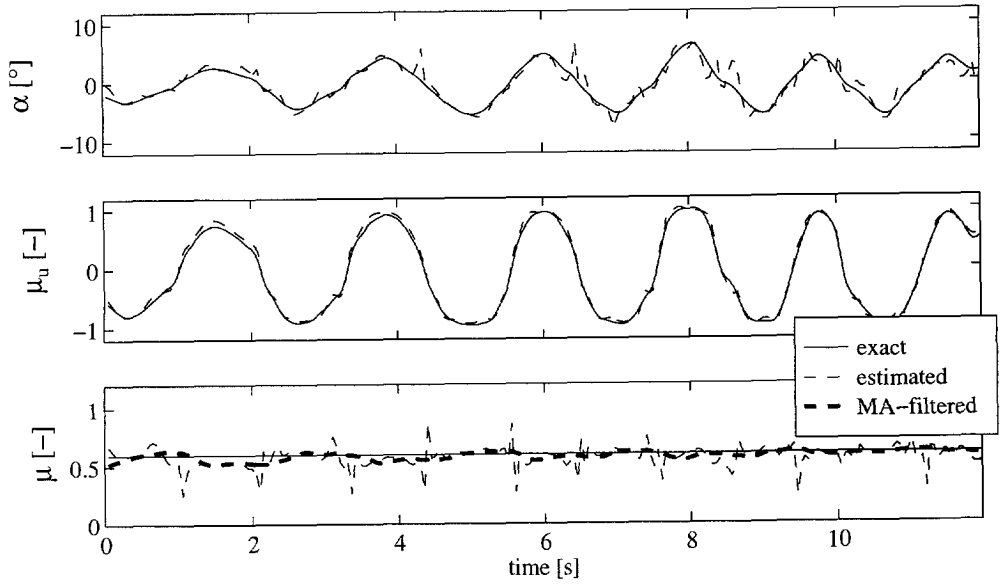

Figure 5.19: *Estimation of α, μ_u and μ from test set (simulation results): slalom on high friction surface*

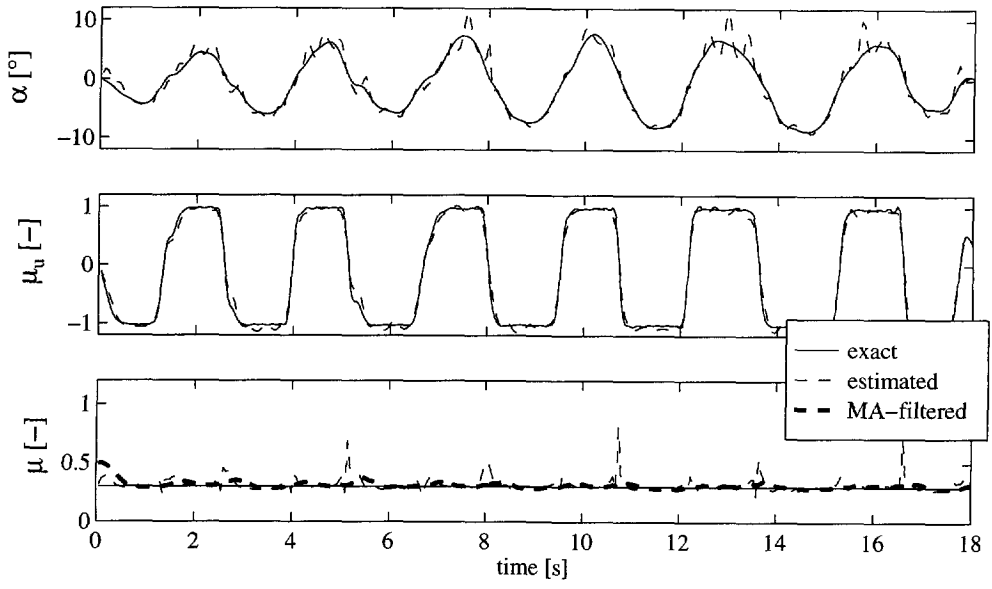

Figure 5.20: *Estimation of α, μ_u and μ from test set (simulation results): slalom on low friction surface*

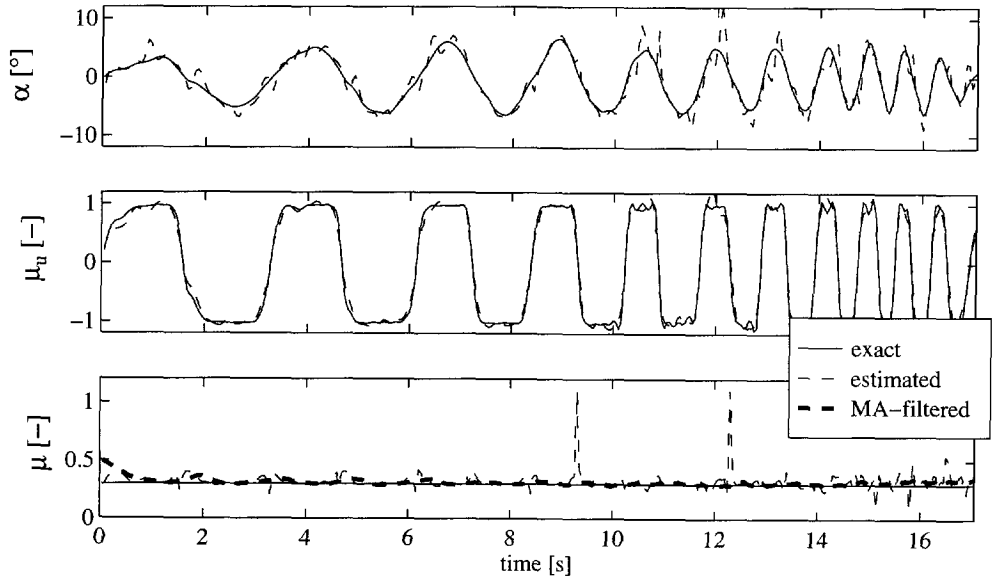

Figure 5.21: *Estimation of α, μ_u and μ from test set (simulation results): slalom with increasing steering frequency on low friction surface*

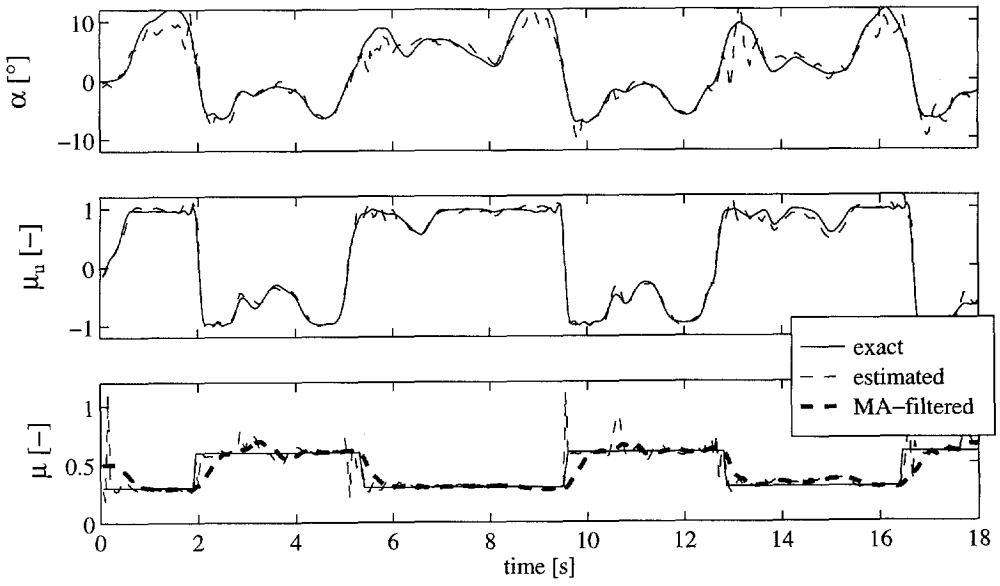

Figure 5.22: *Estimation of α, μ_u and μ from test set (simulation results): lane changes on low and high friction surfaces*

5.4.5. Experiments with the test vehicle

The next step is to identify friction from measured signals using the actual test vehicle. The measured data consist of a series of manoeuvres on two different road surfaces with friction coefficients of approximately 0.4 and 0.8. Note that since the actual friction coefficient is a function of many parameters that may change during the experiment, only approximate values can be given. For these data, a neural network was designed using the Genetic Algorithm approach discussed in Chapter 4. The data was split in three sets: two sets to determine the network structure and to train and validate the network, and another, independent test set to determine the overal performance of the final, trained network.

Neural network architecture optimization by Genetic Algorithms

The GA optimization of the network architecture was carried out in two steps. In the first step, the inputs were selected from the 6 available inputs, the numbers of hidden nodes in the one or possibly two hidden layers were chosen and the activation functions in the hidden and output layers are chosen from three alternatives: linear, logistic or hyperbolic tangent (see Section 4.4.3 on these functions). Since such an optimization run is extremely time consuming, the population was set to a modest 20 members, and the optimization ran for 20 generations. The number of hidden nodes in the first and second layers were

constrained to a maximum of 16 and 8 respectively, for the same reason of computational burden. The fitness is calculated as a function of the acquired accuracy, while network complexity (i.e. more network parameters) is penalized following Eq. 4.15, repeated here for convenience:

$$F = test\_accuracy\left(1 + INI\left(1 - \frac{in}{in_{\max}}\right) + HNI_1\left(1 - \frac{hn_1}{hn_{1,\max}}\right) + HNI_2\left(1 - \frac{hn_2}{hn_{2,\max}}\right)\right) \tag{5.12}$$

where the node influence factors have chosen as:

$INI = 0$; $HNI_1 = 0.05$; $HNI_2 = 0.1$

This choice is rather subjective, but aims to express a preference for low complexity, single layer networks, while not excluding the possibility of a second hidden layer if that is really beneficial.

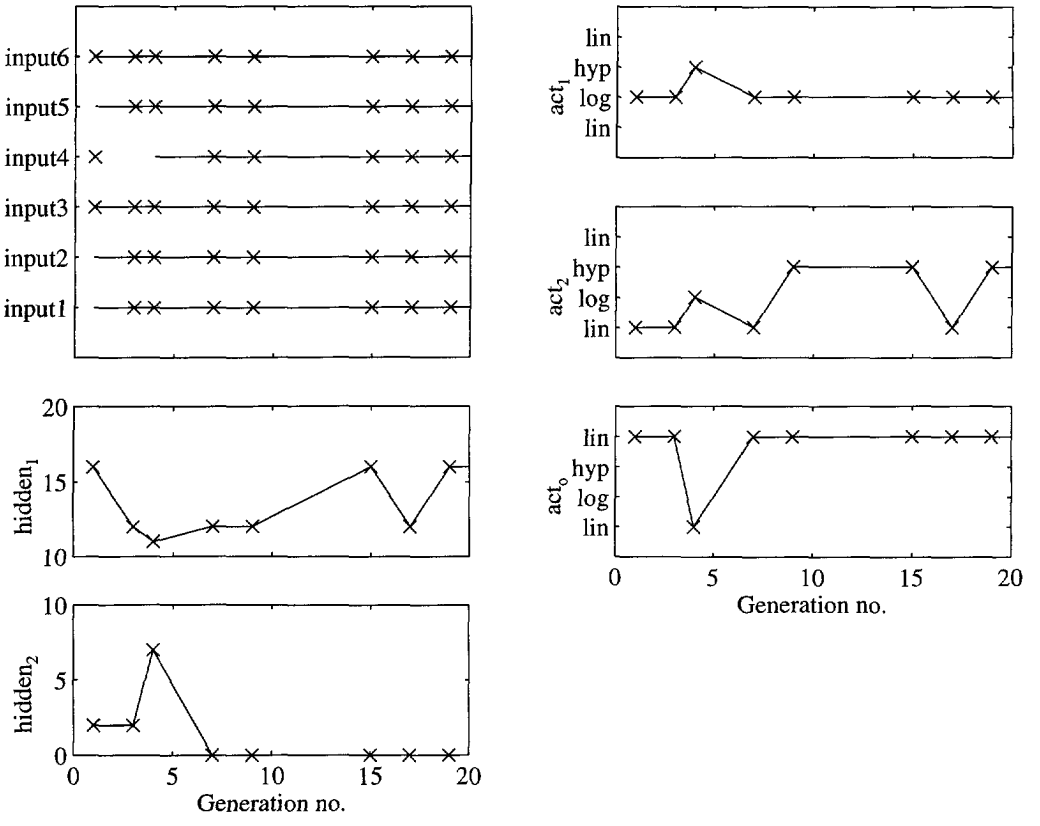

Figure 5.23: *Parameter evolution of the first GA-run to optimize the neural network architecture*

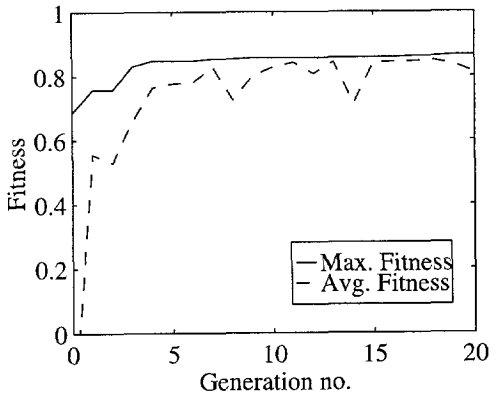

Figure 5.24: *Maximum and average fitness of the successive populations of the first GA-run to optimize the neural network architecture*

This optimisation run resulted in the parameter evolution shown in Figure 5.23. The maximum and average fitnesses of the successive generations are displayed in Figure 5.24. From this optimization run it becomes clear that all inputs to the network are relevant and have to be included for best performance. Furthermore, it seems that the maximum number of hidden nodes chosen was too small for the first hidden layer. A second hidden layer seems to be unnecessary. Either logistic or hyperbolic tangent functions can be used as activation functions for the hidden layer, but clearly linear activation functions have to be used for the output layer.

Since the hyperbolic tangent function can be seen as a scaled logistic function, it is easily understood that no clear preference for one or the other function to serve as activation function in the hidden layers shows up. The output function, however, needs to be linear to cover the range of output values. Therefore, a second optimization run was conducted, optimizing only the choice of input signals and the numbers of nodes in the hidden layers. For the first hidden layer the maximum number of nodes was set to 32, and for the second to 8. The activation functions were set to hyperbolic tangent for the hidden layers, and linear for the output layer. The fitness calculation remained the same. Figure 5.25 shows the parameter evolution for this optimization run and Figure 5.26 shows the accompanying fitness for the succesive generations. The population size was again set to 20 members and the optimization ran for 20 generations. The parameter evolution converged to form an optimal neural network architecture with a single hidden layer containing 30 nodes.

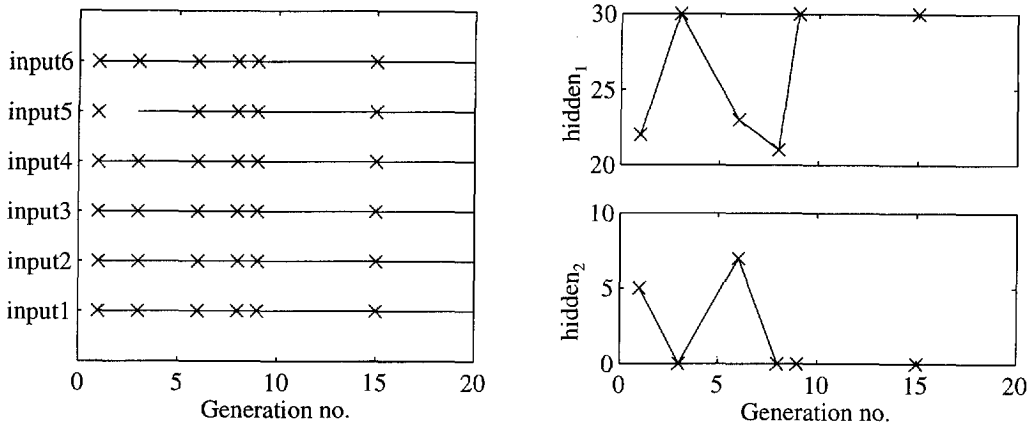

Figure 5.25: *Parameter evolution of the second GA-run to optimize the neural network architecture*

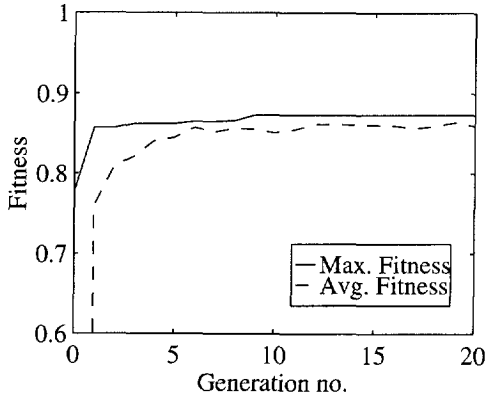

Figure 5.26: *Maximum and average fitnees of the successive populations of the second GA-run to optimize the neural network architecture*

Neural network results on training and validation sets

The single hidden layer neural network with 30 hidden nodes results in the following training results. Figures 5.27 and 5.28 show the results of the neural network on the training and validation set that were used to determine the structure of the net using the GA and the weights in the network training.

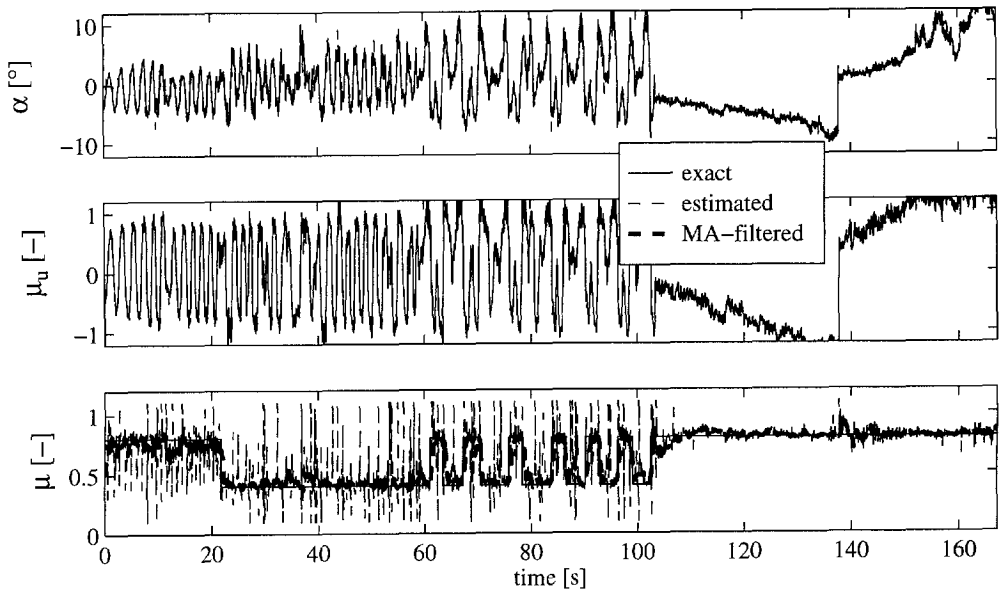

Figure 5.27: *Results on training set*

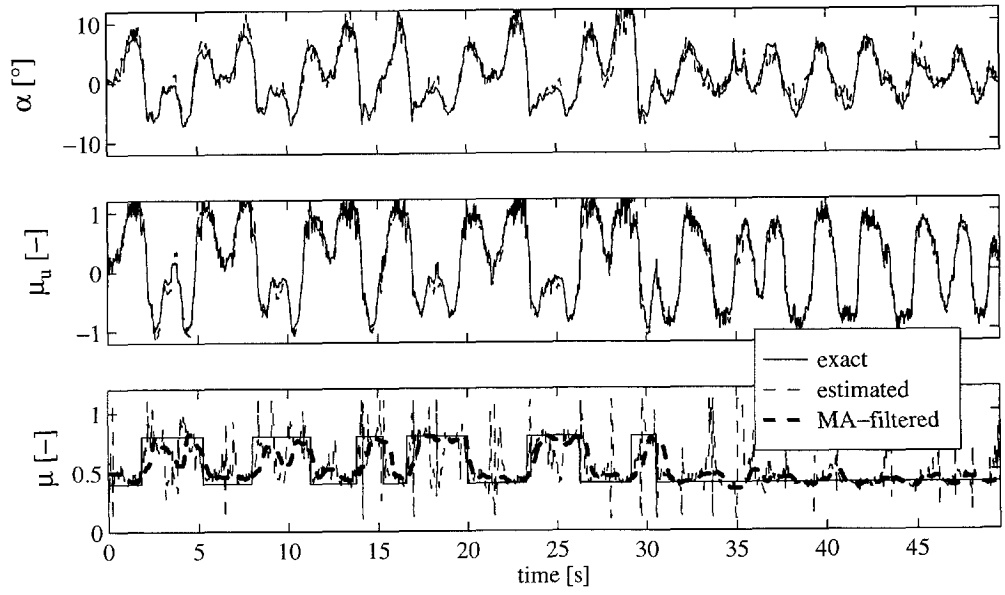

Figure 5.28: *Results on validation set*

Neural network results on the test set

Figures 5.29 to 5.32 show the results on the independent test set, which gives an unbiased measure of the network performance. This test set contains four different manoeuvres: slalom manoeuvres on high and low friction surfaces, a slalom with increasing steering frequency (a sweep) on low friction surface, and finally a series of lane change manoeuvres, changing from high to low friction lane and vice versa. Like the simulation test results, the friction estimates were filtered using a weighted moving average filter. These filtered results are indicated by the thick, dashed lines.

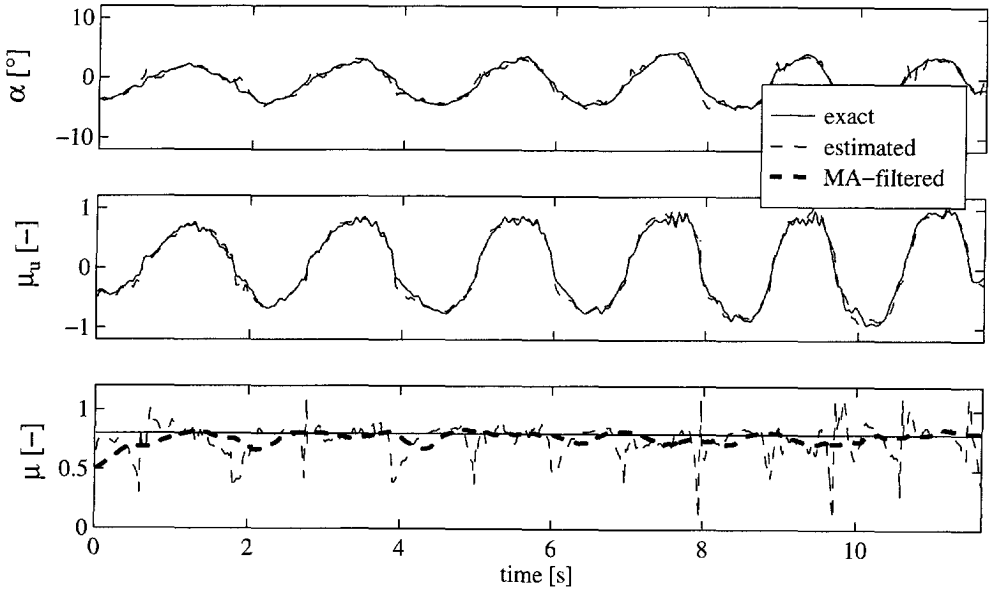

Figure 5.29: *Estimation α, μ_u and μ from test data: slalom on high friction surface*

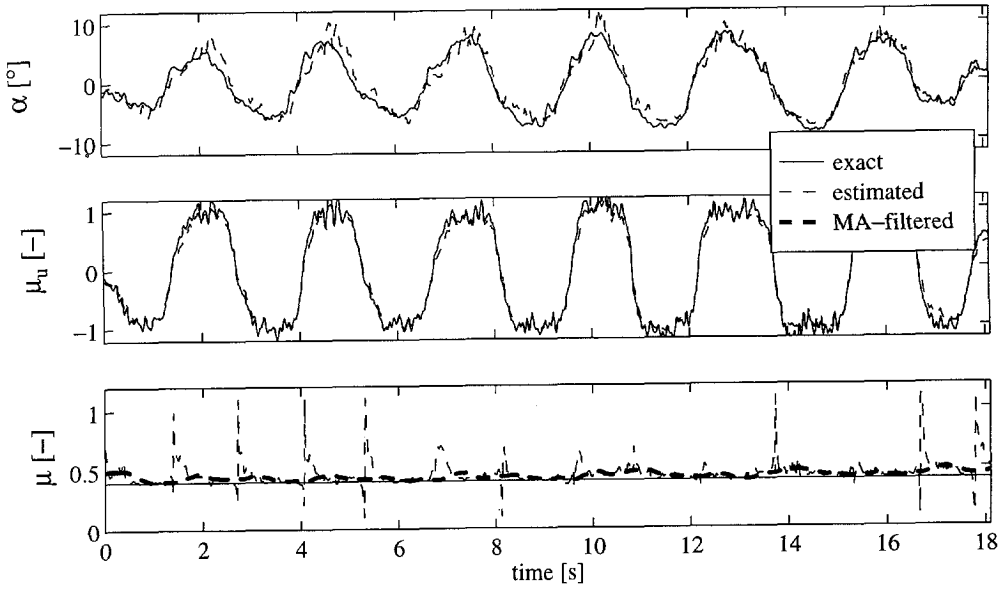

Figure 5.30: *Estimation α, μ_u and μ from test data: slalom on low friction surface*

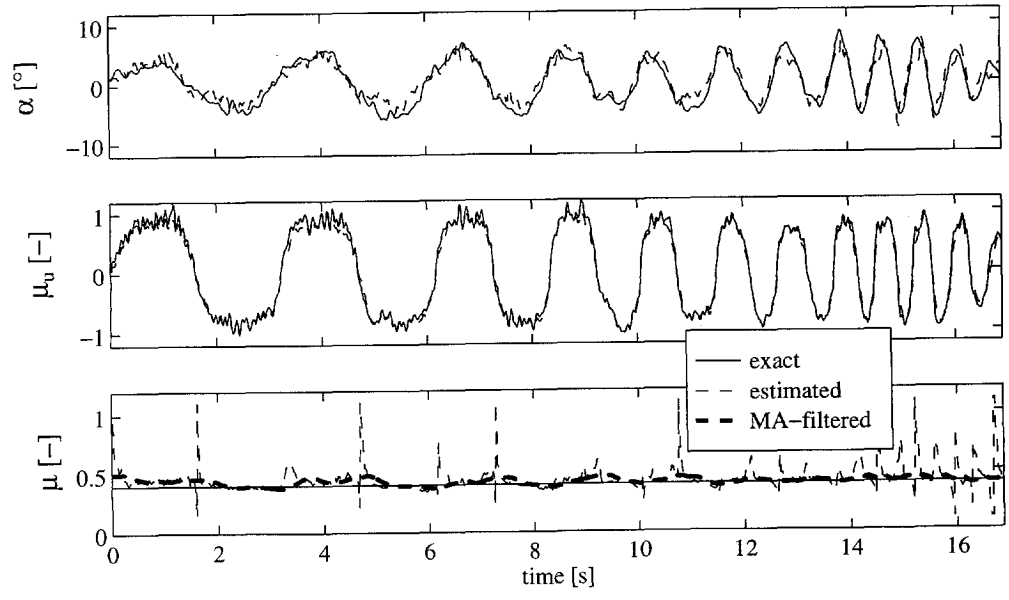

Figure 5.31: *Estimation α, μ_u and μ from test data: slalom with increasing frequency on low friction surface*

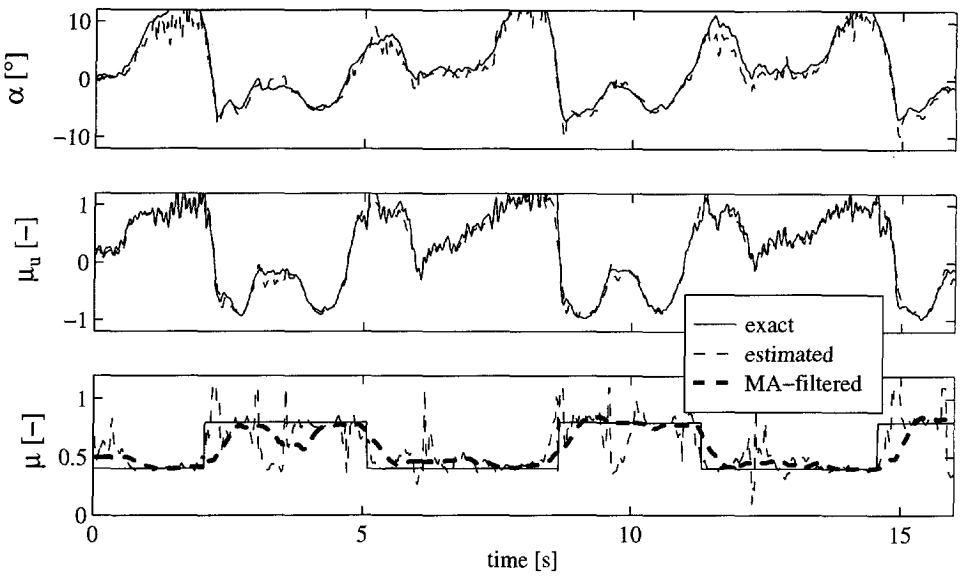

Figure 5.32: *Estimation α, μ_u and μ from test data: lane change manoeuvres on high and low friction surface*

Error distribution as a function of utilised friction

As has been remarked before, the accuracy of the side slip and friction estimates is strongly dependent on the degree of friction utilisation. The data samples of the test set were sorted into 10 categories of absolute utilised friction, ranging from 0 to 1 with increments of 0.1. For these categories, the mean and the standard deviation of the absolute error $|\varepsilon_i|$, $i = \alpha, \mu_u, \mu$ were calculated (before filtering with the moving average filter). Figure 5.33 shows the mean error and the mean error plus the standard deviation of the error on the friction estimate for the test data set. It needs to be realised that the errors displayed in these graphs are partially due to the error in the assumed actual tyre to road friction coefficient. The assumed actual friction values of 0.4 and 0.8 for the low and high friction tracks are only accurate within about 0.1.

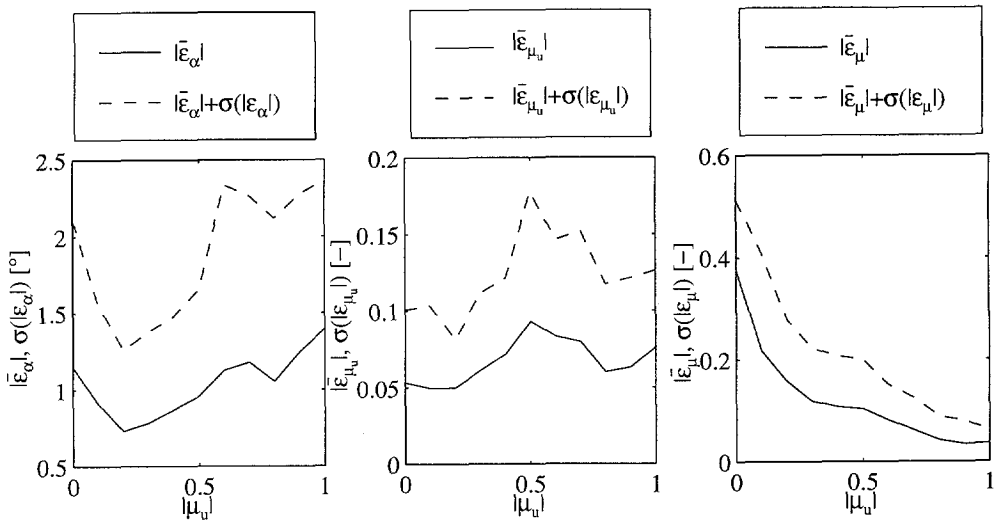

Figure 5.33: *Error of friction coefficient and side slip angle estimates on test set*

Nevertheless, these results show that reasonably accurate friction estimates can be made at friction utilization levels higher than about 0.3, while the side slip angle estimates are reasonably accurate up to a level of friction utilization of about 0.6. These measures are of course rather subjective. It is also noted that the estimation of utilised friction is very accurate. Therefore, it is possible to indicate the expected accuracy of the estimates of the tyre to road friction coefficient and the side slip angle.

5.5. External disturbances

The practical applicability of the proposed method to identify the tyre to road friction coefficient and the side slip angle depends heavily on the robustness of the method with respect to various common disturbances. It is beyond the scope of this research to study their various effects on the identification results in detail. However, a more general discussion already provides insight with respect to the expected robustness of the method to various disturbances.

The disturbances are subdivided according to their sources. We distinguish tyre related disturbances, vehicle (excluding the tyres) related disturbances, road induced disturbances and disturbance due to side wind. These will be discussed in the following sections.

5.5.1. Tyre induced disturbances

Tyre inflation pressure

The tyre inflation pressure is usually variant in time, due to poor maintenance and temperature effects. The tyre contact length and the tyre carcass stiffness are both related to the inflation pressure. It is therefore important to either monitor the inflation pressure and account for changes, or to control the tyre inflation pressure in order to have proper behaviour of the side slip angle and friction coefficient identification. The extreme case, a flat tyre, will make the identification procedure invalid.

Tyre temperature

The tyre temperature changes due to weather conditions (outside temperature, heat transfer to and from pavement or lubricant (rain)) and due to hysteresis and frictional forces. Although it is generally understood that the tyre characteristics are dependent on the tyre temperature, it is not clear yet how and to what extent this will affect the friction identification method. If the effects are known and the tyre temperature is available, it seems likely that the effects of a changing temperature on the identification method could be accounted for.

Changing tyres

Tyres all have individual properties, even when taken from the same production batch. Therefore, if the tyres are changed, the parameters of the identification procedure have to be updated. Some of these parameters can be easily identified, for example the residual forces and torques can be found by driving straight ahead without external disturbances such as side wind or road banking, but if another type of tyre is applied, a more advanced self-learning algorithm will be needed.

Tyre wear

Owing to tyre wear, the cornering and brake slip stiffnesses of a tyre usually increase on dry roads, but on wet roads their drainage capacity may fall short, resulting in early skidding. Furthermore, the tyre's residual forces and torques tend to become more prominent as the tyre wears. Thus, the tyre behaviour may become quite different.

It would be useful to update the identification procedure for this effect also by a self-learning algorithm. It may be feasible to assess the longitudinal slip stiffness of the tyre using the ABS System. This slip stiffness will increase with progressive wear of the tyre. By using this information as an indicator of tyre wear, the tyre parameters of the friction identification method may be adjusted.

5.5.2. Varying vehicle dynamic properties

The dynamic properties of a vehicle may vary considerably owing to, for example, the number of passengers and load in the trunk. Apart from the fact that the friction utilisation depends to some extent on the vehicle dynamic properties, the friction identification is expected to be robust for these disturbances.

5.5.3. Road induced disturbances

Banking, crowning and truck ruts

A vehicle driving straight ahead on a banked road, will experience lateral forces on the wheels due to the lateral component of the gravity forces. For the same reason, the vehicle body will have a roll angle. The driver has to give a countersteering input to the steering wheel to force the car to follow a straight course. Thus, we have a situation similar to pure cornering on a level road. Therefore, the identification of side slip angle and friction coefficient is not different from normal cornering.

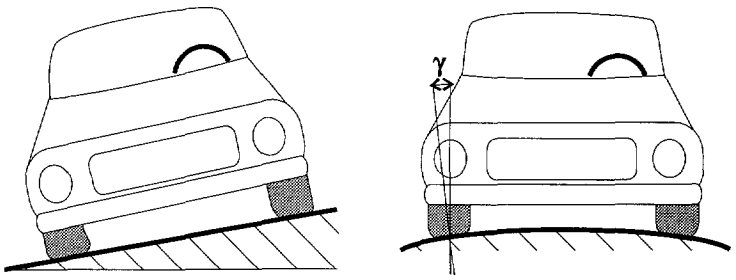

Figure 5.34: *Road banking (left) and crowning (right)*

Road crowning causes opposite camber angles at left and right wheels, while the vehicle may still pursue a straight course. This camber angle is not related to cornering of the vehicle, and is thus a disturbing input. As shown in Chapter 2, a camber angle primarily causes a shift in the forces and torques, which affects the identification of side slip angle and friction coefficient and may cause erroneous results.

Truck ruts in the road (tram-lining) force the wheels of the vehicle to take a course that the driver may not have intended to follow. The normal forces between the deformed road and the tyre may have components in planar direction, and since these forces are usually not uniformly distributed over the tyre contact length, they may also cause a torque around the vertical axis of the tyre. Thus, the perception of

side force and aligning torque may be severely disturbed by the ruts and so the identification of side slip angle and friction coefficient may be erroneous.

Soft soil or snow

Driving over soft surfaces such as sand or snow may cause the wheels to form ruts in the soil. In addition to the problems with ruts, as discussed previously, the material in front of the tyre causes resistance forces in longitudinal direction on the wheel (Fig. 5.35).

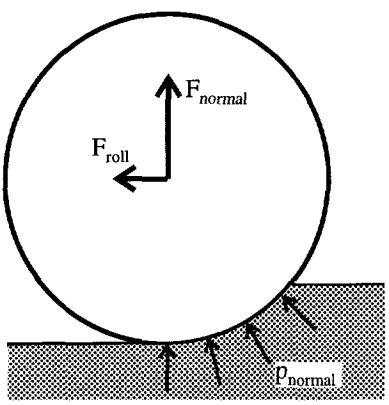

Figure 5.35: *Normal forces applied to the tyre when driving in soft soil*

This force is not a frictional force of the tyre. If no appropriate measures are taken, this will affect the accuracy of the friction identification. Also, when driving in soft soil with for example off-road vehicles, the pressure distribution over the contact area and the shape of the contact area may be quite different from those experienced when driving on firm road surfaces. This will affect the build up of side force and aligning torque in the contact area. In addition, shear forces may be built up in the soil that are imposed on the tyre.

Aquaplaning

If the tyre is unable to drain the water between tyre and road surface sufficiently, a film of water will build up between the tyre and the road. At the leading edge of the contact area, a wedge of water will be formed that the tyre tries to climb. Due to these effects, the tyre contact area may be severely diminished and shifted towards the trailing edge of the contact length. This behaviour can be learned by the neural network used for identification, and thus the identification method can be made robust with regard to aquaplaning.

Road unevenness and roughness

Road unevenness results in a varying normal wheel load which leads to loss of lateral tyre force, as shown by [61]. This probably has two main causes. Firstly, since the cornering stiffness increases less than proportional to the normal tyre load, the effective cornering stiffness is lower than would be obtained if the average wheel load were applied statically. Secondly, there is transient behaviour related to the tyre relaxation length. It has been found that this behaviour is due to the increase of the relaxation length with the vertical tyre load. At small slip angles, this results in a loss of cornering and braking forces, as well as a loss of aligning torque. However, at large side slip angles (beyond the slip angle at maximum aligning torque), the aligning torque actually increases due to the load oscillations. The lateral force continues decreasing, even at these large slip angles.

With regard to the identification method, the first cause can be accounted for by monitoring the amplitude of load oscillations. The situation is more complicated for the second cause, since the slip angle is an unknown variable beforehand. For small slip angles, the side force and aligning torque will decrease proportionally, such that the identification method will find a smaller friction estimate. For larger slip angles, this no longer holds. However, since the slip angle is not known a priori, this may not be recognized.

The effects of road unevenness on the tyre behaviour are still subject of research in the Vehicle Research Laboratory at the Delft University of Technology. The effect of road unevenness on the friction identification method is not entirely predictable at this point.

5.5.4. Side wind

The lateral components of the integrated side wind forces acting on the vehicle can be thought of being concentrated in a force F_{wind} acting on the side wind pressure point, somewhere on the vehicle body. This force naturally depends on variables such as air speed, air density and area on which the wind force is acting. The force F_{wind} may be replaced by a combination of a side force $F_{y,w}$, acting in the centre of gravity of the vehicle, a (yaw) moment around the z-axis $M_{z,w}$ and a (roll) moment about the x-axis $M_{x,w}$.

If we consider one wheel with suspension, friction estimation is not hindered by side wind. The extra body side force will result in an increased tyre side force and self aligning torque and thus create an extra side slip angle. The moments $M_{z,w}$ and $M_{x,w}$ will affect the distribution of side forces over the wheels of the vehicle, but will not disturb the identification at an individual wheel.

5.6. Conclusions of this chapter

This chapter has built a bridge between theory and practice with regard to the identification of the tyre to road friction and the side slip angle. First, mathematical vehicle models were built in order to be able to simulate the friction estimation method. A fairly simple and fast calculating, yet non-linear model with three degrees of freedom was built using Matlab/Simulink, while a more elaborate model with 17 degrees of freedom was built using multi-body software (BAMMS). The first model was used to obtain insight in the vehicle behaviour and to make rough estimates of the behaviour of the identification method. It was also used to generate steering files for use with the tyre test trailer. The second model describes the vehicle, and in particular the front wheel suspension, in greater detail, thus providing accurate simulations of the actual vehicle and suspension behaviour.

The identification method was verified by experiments with the tyre test trailer under various road conditions. The identification method proved to be valid, both in steady state side slip angle sweeps and in simulated manoeuvres of an actual vehicle. As expected on the basis of the theory explained in the preceeding chapters, the friction estimate improved in accuracy with increasing friction utilization, while the side slip angle estimate improved with decreasing friction utilization. Even though the identification method assumes quasi-static tyre behaviour, it produced reasonable results when transient tyre behaviour starts to play a role.

Implementation of the identification method in a standard vehicle required the development of a measurement system to determine the tyre forces and self aligning torque and the wheel orientation with respect to the vehicle body. This was achieved by using fairly inexpensive sensors and with the aid of a feedforward neural network to describe the strongly nonlinear suspension kinematics.

Experiments with the instrumented vehicle were conducted on two types of road surfaces, which had low and high friction properties respectively. The experiments conducted were also 'played back' in the BAMMS simulation model. The simulation results were very similar to the measured vehicle respones, thereby validating the BAMMS model. Moreover, the identification results of both the simulated and the measured data sets were similar and again showed both the validity of the identification method and the limitations, imposed by the tyre behaviour. The error in the friction estimate appears to be a function of the utilized friction, as we would expect from the theory. If the friction utilization is below about 30% of the friction potential, the friction estimates are unreliable. The friction estimate can be improved by applying a weighted moving average filter, using the absolute utilized friction as weighting factor. Tuning this filter depends on the required accuracy and maximum allowable phase lag.

Unfortunately, the friction estimator could not be tested at other road surfaces, such as packed snow. Furthermore, because of limited resources only one front wheel suspension of the test vehicle was instrumented. It would however be recommendable to instrument the suspension at both front wheels.

Finally, some common disturbances that were not actually considered in this research have been regarded qualitatively. Unfortunately, it is to be expected that the friction and side slip angle identification method will prove to be quite sensitive to tyre induced disturbances, such as loss of inflation pressure, tyre temperature and wear and changing of tyres. It will therefore be necessary to monitor these variables periodically. The identification method is expected to be robust with regard to variations in vehicle mass and inertia properties as well as to side wind disturbances. The same holds true for road banking and grading, but truck ruts and soft soil may disturb the identification severely. The method could probably be made robust to cope with aquaplaning, but the effects of road unevenness and roughness are not yet well enough understood to predict the robustness of the identification method with regard to these disturbances. It would be recommendable to do further research to determine the actual sensitivity of the estimator to the various disturbances.

Integration of Friction Estimates into Advanced Vehicle Control Systems

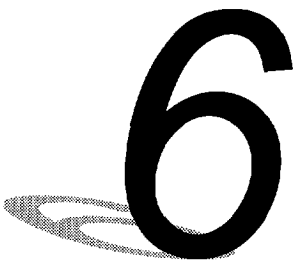

6.1. Introduction

As already mentioned in the first chapter of this thesis, every application puts its own demands on a friction and side slip angle estimator. Therefore, the aim of this chapter is to illustrate the benefits integration of the proposed friction estimator could contribute to a few popular vehicle control systems as well as its possible limitations. More specifically, we will study four-wheel steering and active yaw control, and automatic distance keeping. However, since these control systems are not the main subject of this thesis, we will only study a rather basic approach to control design.

6.2. Independent Four-Wheel Steering with Friction Compensation

6.2.1. The obstacle avoidance problem

In this section we study the effects of friction changes and non-linear tyre behaviour on obstacle avoidance manoeuvering with a four-wheel steering vehicle on a μ-split road first without and then with information on the actual friction coefficient and friction utilisation.

Figure 6.1 sketches the obstacle avoidance problem. It is assumed that a trajectory to be followed by the vehicle is defined by some external means. The forward speed of the vehicle is assumed to stay at a constant value of 20 m/s throughout the manoeuvre. In y-direction, the trajectory exhibits a smoothed step function that has been generated using a logistic function (see Eq. 4.8). The step size is 4 meters, which is about the width of a highway lane. The controller has to steer the wheels in a way such that the desired trajectory is tracked. Thus, the controller replaces the

human driver in the steering control loop. This has been chosen primarily to simplify the analysis, but it is not inconceivable that such a system would actually be incorporated in an automated highway system, as will be discussed later. In that respect, it has been suggested that magnetic markers or road marking may be used to define the desired trajectory, while also direct communication between the road administrator and the vehicles (e.g. for obstacle avoidance manoeuvres) is not unthinkable [30].

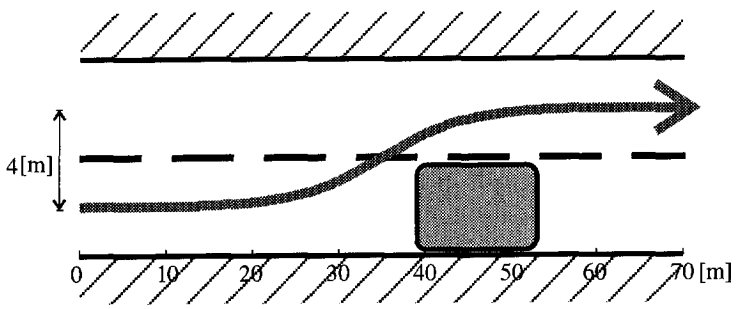

Figure 6.1: *The obstacle avoidance problem*

In this case, for simplicity we study a fairly simple feedforward/feedback system without preview. It is, however, well known that adding preview is beneficial for the four-wheel steering control performance, see for example [34, 50]. The four-wheel steering control problem has been extensively studied over the past decades. The feedback control as described below is more or less a standard design, previously described in for example [1].

6.2.2. Single track vehicle model

The feedback control design is based on the optimal control technique known as LQ (Linear Quadratic) control. A single track vehicle model ('bicycle model') with two degrees of freedom (lateral and yaw) described by

$$\begin{aligned} m(\dot{V}_y + Vr) &= F_{y_f} + F_{y_r} \\ I\dot{r} &= aF_{y_f} - bF_{y_r} \end{aligned} \tag{6.1}$$

where the lateral tyre forces at the front and rear axles are lumped by

$$\begin{aligned} F_{y_f} &= F_{y_1} + F_{y_2} \\ F_{y_r} &= F_{y_3} + F_{y_4} \end{aligned} \tag{6.2}$$

has been used for the controller design. This single track model is a simplified version of the model with three degrees of freedom discussed in Chapter 5: the roll degree of freedom, the load transfer and all non-linearities are omitted. The lateral

tyre characteristics are approximated by the (negative) cornering stiffnesses C_f and C_r and the sideforces at the axles are calculated by

$$\begin{aligned} F_{y_f} &= C_f \alpha_f \\ F_{y_r} &= C_r \alpha_r \end{aligned} \tag{6.3}$$

The sideslip angles at the front and rear axles are given by

$$\begin{aligned} \alpha_f &= \frac{V_y + ar}{V} - \delta_f \\ \alpha_r &= \frac{V_y - br}{V} - \delta_r \end{aligned} \tag{6.4}$$

Combining 6.1 through 6.4, we have:

$$\begin{aligned} \dot{V}_y &= \frac{C_f + C_r}{mV} V_y + \left(\frac{aC_f - bC_r}{mV} - V \right) r - \frac{C_f}{m} \delta_f - \frac{C_r}{m} \delta_r \\ \dot{r} &= \frac{aC_f - bC_r}{I_z V} V_y + \frac{a^2 C_f + b^2 C_r}{I_z V} r - \frac{aC_f}{I_z} \delta_f + \frac{bC_r}{I_z} \delta_r \end{aligned} \tag{6.5}$$

6.2.3. Trajectory tracking

After [34], the desired trajectory is defined by the trajectory curvature ρ as a function of distance s. The distance s is measured along the trajectory which may be curved. Assuming a constant forward speed of the vehicle, we have

$$s(t) = V_x t \approx Vt \tag{6.6}$$

The curvature is defined by the rate of change of the heading angle ψ_r of the tangent to the desired trajectory to s:

$$\rho(s) = \frac{\mathrm{d}\psi_r}{\mathrm{d}s} \tag{6.7}$$

The radius of the curvature is the reciprocal value of ρ. The difference between the heading angle of the vehicle and the heading angle of the desired trajectory is the heading error $\Delta\psi$, while Δy represents the lateral offset of the vehicle's centre of gravity to the desired trajectory. These definitions are illustrated by Figure 6.2.

Assuming that the vehicle side slip angle $\beta = V_y / V$ and the heading angle error $\Delta\psi$ are small, we have

$$\begin{aligned} \Delta\dot{y} &= V_y + V\Delta\psi \\ \Delta\dot{\psi} &= r - V\rho(s) \end{aligned} \tag{6.8}$$

and assuming a constant curvature we have

$$\Delta\ddot{y} = \dot{V}_y + V\Delta\dot{\psi}$$
$$\Delta\ddot{\psi} = \dot{r} \tag{6.9}$$

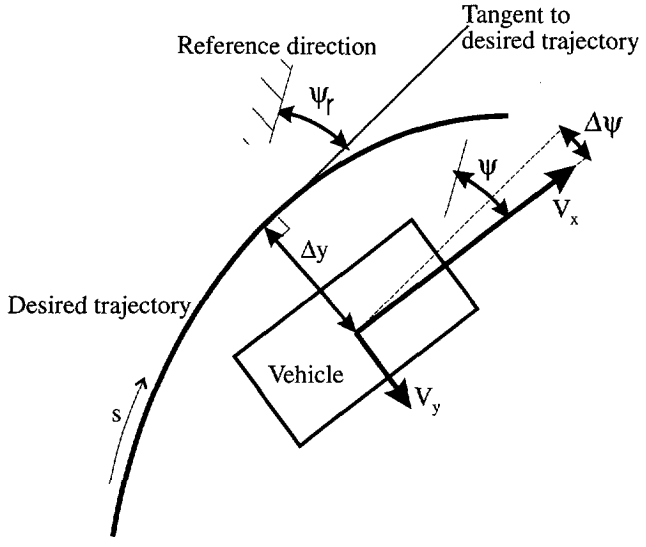

Figure 6.2: *Trajectory tracking*

6.2.4. Linear feedforward-feedback control

With 6.5, we can formulate the tracking problem as a regulator problem with a state space description that is suitable for LQ control:

$$\dot{\mathbf{x}} = \mathbf{A}\mathbf{x} + \mathbf{B}\mathbf{u} + \mathbf{F}\mathbf{w} \tag{6.10}$$

with

$$\mathbf{x} = \left[\Delta y \quad \Delta\dot{y} \quad \Delta\psi \quad \Delta\dot{\psi}\right]^T;\ \mathbf{u} = \left[\delta_f \quad \delta_r\right]^T;\ \mathbf{w} = \rho^T$$

$$\mathbf{A} = \begin{bmatrix} 0 & 1 & 0 & 0 \\ 0 & \frac{C_f + C_r}{mV} & -\frac{C_f + C_r}{m} & \frac{aC_f - bC_r}{mV} \\ 0 & 0 & 0 & 1 \\ 0 & \frac{aC_f - bC_r}{I_z V} & -\frac{aC_f - bC_r}{I_z} & \frac{a^2C_f + b^2C_r}{I_z V} \end{bmatrix};\ \mathbf{B} = \begin{bmatrix} 0 & 0 \\ -\frac{C_f}{m} & -\frac{C_r}{m} \\ 0 & 0 \\ -\frac{aC_f}{I_z} & \frac{bC_r}{I_z} \end{bmatrix};\ \mathbf{F} = \begin{bmatrix} 0 \\ \frac{aC_f - bC_r}{m} - V^2 \\ 0 \\ \frac{a^2C_f + b^2C_r}{I_z} \end{bmatrix}$$

The LQ method to determine the optimal feedback control law involves the minimization of the cost function:

$$J = \int_0^\infty \left\{x^T(\tau)Qx(\tau) + u^T(\tau)Ru(\tau)\right\} \mathrm{d}\tau \tag{6.11}$$

The weighting matrices **Q** and **R** can be used to trade off the deviations of the states (in this case the heading angle and lateral errors and their time derivatives) from zero and the control effort (in this case the front and rear steer angles). Both the matrices **Q** and **R** must be symmetric and they have to be positive semi-definite and positive definite respectively. By solving the associated Ricatti-equation, the linear, time-invariant state-feedback matrix $\mathbf{K_{fb}}$ is obtained. The feedback law becomes

$$\mathbf{u_{fb}} = -\mathbf{K_{fb}}\mathbf{x} \tag{6.12}$$

which results in excellent tracking of the desired trajectory for this linear model (Fig. 6.4).

However, since we have assumed that the trajectory is known, that is **w** is known, we may also use a static feedforward controller to generate the steering inputs in such a way that the trajectory is followed. If we define the matrices $\mathbf{B_2}$ and $\mathbf{F_2}$ by selecting the second and fourth rows of **B** and **F**, respectively, we obtain the feedforward matrix $\mathbf{K_{ff}}$ by

$$\mathbf{K_{ff}} = -\mathbf{B_2}^{-1}\mathbf{F_2} \tag{6.13}$$

with

$$\mathbf{B_2} = \begin{bmatrix} -\frac{C_f}{m} & -\frac{C_r}{m} \\ -\frac{aC_f}{I_z} & \frac{bC_r}{I_z} \end{bmatrix}; \mathbf{F_2} = \begin{bmatrix} \frac{aC_f - bC_r}{m} - V^2 \\ \frac{a^2C_f + b^2C_r}{I_z} \end{bmatrix}$$

The feedforward law becomes

$$\mathbf{u_{ff}} = \mathbf{K_{ff}}\mathbf{w} \tag{6.14}$$

and the total input

$$\mathbf{u} = \mathbf{u_{fb}} + \mathbf{u_{ff}} \tag{6.15}$$

Figure 6.3 shows a system diagram of this feedforward-feedback control structure.

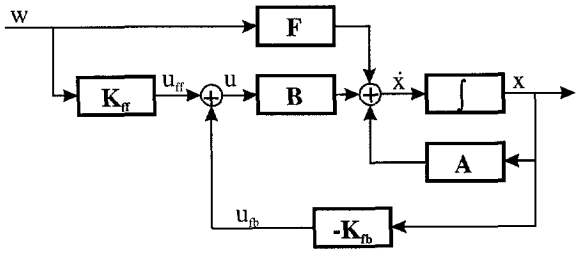

Figure 6.3: *System diagram of the feedforward-feedback system*

For the linear case, the feedforward steering provides perfect tracking on its own, since the 'disturbance' **w** is completely cancelled by the feedforward control. Actually, the feedback is not used at all in this case.

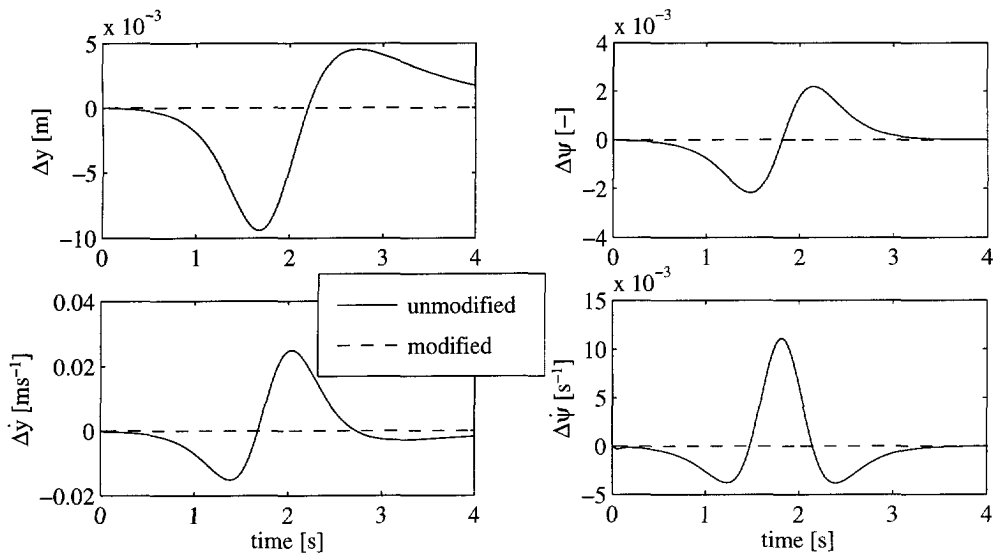

Figure 6.4: *Performance of feedback and feedforward+feedback control on linear model*

The behaviour of the controller under more realisitic conditions is checked by using the nonlinear Simulink model, developed in Chapter 5. This two-track model uses nonlinear DTM-type tyre models for the calculation of the tyre forces, and also features a roll degree of freedom and load transfer. Therefore, when using the simple control laws as developed in this section, the left and right tyres on the front or rear axles will generally have different degrees of friction utilisation. This becomes even more apparent if the tyre to road friction coefficients of left and right wheels are different. In this case, we assume tyre to road friction coefficients of 0.3 for the left wheels and 1.0 for the right wheels. The solid lines in Figure 6.5 show the performance of the feedforward/feedback controller on the Simulink model on the μ-split road. Figure 6.6 shows the friction utilization of each wheel. Note that since the controller has been designed for a single track model, the steering angles of the left and right wheels are the same. Apparently, the degrees of friction utilisation of the tyres are quite different.

6.2.5. Feedforward with friction compensation

From the viewpoint of safety, it may be advisable to balance the friction utilisation of left and right tyres per axle. We discuss this issue for the front axle, while the rear axle is similar. This discussion should be regarded as an exploration of possibilities, it does not aim to design the best performing and robust controller.

Equal friction utilization at the front axle is formulated by

$$\mu_{u_1} = \mu_{u_2} \tag{6.16a}$$

or equivalently,

$$\frac{F_{y_1}}{\mu_1 F_{z_1}} = \frac{F_{y_2}}{\mu_2 F_{z_2}} \tag{6.16b}$$

For the sake of simplicity, we may assume for small slip angles:

$$\frac{F_{y_1}}{F_{y_2}} \approx \frac{\alpha_1 F_{z_1}}{\alpha_2 F_{z_2}} \tag{6.17}$$

Thus we conclude that the objective should be

$$\frac{\alpha_1}{\alpha_2} = \frac{\mu_1}{\mu_2} \tag{6.18}$$

Furthermore, we have (see Eq. 5.6)

$$\begin{aligned} \alpha_1 &= \beta_f - \delta_1 \\ \alpha_2 &= \beta_f - \delta_2 \end{aligned} \tag{6.19}$$

so that we would like to obtain

$$\frac{\beta_f - \delta_1}{\beta_f - \delta_2} = \frac{\mu_1}{\mu_2} \tag{6.20}$$

where β_f is the deviation angle at the front axle. At the same time, we want to maintain the same summed lateral forces per axle. Since we know both the actual tyre to road friction coefficient and the friction utilisation, we can modify for example the feedforward control law to try to fulfil these demands. A simple modification is proposed, where the steering angle at each wheel is increased or decreased, depending on the tyre to road friction at the wheels. The new feedforward steering angles are defined by

$$\begin{aligned} \delta_{ff_1} &= \delta_{ff_f} + \Delta\delta_{ff_1} \\ \delta_{ff_2} &= \delta_{ff_f} + \Delta\delta_{ff_2} \end{aligned} \tag{6.21}$$

If the feedforward controller is effective, we may assume that the feedback control action is relatively small, such that the feedforward steering angles are approximately equal to the total steering angles:

$$\delta_i \approx \delta_{ff_i} \quad (i = 1..4) \tag{6.22}$$

The requirement that the total side force per axle remains the same results in

$$\left(\beta_f - \delta_{ff_1}\right)F_{z_1} + \left(\beta_f - \delta_{ff_2}\right)F_{z_2} = \left(\beta_f - \delta_{ff_f}\right)F_{z_1} + \left(\beta_f - \delta_{ff_f}\right)F_{z_2} \tag{6.23}$$

With Eq. 6.21 we find

$$\left(\delta_{ff_f} + \Delta\delta_{ff_1}\right)F_{z_1} + \left(\delta_{ff_f} + \Delta\delta_{ff_2}\right)F_{z_2} = \delta_{ff_f}\left(F_{z_1} + F_{z_2}\right) \tag{6.24a}$$

and

$$\Delta\delta_{ff_1} = -\Delta\delta_{ff_2}\frac{F_{z_2}}{F_{z_1}} \tag{6.24b}$$

From Eq. 6.20 to 6.22 we obtain

$$\Delta\delta_{ff_2} = -\frac{\mu_2}{\mu_1}\left(\beta_f - \delta_{ff_f} - \Delta\delta_{ff_1}\right) + \beta_f - \delta_{ff_f} \tag{6.25}$$

and combined with Eq. 6.24 we have

$$\Delta\delta_{ff_2} = \frac{\mu_1 F_{z_1}}{\mu_1 F_{z_1} + \mu_2 F_{z_2}}\left(\beta_f - \delta_{ff_f}\right)\left(1 - \frac{\mu_2}{\mu_1}\right) \tag{6.26}$$

Similarly, for the rear axle we define

$$\begin{aligned} \delta_{ff_3} &= \delta_{ff_r} + \Delta\delta_{ff_3} \\ \delta_{ff_4} &= \delta_{ff_r} + \Delta\delta_{ff_4} \end{aligned} \tag{6.27}$$

and we derive

$$\Delta\delta_{ff_3} = -\Delta\delta_{ff_4}\frac{F_{z_4}}{F_{z_3}} \tag{6.28}$$

$$\Delta\delta_{ff_4} = \frac{\mu_3 F_{z_3}}{\mu_3 F_{z_3} + \mu_4 F_{z_4}}\left(\beta_f - \delta_{ff_f}\right)\left(1 - \frac{\mu_4}{\mu_3}\right) \tag{6.29}$$

This results in less steering input to the wheels at low friction and vice versa. Actually, the modification of the steering input is a little too strong, due to the nonlinear tyre characteristics and the many simplifications that have been made in the controller design proces.

The modified feedforward steering inputs compared to the original feedforward steering inputs are shown in Figure 6.7. The summed lateral forces per axle vary somewhat due to this modification, but this is corrected by the feedback controller. The overall result is that the differences of friction utilization of left and right wheels are diminished, but do not completely vanish, as shown in Figure 6.6. The friction utilisation at the low friction side has been reduced while the friction utilization at the high friction side has been slightly increased. As shown by the dashed lines in Figure 6.5, the tracking performance is still good. The lateral offset has been increased by a few millimeters, while the yaw error and the yaw oscillation have been slightly suppressed. The control action of the feedback controller is only slightly changed by the modification of the feedforward controller, as shown by Figure 6.8.

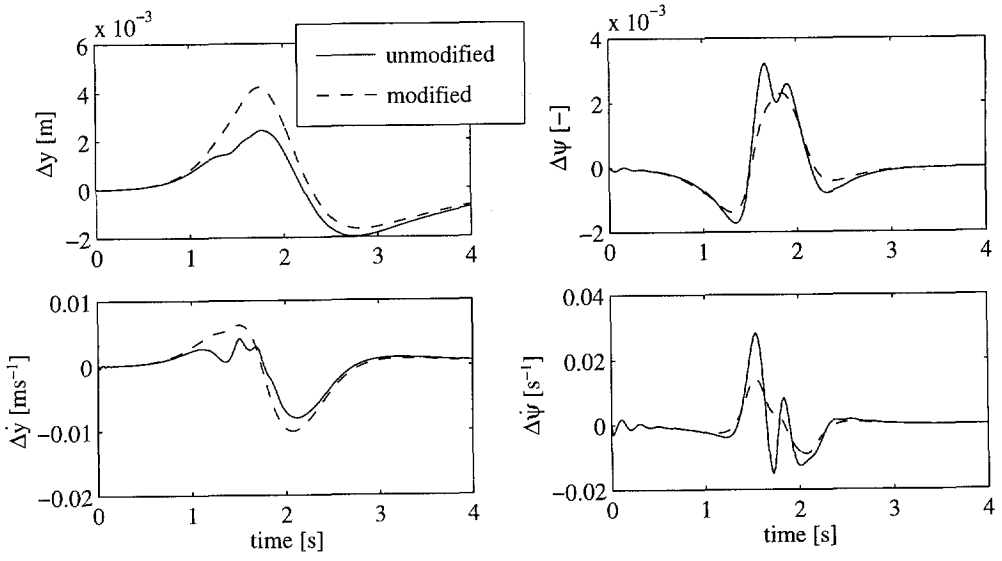

Figure 6.5: *Performance of feedforward+feedback control on nonlinear Simulink model*

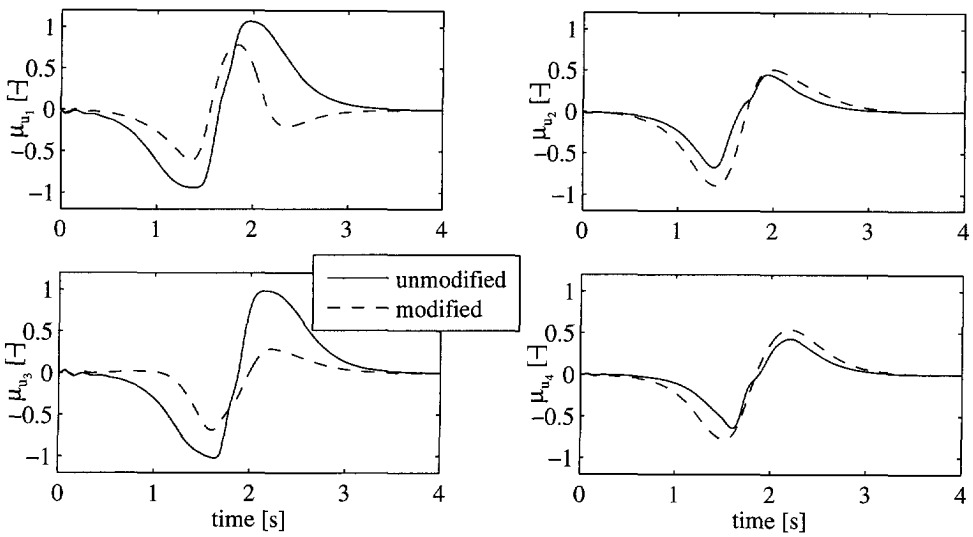

Figure 6.6: *Friction utilization at each wheel with feedforward+feedback control of nonlinear Simulink model*

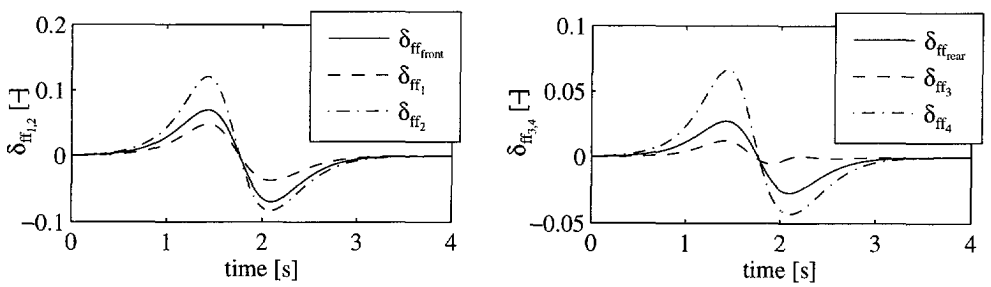

Figure 6.7: *Feedforward control output without and with modification for friction utilization*

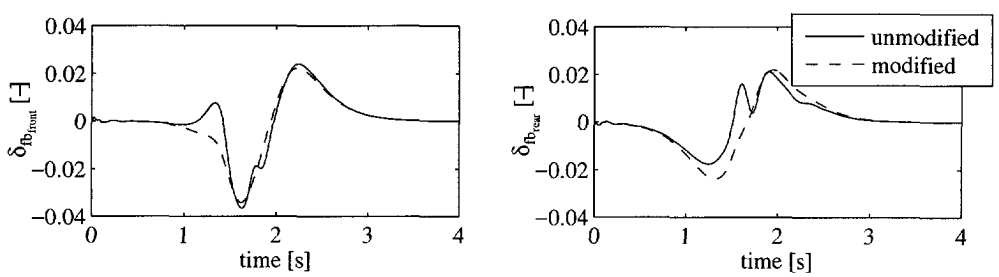

Figure 6.8: *Feedback control output without and with modification of the feedforward control for friction utilization*

6.2.6. Some remarks on the four-wheel steering control design

In this discussion many aspects that are relevant to four-wheel steering control have not been taken into account, including the actuator dynamics. On the other hand, fairly simple enhancements of the control algorithm such as adding preview have not been considered either. Furthermore, in this controller design the friction and side slip angle information has been used only in the feedforward law, while the feedback law remained unchanged. Strictly speaking, if side slip information is fed back into the feedforward controller, it is no longer a feedforward controller. An integrated approach to the design of both feedforward and feedback laws using the frcition and side slip angle information would therefore be preferable. Finally, a more thorough design should involve extensive tests of performance and robustness. This controller design should not therefore be considered as a guideline for four-wheel steering control design, but merely as an indication of potential possibilities.

Since knowledge of the tyre-to-road friction only becomes important at higher levels friction utilisation, it is less important to have good friction estimates at low levels of friction utilisation. However, the estimate should be fast and reliable at higher friction utilisation levels. Since the suggested friction estimator meets these demands, it could be used for this purpose.

6.3. Active Yaw Control

In addition to steering, each wheel may be braked individually to accomplish a desired yaw rate, as has been shown in many publications (e.g. [69]). For this system, the benefits of the integration of a friction estimator in the controller design for active yaw control are essentially the same as for four-wheel steering control.

Active yaw control by applying brake torques to the various wheels is only intended for near critical situations. Therefore, although it is not necessary to have a friction estimate at low friction utilisation, the estimate should be fast and reliable at high friction utilisation. The suggested friction estimator can meet these demands. It should be noted, however, that since braking forces are applied, friction estimators using the control cycle of the anti-lock system may also be used.

6.4. Automated Highway Systems

The congested highway systems in their countries have inspired governments of various industrialised countries to subsidise research in the optimisation of the utilisation of the highways. This research on so-called Automated Highway Systems (AHS) covers various research areas, such as traffic management systems, traveller information systems, advanced vehicle control systems and advanced public transportation systems. A survey of the various research efforts throughout the world has been made in [30].

One of the key issues in this research is minimising the intervehicle spacing at high speed in order to increase the highway capacity. However, high accident rates due such a system would not be acceptable. Since with very short distances between leading and following cars the human driver is not a reliable controller, fast and reliable automated controllers have to be designed. Obviously, the available tyre to road friction is a prominent factor in the determination of the minimum allowable intervehicle spacing at a given speed. For this reason, a lot of attention is being paid to friction estimators.

One of the requirements of such an estimator in this application is that it should provide reliable information, even at very low levels of friction utilization. As shown in this thesis, using the tyre force relationships as a basis for friction estimation does not fulfil this requirement. Therefore, one will have to either resort to the indirect methods (see Chapter 2) such as optical and acoustical methods, or have the road administrator provide the friction information through communication with the vehicles.

6.5. Conclusions of this chapter

This chapter illustrated the possible use of tyre to road friction and side slip angle estimates in the design of vehicle control concepts. As a case study, the design of a simple four-wheel steering controller, provided with friction and side slip angle information, was carried out. Although this relatively simple control design could be improved, it already shows that, for example, a goal such as equalising the friction utilisation at left and right wheels can be accomplished using friction and side slip information. Since these benefits show up primarily at higher friction utilization, the friction estimator discussed in this thesis may well serve to provide this information. The same holds true for active yaw control by applying braking torques to individual wheels.

For automatic distance keeping in Automated Highway Systems however, the desired intervehicle spacing has to be set before a substantial utilisation of the friction potential has been reached. This minimum distance is based on the tyre to road friction coefficient as well as a number of other factors. In that case, friction estimators based on tyre or vehicle behaviour are not suitable for implementation, since they will not provide reliable estimates at low friction utilisation.

These findings again show the need to determine the requirements for the friction estimator prior to the design of such an estimator.

7

Conclusions and Recommendations

7.1. Introduction

This chapter provides the conclusions of this thesis and recommendations for further research. The main conclusions will be stated first, followed by more in-detailed conclusions regarding the different parts of the research. Finally some recommendations will be formulated.

7.2. Main Conclusions

Recalling the main subject of the thesis, 'investigation of the possibility to use the tyre as a sensor for online identification of tyre to road friction characteristics', we may conclude:

1. The tyre can be used as a sensor for online identification of the tyre-to-road friction coefficient, as soon as the generation of tyre forces and torques becomes dependent on the friction coefficient. The limit lies around 30% utilisation of the available friction potential. The tyre forces and torques are generated almost only by adhesion friction if the degree of friction utilisation is below this limit. Above this limit, some sliding occurs in the contact patch and consequently the friction coefficient can be estimated.
2. In addition to the friction coefficient, the side slip angle and the degree of friction utilisation can be estimated. The estimate of the side slip angle becomes more accurate at lower degrees of friction utilisation.
3. Neural Networks have proven to be flexible tools to build the friction estimator
4. The friction estimator under consideraton is primarily suitable for implementation in vehicle control systems that become active when there are intermediate to high degrees of friction utilisation.

7.3. Conclusions with respect to the different parts of the research

7.3.1. Conclusions with respect to the tyre theory

Using the simple brush tyre model, it was shown that the relationship between side force and self aligning torque is dependent on both side slip angle and friction coefficient. This dependency can be used to identify the slip angle and the friction coefficient, provided that the tyre behaviour and the other relevant conditions (vertical wheel load, longitudinal slip and wheel orientation) are known. The possibility to identify slip angle and friction coefficient depends on the degree of slip in the contact area between tyre and road. Three cases with increasing degree of slip can be distinguished:

1. *Complete adhesion* - the side slip angle can be estimated, but the friction coefficient cannot be estimated
2. *Adhesion and sliding* - both the friction coefficient and the side slip angle can be estimated
3. *Complete sliding* - the friction coefficient can be estimated, but the side slip angle cannot be estimated.

The sensitivity analysis of the friction and side slip angle estimate shows that for the friction estimate it is most important to have accurate measurements of the self aligning torque, while for the side slip angle estimate it is primarily the side force that needs to be measured accurately.

Although the results of the simple brush tyre model only have a qualitative meaning, they are supported by the results obtained by using the Delft Tyre Model.

The dynamic behaviour of the tyre has not been considered in this research. It is expected that the transient behaviour of the tyre due to the relaxation length may become important only during fast steering manoeuvres.

7.3.2. Conclusions with respect to the identification methods

The identification was focused on methods to describe the static nonlinear relation between side force and self aligning torque in relation to the friction coefficient and the side slip angle. Two methods have been discussed.

1. *Identification using Lookup Tables* - The infinite number of possible combinations of conditions makes it necessary to transform the forces and torque measurements to equivalent values for a predefined set of nominal conditions. Then, a relatively small table can be used. Although filling the table can be difficult, once the table has been made the table lookup method is very

straightforward. A problem is its sensitivity to minor changes in operating conditions.

2. *Identification using Neural Networks* - Feedforward Neural Networks offer a very flexible solution to the mapping problem. This type of neural networks may be regarded as a generalisation of lookup tables. Using neural networks involves two steps: choosing the network architecture and optimising the network parameters. The first step is usually made on the basis of experience and rules of thumb, but choosing the network architecture may also be regarded as an optimisation problem that can be solved by using Genetic Algorithms. However, the latter option is extremely computationally expensive. For the second step, the training of the network, many standard algorithms are available. Feedforward neural networks are quite robust towards disturbances.

Because of their good results and flexibility, neural networks were selected for this research.

7.3.3. Conclusions with respect to the application

Experiments with the tyre test trailer have shown the validity of the friction estimation method. As we would expect, based on the knowledge of the tyre models, the accuracy of the friction estimate increases with increasing friction utilisation, while the accuracy of the side slip angle estimate increases with decreasing friction utilisation.

Implementation of the estimation method into a standard vehicle required the development of a measurement system to determine the required tyre forces and self aligning moment, as well as the wheel orientation relative to the vehicle body and the road surface. In addition to some standard equipment, the king pin was gauged to serve as a force sensor. By using the measurements and a neural network, it was possible to make an adequate description of the strongly nonlinear behaviour of the vehicle suspension. Consequently, the friction coefficient and the side slip angle could also be estimated using these measurements. This has been shown both by computer simulations, using a 17 degrees of freedom nonlinear multi-body full-vehicle model, and by using the instrumented vehicle.

The friction and side slip angle estimator are expected to be robust to changes in vehicle properties such as mass and inertia, as well as to side wind disturbances and road banking and grading. However, the estimator is expected to be sensitive to varying tyre inflation pressure, tyre temperature and wear.

7.3.4. Conclusions with respect to the integration of friction estimates into advanced vehicle control systems

Advanced vehicle control systems can benefit from friction and side slip angle information. A simple example using a four-wheel steering controller illustrated the benefit that such systems may have of using the friction and side slip angle information.

Since the friction estimator proposed in this research only generates reliable estimates at medium and high levels of friction utilisation, the estimator is especially suited for control systems that are activated in those situations. However, the method is not suited for automatic distance keeping , since this control system requires friction estimates also at low levels of friction utilisation.

7.4. Recommendations

A number of problems regarding the estimation of friction and side slip using the proposed method require further attention:

1. *Definition of demands on the friction and side slip estimator* - At present, rather rough friction estimates are being used in advanced vehicle control systems. With the availability of more advanced friction and side slip estimators, it may be worthwhile to investigate to what extent better friction and side slip angle estimates can further improve the vehicle control behaviour, such that the demands that have to be put on a friction estimator can be specified.
2. *Filtering of the friction estimate* - By using more advanced filtering techniques it may be feasible to extract a smoother friction estimate from the available measured signals and neural networks than currently has been achieved.
3. *Self adapting estimator* - It would be advantageous to develop a self adapting algorithm for the estimator that relatively slowly adapts to varying working conditions, such as tyre wear and varying tyre inflation pressure and changing of tyres. Neural networks may be suitable to develop such an algorithm.
4. *More robust and cheaper instrumentation* - Although the location of the king pin is very convenient to measure the tyre generated forces, the gauged king pin proved to be quite fragile. With further integration of the sensors in the wheel suspension, bearing in mind that forces and torques need to be measured while designing the wheel suspension, it may become feasible to develop more robust sensors. The load cell in the steering link and the steering wheel sensor used in this research may be replaced by information from the power steering system.
5. *More variation in operating conditions* - Owing to the limited availability of suitable test tracks to test the estimator with the test car, the estimator was only tested on two different road surfaces, namely a low friction ABS test track and a high friction concrete road track. The dimensions of the test track also dictated the achievable vehicle speed. It is to be expected that the vehicle speed

will be an important factor that can be easily accounted for, while the vehicle speed is easily measurable. Moreover, tests on other surfaces such as packed snow would contribute to the overall estimation properties. Furthermore, it is recommended that tests to determine the sensitivity of the estimator to variations in tyre inflation pressure, temperature and wear should be carried out.

6. *Research on tyre behaviour related to variations in temperature* - The tyre temperature depends on a number of factors, for example the ambient temperature, the rolling resistance of the tyre, the heat transfer to the road surface or a lubricant (e.g. a wet road) and the surrounding air, and the amount of heat produced by the frictional forces in the contact area. The temperature certainly affects the tyre behaviour, however it is not yet clear to what degree. So far, it has been difficult to measure the tyre temperature in a standard vehicle. However, with the availability of cheaper infrared sensors, the tyre temperature may prove to be a viable parameter for the tyre to road friction estimation.

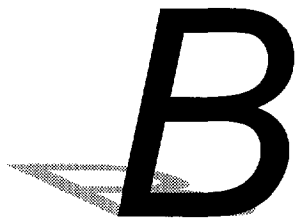

Bibliography

[1] Alleyne A., **A Comparison of Alternative Obstacle Avoidance Strategies for Vehicle Control**, Vehicle System Dynamics, Vol. 27, pp. 371-392, 1997

[2] Bachmann T., Ernesti S., Breuer B., **Influences on and Detection of Tyre/Road-Friction**, Proceedings of the XXVth FISITA Congress, Beijing, 1994

[3] Bachmann T. and Breuer B., **Reibwertforschung an der Schnittstelle Reifen/Fahrbahn**, Proceedings of Darmstadter Reifenkolloquium, ed. Breuer B., VDI Forschritt-Berichte Reihe 12 Nr. 285, 1996

[4] Bakker E., Nyborg L., Pacejka H.B., **Tyre Modelling for the Use of Vehicle Dynamics Studies**, SAE-paper 870421, 1987

[5] Bakker E., Pacejka H.B., Lidner L., **A New Tire Model with an Application in Vehicle Dynamics**, SAE-paper 890087, 1989

[6] Bayle P., Forissier J.F., Lafon S., **A new tyre model for vehicle dynamics simulations**, Automotive Technology International '93, pp. 193-198

[7] BioComp Systems Inc., **Neuro Genetic Optimizer**, BioComp Systems Inc., Redmond, WA, U.S.A, 1997

[8] Bishop C.M., **Neural Networks for Pattern Recognition**, Oxford University Press, 1995

[9] Davis L., **Handbook of Genetic Algorithms**. Van Nostrand Reinhold, New York, U.S.A., 1991

[10] Demuth H. and Beal M., **Neural Network Toolbox User's Guide**. The Mathworks, Inc., U.S.A., 1994

[11] Dieckmann Th., **Assessment of road grip by way of measured wheel variables**, Proceedings of the XXIVth FISITA Congress, London, 1992

[12] Dieckmann Th., **Der Reifenschlupf als Indikator für das Kraftschlußpotential**, IKH Universität Hannover, Dissertation, 1992

[13] Dixon J.C., **Tyres, Suspension and Handling**, Cambridge University Press, 1991

[14] Doebelin E.O., **Measurement Systems, Application and Design**, 3rd edition, McGraw-Hill Mechanical Engineering Series, 1986

[15] Eichhorn U., Seibert W., **System for parameter-measurement and - evaluation on the process of tyre/road-friction**, 3rd PROMETHEUS Workshop, Torino, 1990

[16] Eichhorn U., Roth J., **Prediction and monitoring of tyre/road friction**, Proceedings of the XXIVth FISITA Congress, London, 1992

[17] Eichhorn U., **Reibwert zwischen Reifen und Fahrbahn - Einflußgrößen und Erkennung**, VDI Berichte Nr. 222, 1994

[18] Fonda A.G., **Tyre Tests and Interpretation of Experimental Data**, Research in Automobile Stability and Control and in Tyre Performance, Cornell Aeronautical Laboratory, Inc. of Cornell University, 1956

[19] Frank P.M., **Introduction to system sensitivity theory**, Academic Press, Inc., New York, 1978

[20] Fujioka T. and Goda K., **Discrete Brush Tire Model for Calculating Tire Forces**, in proceedings of 14th IAVSD Symposium held in Ann Arbor, Michigan USA, 1995, Vehicle System Dynamics Supplement 25, pp. 200-216, 1996

[21] Gillespie Th.D., **Fundamentals of Vehicle Dynamics**, SAE Warrendale, PA, USA, 1992

[22] Görich H.J., **Basic System for Friction Detection and Monitoring**, Prometheus Report 1991

[23] Görich H.J., Jacobi S., Reuter U., **Ermittlung des aktuellen Kraftschlußpotentials eines Pkws im Fahrbetrieb**, VDI Berichte Nr. 1088, 1993

[24] Goldberg D.E., **Genetic Algorithms in Search, Optimization, and Machine Learning**, Addison-Wesley Publishing Company, Inc., 1989

[25] Gustafsson F., **Slip-based tire-road friction estimation**, Automatica, Vol. 33, No.6, pp. 1087-1099, 1997

[26] Haeg S. R., **Steer Dynamics in Road Simulation**, SAE-paper no. 970381, 1997

[27] Haykin S., **Neural Networks, A Comprehensive Foundation**, MacMillan College Publishing Company, Inc., ISBN 0-02-352761-7, 1994

[28] Higuchi A., **Transient Response of Tyres at Large Wheel Slip and Camber**, Disseration, Delft University of Technology, 1997 (expected)

[29] Holzwarth F., **A prototype of a measuring water sensor**, 3rd PROMETHEUS Workshop, Torino, 1990

[30] Ioannou P.A., **Automated Highway Systems**, Center of Advanced Transportation Technologies, Univ. of Southern California, Los Angeles, U.S.A., 1997

[31] Ito M., Yoshioka K., Saji T., **Estimation of Road Surface Conditions Using Wheel Speed Behavior**, Proceedings of AVEC'94 Conference, Tsukuba City, Japan, 1994

[32] Kiencke U., Daiß A., **Estimation of Tyre Friction for enhanced ABS Systems**, Proceedings of AVEC'94 Conference, Tsukuba City, Japan, 1994

[33] Klaarenbeek F.W.G., **Lateral Friction Estimation Based on Model Reference**, Master Thesis, Report No. 96.3.VT.4806, Delft University of Technology, 1996

[34] Lee A.Y., **A Preview Steering Autopilot Control Algorithm for Four-Wheel-Steering Passenger Vehicles**, ASME Journal of Dynamic Systems, Measurement and Control, Vol. 114 pp. 401-408, 1992

[35] Liu C.-S., Peng H., **Road Friction Coefficient Estimation For Vehicle Path Prediction**, Proceedings of IAVSD'95 Conference, Ann Arbor, USA, 1995

[36] Ljung L.J., **System Identification: Theory for the User**, Prentice Hall, 1987

[37] Moran A., **Identification and Control of Nonlinear Vehicle Dynamics Using Neural Networks**, Tokyo University of Agriculture and Technology, Doctoral Thesis, 1994

[38] Naab K., Hoppstock R., **Sensor Systems And Signal Processing For Advanced Driver Assistance**, Smart Vehicles, Pauwelussen J.P. and Pacejka H.B. (eds.), pp. 69-97, Swets & Zeitlinger, 1995

[39] Orr M.J.L., **Introduction to Radial Basis Function Networks**, University of Edinburgh, Centre of Cognitive Science, http://www.cns.ed.ac.uk/people/mark/intro/intro.html, 1996

[40] Pacejka H.B., **The Tire as a Vehicle Component**, Chapter 9 of Mechanics of Pneumatic Tires, ed. S.K. Clark, N.B.S. Monograph 122, Washington D.C. 1971

[41] Pacejka H.B., **The Tire as a Vehicle Component**, Chapter 9 of Mechanics of Pneumatic Tires, ed. S.K. Clark, N.B.S. Monograph 122, Washington D.C. 1971

[42] Pacejka H.B., **Modelling of the pneumatic tyre and its impact on vehicle dynamic behaviour**, Vehicle Research Laboratory, Delft University of Technology, The Netherlands, 1988

[43] Pacejka H.B., Sharp R.S., **Shear force development by pneumatic tyres in steady state conditions: A review of modelling aspects.** Vehicle System Dynamics Vol. 20, pp. 121-176, 1991

[44] Pacejka H.B., **The Tyre as a Vehicle Component,** Proceedings of XXVI FISITA Congress, Prague, 1996

[45] Pal C., Hagiwara I., Morishita S., Inoue H., **Application of Neural Networks in Real Time Identification of Dynamic Structural Response and Prediction of Road-Friction Coefficient μ from Steady State**

Automobile Response , Proceedings of AVEC'94 Conference, Tsukuba City, Japan, 1994

[46] Palkovics L., El-Gindy M., Pacejka H.B., **Modelling of the cornering characteristics of tyres on an uneven road surface: a dynamic version of the 'Neuro-Tyre'**, Int. J. of Vehicle Design, Vol. 15, Nos. 1/2, pp. 189-215

[47] Pasterkamp W.R., Pacejka H.B., **On Line Estimation of Tyre Characteristics For Vehicle Control**, Proceedings of AVEC'94 Conference, Tsukuba City, Japan, 1994

[48] Pasterkamp W.R., Pacejka H.B., **Friction Recognition Using The Tyre As Sensor**, Proceedings of IFAC'96 World Congress, San Francisco, 1996

[49] Pasterkamp W.R., Pacejka H.B., **The Tyre As A Sensor To Estimate Friction**, Vehicle System Dynamics, Vol. 27, pp. 409-422, 1997

[50] Peng H., Tomizuka M., **Preview Control for Vehicle Lateral Guidance in Highway Automation**, ASME Journal of Dynamic Systems, Measurement, and Control, Vol. 115 pp. 679-686, 1993

[51] Pham D.T., Xing L., **Neural networks for identification, prediction and control**, Springer-Verlag, London, 1995

[52] Ray L.R., **Nonlinear State and Tire Force Estimation for Advanced Vehicle Control**, IEEE Transactions on Control Systems Technology, Vol. 3, No. 1, pp. 117-124, March 1995

[53] Ray L.R., **Real-Time Identification of Road Coefficient of Friction for IVHS and Advanced Vehicle Control**, Proceedings of 1995 American Control Conference, Seattle WA, Vol. 3, June 1195, pp. 2133-2137

[54] Ray L.R., **Nonlinear Tire Force Estimation and Road Friction Identification: Field Test Results**, SAE paper no. 960181, 1996

[55] Reimpel J., **Fahrwerktechnik: Lenkung**, Vogel-Buchverlag, Würzburg, Germany, 1984 (in german)

[56] Ripley B.D., **Pattern Recognition and Neural Networks**, Cambridge University Press, 1996

[57] Roth J., **Untersuchungen zur Kraftübertragung zwischen Pkw-reifen und Fahrbahn unter besonderer Berücksichtigung der Kraftschlußerkennung im rotierenden Rad**, VDI Berichte Nr. 195, 1993

[58] Sarle W.S., **Neural Networks and Statistical Models**, Proceedings of the Nineteenth Annual SAS Users Group International Conference, 1994

[59] Sjöberg J., **Non-Linear System Identification with Neural Networks**, Linköping University, Sweden, doctoral thesis, 1995

[60] Stamm K., **Description, Identification and Compensation of Nonlinearities by Means of Look-Up-Tables**, Proceedings of the 1996 IEEE Int. Symposium on Computer-Aided Control System Design, Dearborn, MI, 1996

[61] Takahashi T., Pacejka, H.B., **Cornering on Uneven Roads**, Proceedings of the 10th IAVSD Symposium, 1988

[62] Turco P., Borodani P., Klaarenbeek F.W.G., **Algorithms for a Vehicle Dynamics Monitoring System, Based on Model Reference Structure**, Proceedings of the 1st International Conference on Control and Diagnostics in Automotive Applications, Genova, Italy, 1996

[63] Verheul, C.H., **Bond Graph Based Modelling using Macros, an Introduction to the Program BAMMS**, Application of Multibody Computer Codes to Vehicle System Dynamics, Progress Report to the 12th IAVSD Symposium on a Workshop and Resulting Activities, 1991

[64] Venhovens, P.J.Th., **Optimal Control Of Vehicle Suspensions**, Delft University of Technology, doctoral thesis, 1993

[65] Witte, B. and Zuurbier, J., **Detection of Friction Coefficient in a running Vehicle and Measurement of Tire Parameters on different Road Surfaces**, VDI Berichte Nr. 1224 (in german)

[66] Würtenberger M. and Isermann R., **Model based supervision of lateral vehicle dynamics**, proceedings of the American Control Conference, Vol. 1, pp. 408-412, 1994

[67] Yamazaki, S., Furukawa, O. and Suzuki, T., **Study on Real Time Estimation of Tire to Road Friction**, proceedings 15th IAVSD Symposium held in Berlin, Germany, Vehicle System Dynamics Supplement 27, pp. 225-233, 1997

[68] Zadeh A.G., Fahim A. and El-Gindy M., **Neural network and fuzzy logic applications to vehicle systems: literature survey**, Int. Journal of Vehicle Design, Vol. 18, No.2, pp. 132-193, 1997

[69] Zanten, A. Van, Erhardt R., Pfaff, G., **VDC, The Vehicle Dynamics Control System of BOSCH**, SAE 950759, 1995

Summary

The Tyre As Sensor To Estimate Friction

Wim R. Pasterkamp

The demand for enhancement of the safety and the performance of automobiles has led to the implementation of modern vehicle control systems, such as anti-lock brake systems (ABS), active yaw control systems (AYC) and vehicle dynamics control systems (VDC), into the vehicle. These control systems can only perform to their full potential if they have access to accurate information about the behaviour of the vehicle. In this respect, the tyre-to-road friction is one of the key parameters that need to be determined. This thesis, therefore, focuses on investigation of the possibility to use the tyre as a sensor for online identification of tyre-to-road friction characteristics. In particular, the lateral behaviour of the tyre has been investigated.

A tyre, rolling over the road surface while subjected to a side slip angle and a vertical load, generates a side force and a self aligning torque around its vertical axis if there is friction between the tyre and the road surface. The ratio between the actually generated friction force and the maximum friction force that can be achieved under the given conditions of vertical load and friction coefficient defines the level of friction utilisation.

The tyre behaviour is studied using a simple, steady state brush type tyre model. Assuming a constant vertical load, this results in the following findings for pure side slip. With increasing levels of friction utilisation, the planar tyre forces are transmitted by adhesion friction only, adhesion and sliding friction or sliding friction only. As long as the forces between the tyre and the road are transmitted by

adhesion friction only, the side force and the self aligning torque are linearly dependent on the side slip angle and independent of the friction coefficient between the tyre and the road. As soon as some sliding occurs in addition to the adhesion in the contact patch between the tyre and the road, the side force and the side slip angle become nonlinearly dependent on both the side slip angle and the friction coefficient. If there is complete sliding of the tyre over the road surface, the side force is dependent on the friction coefficient only, while the self aligning torque becomes zero.

By applying the relations between side slip angle and friction coefficient on the one hand and side force and aligning torque on the other hand conversely, it is possible to determine the friction coefficient from the combination of side force and self aligning torque if there is some sliding or complete sliding in the contact area. In addition, it is possible to determine the side slip angle if there is complete or partial adhesion friction between the tyre and the road. This provides a method to estimate the friction coefficient and the side slip angle.

A sensitivity analysis shows that the friction estimate is primarily sensitive to inaccuracies in the determination of the self aligning torque, especially at low levels of friction utilisation. The side slip angle estimate is primarily sensitive to inaccuracies in the determination of the side force, in particular at high levels of friction utilisation. A qualitative analysis shows that the estimates are also sensitive to other common disturbances, such as combined slip, camber and residual forces. However, if these disturbances can be determined, they can be accounted for in the estimation method. The transient behaviour of the tyre may become important during fast steering manoeuvres on undulating road surfaces.

The Delft Tyre Model, which describes the actual tyre behaviour more accurately, shows the same qualitative behaviour with respect to the estimation of the side slip angle and the friction coefficient as the brush type tyre model.

Experiments with the tyre test trailer have shown the validity of the friction estimation method. As expected, based on the knowledge of the tyre models, the accuracy of the friction estimate increases with increasing friction utilisation, while the side slip angle estimate increases with decreasing friction utilisation.

For the actual estimation of the friction coefficient and the side slip angle, neural networks have been employed. Feedforward neural networks provide the necessary nonlinear mapping between measured forces and torques on the one hand, and side slip angle and friction coefficient on the other hand. These findings have been confirmed by simulations and by experiments with the tyre test trailer. While the optimisation of the neural network parameters can be achieved by standard

algorithms such as backpropagation and Levenberg-Marquardt, the choice of the network architecture requires expertise and trial and error. Alternatively, genetic algorithms can be employed to optimise the network architecture, but this approach usually involves extensive computations.

Implementation of the estimation method into a standard vehicle required the development of a measurement system to determine the required tyre forces and self aligning moment, as well as the wheel orientation relative to the vehicle body and the road surface. In addition to some standard equipment, the king pin (lower ball joint) was gauged to serve as a force sensor. A neural network has been trained to describe the strongly nonlinear behaviour of the suspension and to perform the actual estimation of the friction coefficient and the side slip angle from the sensory signals. Experiments with both a simulation model and with the actual vehicle were conducted on various test tracks to demonstrate the desired behaviour of the estimator.

Finally, some examples are presented to illustrate the possible integration of friction and side slip angle estimation into vehicle control systems. A small case study on four wheel steering has been conducted. Because of the nature of the proposed friction estimator, it is primarily suitable for systems that benefit from the friction and side slip angle information at medium to high levels of friction utilisation. This holds true for systems such as four wheel steering and active yaw control, but not, for example, for automatic distance keeping, where the friction estimate has to be made before a substantial friction demand has been made. It is therefore important to determine the demands prior to the design of such an estimator.

Samenvatting

The Tyre As Sensor To Estimate Friction (De band als sensor om wrijving te schatten)

Wim R. Pasterkamp

De vraag naar verbetering van de veiligheid en de prestaties van de automobiel heeft geleid tot implementatie van moderne voertuigregelsystemen in de auto, zoals ABS, AYC en VDC. Alleen wanneer deze regelsystemen kunnen beschikken over nauwkeurige informatie omtrent het voertuiggedrag kunnen ze optimaal presteren. In dit verband is de wrijving tussen band en wegdek een van de belangrijkste parameters die bepaald moeten worden. Daarom behandelt dit proefschrift de mogelijkheid om de band als sensor te gebruiken om de wrijving tussen band en wegdek te kunnen bepalen. Met name het laterale bandgedrag krijgt hierbij de aandacht.

Een band die rolt over het wegdek onder een sliphoek en een vertikale belasting genereert een dwarskracht en een terugstelmoment indien er sprake is van wrijving tussen de band en het wegdek. Het bandgedrag is bestudeerd aan de hand van een eenvoudig, quasi-statisch borstelmodel. Bij een gegeven constante vertikale belasting kan het volgende omtrent het bandgedrag bij pure dwarsslip waargenomen worden:

Bij toenemende mate van wrijvingsbenutting, dat wil zeggen het deel van de potentieel beschikbare wrijvingskracht dat daadwerkelijk aangesproken wordt, worden de wrijvingskrachten tussen de band en het wegdek in het contactvlak allereerst overgedragen door adhesiewrijving, dan door een combinatie van adhesie en glijden en tenslotte alleen door glijden. Zolang de krachten tussen band en

wegdek alleen door adhesie overgedragen worden, zijn de gegenereerde dwarskrachten en terugstelmomenten lineair afhankelijk van de sliphoek. Zodra de grenzen aan de adhesiekrachten bereikt zijn en er sprake is van enige mate van glijden in het contactvlak worden de dwarskracht en het terugstelmoment worden op niet-lineaire wijze afhankelijk van zowel de sliphoek als de wrijvingscoëfficiënt. Bij volledig glijden van de band over het wegdek wordt de dwarskracht onafhankelijk van de sliphoek en alleen afhankelijk van de wrijvingscoëfficiënt, terwijl het terugstelmoment tot nul reduceert.

Door de relaties tussen sliphoek en wrijvingscoëfficiënt enerzijds en dwarskracht en terugstelmoment anderzijds in omgekeerde zin te benutten, kan de wrijvingscoëfficiënt bepaald worden uit de combinatie van dwarskracht en terugstelmoment bij gedeeltelijk of volledig glijden van de band over het wegdek, en kan de sliphoek bepaald worden uit de combinatie van dwarskracht en terugstelmoment bij gedeeltelijke of volledige adhesie tussen band en wegdek in het contactoppervlak. Op deze grond kan een wrijvingsschatter en een sliphoekschatter gecreëerd worden.

Een gevoeligheidsanalyse voor het borstelmodel bij pure dwarsslip toont aan dat de wrijvingsschatting vooral gevoelig is voor meetonnauwkeurigheden en andere verstoringen bij lage niveaus van wrijvingsbenutting. Met name onnauwkeurigheden in de bepaling van het terugstelmoment veroorzaken dan grote afwijkingen in de wrijvingsschatting. De sliphoekschatting daarentegen is vooral gevoelig voor onnauwkeurigheden in de dwarskracht, bij hoge niveaus van wrijvingsbenutting. Kwalitatief is ook aangetoond dat andere veel voorkomende verstoringen zoals het optreden van gecombineerde slip, camber en residuele krachten de schattingen kunnen verstoren. Voor deze verstoringen kan echter gecompenseerd worden indien ze bepaald kunnen worden. Het overgangsverschijnsel dat optreedt bij banden als gevolg van de relaxatielengte kan van belang zijn bij snelle stuurmanoeuvres en bij het rijden over oneffen wegdekken.

Het 'Delft Tyre Model', dat het bandgedrag preciezer beschrijft dan het borstelmodel, vertoont in kwalitatieve zin hetzelfde gedrag als het borstelmodel.

Door middel van experimenten met de bandenmeetwagen is de geldigheid van de wrijvings- en sliphoekschattingsmethode aangetoond. Zoals verwacht op grond van de bandmodellen neemt de nauwkeurigheid van de wrijvingsschatting toe met toenemende mate van wrijvingsbenutting, terwijl de nauwkeurigheid van de sliphoekschatting toeneemt met afnemende wrijvingsbenutting.

Voor de daadwerkelijke schatting van de wrijvingscoëfficiënt en de sliphoek is gebruik gemaakt van neurale netwerken. De zogenaamde 'feedforward' neurale netwerken kunnen het niet lineaire verband tussen de gemeten krachten en koppels enerzijds en de sliphoek en de wrijvingscoëfficiënt beschrijven. Deze bevindingen zijn bevestigd door middel van simulaties en door middel van experimenten met de bandenmeetwagen. Het optimaliseren van de netwerkparameters geschiedt met behulp van standaardalgoritmen zoals de zogenaamde 'backpropagation' en 'Levenberg-Marquardt' algoritmen. De keuze van de netwerkstructuur is echter veelal een zaak van expertise en experimenteren. Er kan ook gebruik gemaakt worden van genetische algoritmen om de optimale netwerkstructuur te bepalen, maar dit gaat in het algemeen gepaard met zeer uitvoerige berekeningen.

Voor de implementatie in een standaard automobiel was de ontwikkeling van een meetsysteem dat in staat is de vereiste bandkrachten en -momenten en de wielstand ten opzichte van het voertuig te bepalen, noodzakelijk. Behalve enige standaardopnemers zijn ook rekstrookjes geplakt op de fuseekogel zodat deze dienst kan doen als krachtsensor. Er zijn neurale netwerken ontworpen en geoptimaliseerd om het gedrag van de ophanging te beschrijven en om de daadwerkelijke wrijvings- en sliphoekschatting uit te voeren aan de hand van de gemeten signalen. Er zijn experimenten uitgevoerd, zowel met een simulatiemodel als met het testvoertuig, om het goed functioneren van de schatter bevestigd te zien.

Tenslotte zijn bij wijze van illustratie van de mogelijke integratie van wrijvings- en sliphoekschatters in voertuigregelsystemen enige voorbeelden gegeven van dergelijke systemen. Een kleine studie naar de integratie van deze schatters in een regelsysteem voor vierwielsturing is uitgevoerd. Door de aard van de voorgestelde wrijvingsschatter is deze met name geschikt voor systemen die de schattingen kunnen benutten bij hogere niveaus van wrijvingsbenutting. Hieronder vallen systemen zoals vierwielsturing en actieve giermomentregelingen, maar niet bijvoorbeeld systemen om automatisch afstand te bewaren tot de voorganger, omdat deze laatsten al een schatting van de wrijvingsconditie nodig hebben voordat substantieel gebruik gemaakt is van het beschikbare wrijvingspotentieel. Het is dan ook belangrijk vooraf te bepalen welke eisen aan een wrijvingsschatter gesteld moeten worden alvorens over te gaan tot het werkelijke ontwerp van zo'n schatter.

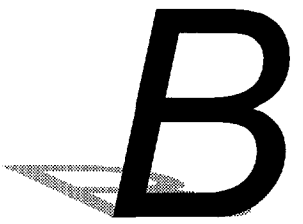

Biography

Wim Pasterkamp was born in Rotterdam, the Netherlands on March 16, 1967. After finishing his pre-university education at the Zandevelt College in 's-Gravenzande in May 1985, he joined the Faculty of Mechanical Engineering at the Delft University of Technology in 1985 and graduated in August 1991. He completed his graduation research at the Measurement and Control Laboratory. The subject of his thesis was the design of a multivariable feedback controller for a hydraulic robot with three coupled rotational degrees of freedom. In November 1991 he became a doctorate student at the Vehicle Research Laboratory, where he has been working on his PhD-thesis and has made contributions to several international conferences and symposia. From October 1997 he has been engaged with the Robert Bosch GmbH in Schwieberdingen, Germany.